

**TEMPORAL AND SPATIAL EVOLUTION OF LASER  
ABLATED CARBON PLASMA IN AMBIENT GAS AND  
MAGNETIC FIELD**

820131

*A Thesis Submitted  
in Partial Fulfilment of the Requirements  
for the Degree of  
DOCTOR OF PHILOSOPHY*

*by*  
**AMIT NEOGI**



to the

**DEPARTMENT OF PHYSICS  
INDIAN INSTITUTE OF TECHNOLOGY**

14 JUN 2000 / PHY  
CENTRAL LIBRARY  
I. I. T., KANPUR  
**A 131098**

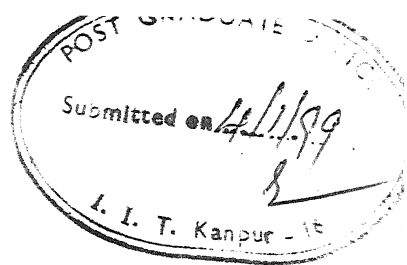
TH  
PHY/1999/P  
NB55



A131098



# CERTIFICATE



It is certified that the work contained in this thesis entitled "*Temporal and Spatial Evolution of Laser Ablated Carbon Plasma in Ambient Gas and Magnetic Field*", by Amit Neogi, has been carried out under my supervision and that this work has not been submitted elsewhere for any degree.

RK Thareja  
Dr. R. K. Thareja 04/01/99  
Professor  
Department of Physics  
Indian Institute of Technology  
Kanpur

January, 1999

---

*It is essential that a student acquire an understanding of and a lively feeling for values. He must acquire a vivid sense of beautiful and of morally good.*

*Otherwise he, with his specialised knowledge more closely resembles a well trained dog than a harmoniously developed person.*

**Albert Einstein**



# Synopsis

---

<i>Name of the student</i>	: Amit Neogi
<i>Roll no</i>	: 9110962
<i>Department</i>	: Physics
<i>Degree for which submitted</i>	: Ph.D
<i>Thesis title</i>	: Temporal and Spatial Evolution of Laser Ablated Carbon Plasma in Ambient Gas and Magnetic Field
<i>Name of the thesis supervisor</i>	: Professor R. K. Thareja

---

The thesis deals with the study of laser ablated carbon plasma expanding in an ambient gas and nonuniform magnetic field using emission spectroscopy, fast photography and Langmuir probe. The nonuniform magnetic field and ambient gas control the plasma behavior in very many ways which may be important for numerous technological applications and studying astrophysical processes.

The carbon plasma was produced by focussing an Nd:YAG laser (DCR-4G, Laser Spectra) pulse ( $E = 800 \text{ mJ/pulse}$ ,  $\lambda = 1.06 \mu\text{m}$ , pulse width = 8 ns) by a spherical lens on to the surface of a rotating graphite target kept inside the vacuum chamber. The chamber can be evacuated to a pressure better than  $10^{-4}$  Torr. It has a provision for introducing gas into it in a controlled manner. The plasma formed was imaged on to the slit of a monochromator (HRS-2, Jobin Yvon) which can be tuned by a microprocessor scanning system. The output from the monochromator was detected by a photo multiplier tube (PMT)(IP28, Hamamatsu). PMT signal was recorded on the chart recorder and oscilloscope (TS-8123, Iwatsu) and finally stored in the personal computer. The two dimensional

image of the plasma plume were recorded using intensified charged coupled device (ICCD-576G/2, Princeton Instrument). The delay of the opening of the camera shutter with respect to ablating pulse can be varied in steps of 5 nsec. The detector consists of microchannel plate (MCP) with a spectral response in the region 200-820 nm and  $384 \times 576$  CCD array. The microchannel plate along with the CCD makes ICCD a highly sensitive device. The system essentially is an opto-electronic device where the images are stored electronically and analysed by the image processing software. A langmuir probe kept at a distance of 4 mm from the target surface at an angle of  $45^\circ$  monitored the evolution of the plasma.

A one dimensional Lagrangian Code MEDUSA which simulates the temporal and spatial evolution of laser ablated plasma in vacuum is modified for the plasma expansion in high pressure ambient atmosphere. Plasma expanding in high pressure ambient gas gives rise to shock wave in the ambient gas. Rankine-Hugoniot relations for the shock wave are used to calculate the boundary conditions of the plasma front. The plasma expanding with a high velocity  $\sim 10^6$  cm/sec acts like a hot jet streaming into an ambient atmosphere. The plasma boundary undergoes boundary layer mixing with ambient gas and gives rise to shear stress at the boundary. Due to the shear stress the plasma plume experiences viscous drag which decelerates the flow. Prandtl's mixing length theory is used to calculate the total shear stress or the viscous drag experienced by the plasma plume. The external gas diffuses into the plasma plume when the pressure outside the plasma front is almost equal to the pressure inside the plume which gives rise to a diffusive force opposing the motion of the plasma. This diffusive force is proportional to the ratio of internal to external pressure and density of the gas. Finally, the Navier-Stokes equation is modified by incorporating the viscous drag term and diffusive force term. The modified MEDUSA (with the changed boundary conditions and modified Navier-Stokes equation) was used to simulate the carbon plasma expanding in high pressure (300 Torr) ambient gas (He, Ar, Ne and Xe). The simulated temporal variation of the plasma front for all the four gases matches well with the experimental observations. The simulated velocity

and shock wave intensity of the plasma front also match well with the experimental values. The plasma parameters like temperature, pressure and electron density of the plasma front can be simulated for any gas at any higher pressure with the help of modified code.

The temporal profiles of CI transition  $2p^3\ ^3D^0 - 8f\ F(5/2)$  at 399.7 nm, CII transition  $3d\ ^2D - 4f\ ^2F^0$  at 426.7 nm, CIII transition  $3s\ ^3S - 3p\ ^3P^0$  at 465.0 nm and CIV transition at  $3s\ ^2S - 3p\ ^2P^0$  at 580.1 nm were recorded at different distances from the target surface at various pressures of air (0.1 mTorr, 5 mTorr and 100 mTorr). The intensity and nature of the temporal profile is studied for different species and for different pressure. The velocity of all these species was estimated from the delay of the peak of the signal with respect to the ablating pulse. In vacuum, it is observed that the species with higher charge have higher velocities (CII  $\sim 1.24 \times 10^6$  cm/sec, CIII  $\sim 1.76 \times 10^6$  cm/sec, CIV  $\sim 1.90 \times 10^6$  cm/sec at a distance of 4 mm from the target). This is because as the plasma propagates the electrons overtake the ions giving rise to electric field which pulls the ions resulting in higher velocity for higher charge. In 5 mTorr air, the velocity of CIII and CIV species decreases compared to that of vacuum (0.1 mTorr) value but the velocity of CI and CII species increases. In 100 mTorr the velocity of CIII, CIV and CI species decreases compared to that of 5 mTorr but the velocity of CII species increases. The intensity of the species is observed to increase in presence of ambient gas. The ICCD photographs at 5 mTorr at various delay times show stratification of plasma plume into two components, fast and slow at 600 ns. The velocity of the two components is estimated to be  $1.0 \times 10^6$  cm/sec and  $7.5 \times 10^5$  cm/sec and hence termed as fast and slow components respectively. The ICCD images show that the fast component is bulky at earlier time ( $\sim 800$  ns) whereas slow component becomes bulky at later time ( $\sim 1500$  ns). In vacuum the temporal profiles show a single peak structure for all the species. In 5 mTorr and 100 mTorr, double peak structure is observed for CI, CII and CIII transitions whereas no double peak is observed for CIV transition. The appearance of double peak in the temporal profiles is attributed to the stratification of the plasma into slow and fast components as observed in ICCD photographs. The velocity of fast peak increases with the increase of pressure whereas that of the slow peak decreases

with pressure. At 100 mTorr, the fast peak in case of CI and CII is stronger than that of the slow peak whereas in case of CIII the slow peak is stronger. At 5 mTorr, the fast peak is stronger than the slow peak for CI. CII and CIII transitions at distances close to the target ( $\sim 8$  mm) whereas at later distance ( $\sim 14$  mm) it is the slow peak which is dominant in accordance with the results of ICCD photography. The stratification of the plasma plume is attributed to the diffusion of ionized air particles into the plasma plume and collisions with the different charged species of the plasma plume. The collided species give rise to slow component where as uncollided species give rise to fast component resulting in stratification.

The ICCD photographs of the plasma expanding in a nonuniform magnetic field show oscillatory behavior of the plasma front at various delay times. The first contraction of the plasma front is seen at 150 ns and second contraction is observed at 500 ns with respect to the ablating pulse. The solution of energy, momentum and Ohm's law equations of the plasma plume expanding in magnetic field predicts periodic bouncing of the radius of the plasma plume. The experimental observations are in accordance with the theoretical predictions though the radius of the first bounce observed experimentally (0.43 cm) is less than that predicted theoretically (1.64 cm). At a later time ( $\sim 1000$  ns) the plume is observed to break into two lobes which move toward the poles of the magnet. The ICCD images were also used to estimate the plasma parameters. The electron density in presence of magnetic field is found to be higher than that of vacuum case and shows oscillations because of alternate contraction and expansion of the plasmoid at 150 and 500 ns. The typical values of electron density at 150 ns in magnetic field, 100 mTorr air and vacuum are  $1.0 \times 10^{17}/\text{cm}^3$ ,  $5.7 \times 10^{16}/\text{cm}^3$  and  $2.7 \times 10^{16}/\text{cm}^3$  respectively. The temperature of the plasma plume is estimated assuming the plasma plume to behave as an ensemble of black body radiators. The typical values of temperature at 150 ns in magnetic field, 100 mTorr air and vacuum are 3.19 eV, 3.94 eV and 2.42 eV respectively. The temperature in case of magnetic field increases due to Ohmic heating caused by the surface current. In presence of ambient gas the temperature rises due to enhanced interparticle collisions with the gas

particles. The calculated density and temperature of the plasma plume in case of vacuum are fitted with the equation of the form  $y = a t^n$ . The experimental observations give value of  $n = -2.85, -2.73$  compared to theoretical value of  $n = -3, -2$  for density and temperature respectively.

The time integrated spectra of the plasma plume propagating in magnetic field is recorded at a distance of 6 mm from the target surface keeping the target at three different positions in magnetic field (say P, Q, R). The magnetic field strength at position P, Q, and R is 1.0, 3.0 and 2.7 kG respectively. When target is kept at position P, the plasma expands in convex magnetic field with positive field gradient, the position Q is similar to P but gradient is less than that in P whereas in position R the field is concave with negative field gradient. It is found that it is not the magnetic field strength but the curvature and the gradient of the magnetic field which controls the plasma behavior. The plasma expanding in convex magnetic field with positive field gradient (position P) shows a maximum rise in ionic line intensity compared to other positions though the magnetic field is lower. Furthermore,  $C_2$  molecular Swan band emission,  $d^3\pi_g - a^3\pi_u$ , with  $\Delta v = -1, 0, 1$  is observed to dominate at this position. The intensity of  $C_2$  Swan band is very weak at other positions of the target. At position R where magnetic field is concave and gradient is negative, the intensity is less than that of no magnetic field case. Assuming local thermodynamic equilibrium (LTE), the temperature calculated from the ratio of line intensity of two lines of same ionization state at a distance of 6 mm from the target is highest in position P of the target (11.4 eV) and lowest in position R (4.34 eV). The increase in line intensity is attributed to compression of magnetic field lines (magnetic Reynold's number  $\sim 5$ ).  $C_2$  emission in position P of the target is attributed to the movement of electrons due to electromagnetic interaction and that of the ions due to curvature gradient drift which are in the same direction favoring recombination whereas they are in opposite direction in position R of the target.

The time resolved spectra of carbon plasma are recorded for all the species CI, CII, CIII and CIV. As the plasma expands in magnetic field, the field gradient develops at the

plume boundary which gives rise to surface current  $J$ . The current  $J$  inside the plume is in a direction opposite to that at the front. The current  $J$  interacts with the magnetic field and gives rise to  $J \times B$  force which decelerates the bulk of the plasma. But  $-J \times B$  accelerates the boundary. Consequently, we observed three components of the plume viz; fast, intermediate and slow. The ICCD images show that the plasma expanding in nonuniform magnetic field gives rise to two lobes, each of which has three components. The target is kept nearer to one pole such that two asymmetric lobes are formed and the three components from each lobe can be distinguished. However, for a symmetrically placed target between the poles it is difficult to distinguish various components. The observed temporal profile of the species are fitted with Gaussian functions for further investigations. It is found that the species at the outermost boundary, CII and CIV, show a single peak structure at 4 mm from the target surface whereas with increasing distance ( $\sim 10$  mm) multiple peaks (six peaks) are observed. They are because of two fast, two intermediate and two slow components arising from two asymmetric lobes. Multiple peaks and oscillations are observed in the temporal profile of CIII and CI when they are at the outermost boundary (14 mm from the target) where CII and CIV disappear. The multiple peaks and oscillations are attributed due to edge oscillations in magnetic field.

The temporal profiles of the species show interesting features when the plasma expands in combined environment of ambient gas and magnetic field. The multiple peaks vanish and only the double peak structure is observed, similar to the one observed when plasma expands in only gas. Another interesting feature observed is a sudden delay in the second peak for CIII and CII species but not for CI. This delay is not observed when the plasma expands in either only gas or only magnetic field. In order to investigate the delay the target is kept at six different positions in magnetic field and it is observed that delay occurs only when the plasma expands in concave magnetic field. As the target is moved further into the magnetic field a distinct triple peak structure is observed just before the onset distance of sudden delay in second peak. This behavior may be due to Rayleigh-Taylor instability which occurs when a plasma expands in concave magnetic field lines. The plasma (heavy

fluid) expanding against magnetic field (light fluid) undergoes Rayleigh-Taylor instability when the plasma particles move along the concave magnetic field and the centrifugal force drives this instability. The Rayleigh-Taylor instability along with the diffusion of air may be responsible for the sudden delay in second peak. The growth time of the instability is estimated to be 1000 ns. The effective deceleration and density gradient scale length of the plasma was estimated from the ICCD photographs. Since the delay is not observed for neutral species the possibility of recombination or charge exchange is significantly low.

The fast ablated plasma flow into a stationary ambient medium in presence of static magnetic field as discussed earlier can be used to study many magnetospheric and astrophysical processes. At low background gas pressure ( $P < 1\text{ Torr}$ ) collisionless phenomena such as those occurring when solar wind impinges on magnetospheric and ionospheric plasmas and with obstacles such as comet, moons, and planets dominate. At high pressure ( $> 1\text{ Torr}$ ) collisional interstreaming plasma effects such as blast wave formation are generated which behave like supernova shocks. Plasma expanding in magnetic field undergo R-T instability. An analogous instability was observed in March 1985 AMPTE barium cloud experiment in the tail of magnetosphere. The plasma behavior in the curved magnetic field can be used to study the motion of the plasma in curved magnetic field of the earth like generation of ring current in the equatorial plane. Because of cosmic abundance of carbon in the interstellar space, spectroscopic study of carbon species is of great significance. The knowledge of plasma behavior in different ambient conditions elucidates our understanding regarding thin film deposition, surgery and many technological applications.

---

*Dedicated To  
My Spiritual Guru  
Revered Mokshaprana Mataji  
&  
My Dear Parents*



# Acknowledgments

---

I have great pleasure to express my deep sense of gratitude to my thesis supervisor Prof. R. K. Thareja for introducing me to the field of laser plasma interaction. His constant guidance, deep involvement and intuitive insight have greatly enlightened me in the field of research. The good scoldings which were showered on me from time to time have surely contributed to my inner growth and unfoldment and have helped me to finish my work in time. Needless to say, words are inadequate to quantify the qualities of a teacher. I also thank Dr. (Ms) Sukarma Thareja for her care and encouragement during my stay at I.I.T. Kanpur.

I am indebted to Dr. Asima Pradhan and Dr. Mahendra Verma for serving on my peer group and giving me suggestions from time to time. I am also thankful to Dr. Gautam Biswas of Mech. Engg. Dept. for having fruitful discussion on fluid mechanics.

I acknowledge my thanks to Dr. N. C. Gupta of BARC who assisted me to run MEDUSA Code. I am thankful to Dr. H. C. Pant, Dr. Bimla Bhuti, Dr. Lawande, Dr. P. K. Kaw, Dr. Hari Ramachandan, Dr. Sanecha, Dr. K. P. J. Reddy and Dr. Rose (RAL) for having fruitful discussions on my research work. I am very much thankful to Dr. Alikha Khare for giving many valuable suggestions in my experiments.

I acknowledge immense help and cooperation from all my labmates. I thank my seniors Dr. A. Sirkar and Dr. R. K. Dwivedi for their help. I would like to thank Ashutosh, Anirban, S. P. Singh, Narayanan, Ashwini, Sushmita, Shiv Govind and Tripti for their full cooperation and support. I especially thank Ashutosh and Narayanan for helping me during my experiment burning midnight oil. I thank Ashwini, Sushmita and Ashutosh for proof reading my thesis. I wish them all a successful research carrier.

I would like to thank my friends Rajan, Sandeep, Alok Saran, Gautam, Tapan, Dobal, Urvijadi, Mayaji, David, Ramesh, Kanwaljit, Navati and Nirmalya for their help and

cooperation from time to time.

I would like to thank all the staff members of CELT and Physics office and workshop for their cooperation. I would especially like to thank Maharaj Singh for his amicable behavior, cooperation and help. I thank G. S. Thapa for tracing my figures very efficiently.

I thank all the members of Vivekananda Samiti for making my stay at IIT Kanpur very memorable. I thank Shreesh, Anirban, Samudra, Sujit, Amit, Vijaya didi, Pranab, Prabal, Sudipto, Patnaik, Malabika, Chelapati, Kumar Sambhav, Alok, Shanthikaran, Shiva, S. V. Rao, Sushovan, Biswajit, Parasar, Mathew and others. I really enjoyed teaching and interacting with children of Samiti school. I would like to thank especially Pranab and Prabal for their help in computer programing. Vivekananda Samiti has contributed a lot in my inner growth and harmony.

I acknowledge immense love and care from Dr. A. K. Biswas and his family. I am indebted to him for his valuable suggestions from time to time and many important discussions regarding life, nation and society.

I am indebted to my friend Samudra for helping me in all my endeavors. I thank him for proof reading my thesis carefully.

I am grateful to canteen boys, my barbar, Kasi and my washerman for serving me at their best. The clean IIT surroundings with rich greenary pertain much to my growth.

I deeply acknowledge immense help and cooperation from Chaitali, my would be. Actually I have no words to express my gratitude to her. She has helped me in every possible way. In all my joys and sorrows she was by my side. I am deeply indebted to her for finalising my thesis work.

Lastly, I must say that it is because of constant encouragement and inspiration from my parents, I could finish my work successfully. I will ever remember their sacrifice and concern for me. At the end, I am glad to say that it is the blessings of my Guru Mataji alone which helped me to overcome all the hurdles in the path of completion of my Ph.D program.

*Amit Neogi*

# List of Publications

---

## In Refereed Technical Journals :

1. "Numerical modeling of laser matter interaction in the presence of an ambient gas", A. Neogi and R. K. Thareja, *Pramana* **50**, 63 (1998).
2. "Dynamics of laser produced carbon plasma expanding in low pressure ambient atmosphere", A. Neogi, A. Mishra and R. K. Thareja, *J. Appl. Phys.* **83**, 2831 (1998).
3. "Laser-produced carbon plasma expanding in vacuum, low pressure ambient gas and nonuniform magnetic field", A. Neogi and R. K. Thareja, *Phys. Plasmas* **6**, xxxx (1999).
4. "Dynamics of laser produced carbon plasma expanding in a nonuniform magnetic field", A. Neogi and R. K. Thareja, *J. Appl. Phys.* **85**, xxx (1999).
5. "Optical emission spectra of laser ablated carbon plasma in curved magnetic field", A. Neogi and R. K. Thareja, Communicated to *Appl. Phys.*
6. "Instabilities in laser produced carbon plasma expanding in a nonuniform magnetic field at low pressure ambient atmosphere", A. Neogi and R. K. Thareja, communicated to *Phys. Plasmas*.

# Contents

Synopsis	i
Acknowledgments	viii
List of Publications	x
List of Figures	xiii
List of Tables	xxi
List of Symbols	xxii
<b>1 Introduction</b>	<b>1</b>
1.1 Laser Matter Interaction . . . . .	4
1.1.1 Laser-Target Interaction . . . . .	6
1.1.2 Laser-Plasma Interaction . . . . .	7
1.1.3 Adiabatic Expansion of the Plume . . . . .	11
1.2 Computer Simulation . . . . .	12
1.3 Laser Ablated Plasmas in the Presence of an Ambient Atmosphere . . . . .	13
1.3.1 Recombination Process . . . . .	16
1.3.2 Charge Transfer . . . . .	17
1.3.3 Shock / Blast wave . . . . .	18
1.3.4 Microinstabilities . . . . .	19
1.4 Equilibrium in Plasmas . . . . .	21

1.5	Laser Plasma in Magnetic Field . . . . .	22
1.6	Diagnostics . . . . .	25
1.7	The Present Work . . . . .	27
<b>2</b>	<b>Experimental Techniques</b>	<b>29</b>
2.1	Optical Emission Diagnostics . . . . .	31
2.1.1	Electron Temperature . . . . .	31
2.1.2	Electron Density . . . . .	32
2.1.3	Plasma Expansion Velocity . . . . .	33
2.1.4	Vibrational Temperature . . . . .	33
2.2	Ion Probe Diagnostics . . . . .	34
2.2.1	Electron Temperature . . . . .	35
2.2.2	Ion Density . . . . .	35
2.3	Fast Photography . . . . .	36
<b>3</b>	<b>Numerical Modeling of Laser Matter Interaction in Presence of an Am- bient Gas</b>	<b>41</b>
3.1	Introduction . . . . .	41
3.2	Numerical Model . . . . .	42
3.2.1	In Vacuum . . . . .	42
3.2.2	In Ambient Gas . . . . .	47
3.3	Results . . . . .	54
<b>4</b>	<b>Laser Produced Carbon Plasma in Low Pressure Ambient Atmosphere</b>	<b>64</b>
4.1	Introduction . . . . .	64
4.2	Experimental Details . . . . .	65
4.3	Results and Discussion . . . . .	65
4.3.1	ICCD Photography . . . . .	65
4.3.2	Emission Spectroscopy . . . . .	67

<b>5</b>	<b>Laser Produced Carbon Plasma in a Nonuniform Magnetic Field</b>	<b>78</b>
5.1	Introduction . . . . .	78
5.2	Laser Produced Plasma in Magnetic Field . . . . .	79
5.2.1	Basic Equations of the Plasma in Magnetic Field . . . . .	79
5.2.2	Diamagnetic Behavior in Magnetic Field . . . . .	82
5.2.3	$\beta$ and Magnetic Reynold's Number $R_m$ . . . . .	83
5.3	Experimental Techniques . . . . .	85
5.4	Results and Discussions . . . . .	85
5.4.1	ICCD Photography . . . . .	85
5.4.2	Time Resolved Emission Spectroscopy . . . . .	96
5.4.3	Time Integrated Emission . . . . .	107
5.4.4	Langmuir probe spectra . . . . .	119
<b>6</b>	<b>Instabilities in a Laser Ablated Plasma Expanding in a Magnetic Field</b>	<b>123</b>
6.1	Introduction . . . . .	123
6.2	Rayleigh Taylor Instability . . . . .	125
6.3	Results and Discussion . . . . .	128
<b>7</b>	<b>Conclusion</b>	<b>137</b>
	<b>Appendix A</b>	<b>156</b>

# List of Figures

1.1	A schematic diagram showing different spatial zones of the plasma during laser matter interaction. . . . .	5
1.2	A schematic diagram showing laser plasma interaction in vacuum and the formation of shock wave moving into the target. . . . .	10
1.3	A schematic diagram showing the expansion of laser produced plasma and the formation of shock wave into the ambient gas. . . . .	19
2.1	Schematic of the experimental set up used in the experiment. Position of the magnet and target is shown separately. T: Target, MC: Monochromator, SO: Storage Oscilloscope SCR: Strip Chart Recorder, PG200: Pulse Generator, L1/L2: Convex Lens, ICCD: Intensified Charged Coupled Device. LP : Langmuir Probe. The magnetic field along Z and X axis is shown in the inset. . . . .	30
2.2	A schematic sketch of the probe. . . . .	34
2.3	(a) A schematic sketch of the ICCD detector and imaging field of view; 1. Object, 2. Image Intensifier, 3. CCD, 4. Nitrogen input port, 5 Coolant ports, 6. Gate shutter switch, 7. DB 25 connector for cable to controller, 8. BNC connector for HV signals from pulser, 9. Potentiometer for setting intensifier gain and (b) Different ports of ICCD. . . . .	37
2.4	A block diagram of the light path in the detector system. . . . .	39
2.5	Typical ICCD image of the plasma plume at 200 nsec delay from the ablating pulse. . . . .	40

3.1	(a) The moving shock front as seen from reference frame fixed to earth; (b) The stationary shock front as seen from reference frame moving with the shock front. . . . .	48
3.2	Region III is expanding plasma, region II is compressed gas and region I is the undisturbed gas shown in the reference frame fixed to the earth. $P_0 / (P_c)$ and $T_0 / (T_c)$ refer to pressure and temperature in region I and II respectively. . . . .	51
3.3	The position of the plasma front versus time in four different ambient gases (a) He (b) Ne (c) Ar and (d) Xe. Experiment (---) Simulation (—). . .	55
3.4	The simulated temporal profile of velocity of the plasma front in Xe gas. The inset shows the oscillations observed at around 300 ns on an enlarged scale. . . . .	56
3.5	The simulated temporal profile of shock intensity at the plasma front in case of plasma expanding in Xe gas. . . . .	57
3.6	Fig.3.3(d) and Fig.3.4 are replotted with a common time axis. . . . .	58
3.7	Temperature of the plasma front expanding in Xe and He as obtained from simulation. Dotted line is for the case of Xe and solid line for He as ambient gas. . . . .	59
3.8	Density of the plasma front expanding in Xe and He as obtained from simulation. Dotted line is for the case of Xe and solid line for He as ambient gas. The inset shows density of the plasma front expanding in He on enlarged scale neglecting the initial points. . . . .	59
3.9	Pressure of the plasma front expanding in Xe and He as obtained from simulation. Dotted line is for the case of Xe and solid line for He as ambient gas. . . . .	60



3.10	Electron density of the plasma front expanding in Xe and He as obtained from simulation. Dotted line is for the case of Xe and solid line for He as ambient gas. The inset shows electron density of the plasma front expanding in He on enlarged scale neglecting the initial points. . . . .	61
3.11	The simulated position of the plasma front as obtained from (a) Eqn.(3.24) i.e. no change in Navier-Stokes equation, (b) Eqn.(3.51) i.e. on adding viscous drag term only, (c) Eqn.(3.53) i.e. on adding viscous drag term and diffusive force term. . . . .	61
3.12	The electron density of the plasma front expanding in Ar, N <sub>2</sub> , He, H <sub>2</sub> as obtained from simulation. . . . .	62
3.13	The position of the plasma front versus time in 100 mTorr ambient air. Experiment (- - -), Simulation (—). . . . .	63
3.14	The temperature of the plasma plume versus time in vacuum. Experiment (- - -), Simulation (—). . . . .	63
4.1	The ICCD photographs of the carbon plasma plume (exposure time = 20 ns) at various time delays (a) 0.1 mTorr, (b) 5 mTorr and (c) 100 mTorr. . . . .	66
4.2	Spatial variation of the emission intensity of (a) CI, (b) CII, (c) CIII and (d) CIV transition in 0.1 mTorr, 5 mTorr and 100 mTorr of air. . . . .	69
4.3	Temporal profile of CI transition at 399.7 nm, CII transition at 426.7 nm, CIII transition at 465.0 nm and CIV transition at 580.1 nm. P1 and P2 are respectively first and second peak (shown only for the 100 mTorr case). Dashed line (- - -) is for P = 0.1 mTorr at a distance of (a) 10 mm (b) 10 mm (c) 12 mm (d) 8 mm. Dashed dot line (- . - . - .) is for P = 5 mTorr at a distance of (a) 10 mm (b) 10 mm (c) 12 mm (d) 8 mm. Solid line (—) is for P = 100 mTorr at a distance of (a) 10 mm (b) 10 mm (c) 8 mm (d) 8 mm. . . . .	71

4.4	Velocity of fast ( $P_1$ ) and slow peak ( $P_2$ ) for (a) CI, (b) CII and (c) CIII species at 5 mTorr and 100 mTorr air respectively, (d) velocity of CIV species at 5 mTorr and 100 mTorr air respectively. . . . .	72
4.5	The temporal profile of CI transition (at 14 mm), CII transition (at 16 mm), CIII transition (at 14 mm) at 5 mTorr of air. The slow peak $P_2$ is dominant in all the three cases. . . . .	75
4.6	Experimentally observed plume front is fitted with the equation $S_t = a_0 t^p$ . . . . .	77
5.1	ICCD pictures of the plasma at different delay times with 20 nsec exposure. The images are normalized with respect to the maximum intensity of each image. (a) Vacuum, (b) 100 mTorr air and (c) Variable magnetic field in vacuum. . . . .	86
5.2	The variation of the plume front with time in vacuum, air at 100 mTorr and magnetic field. The dotted lines connecting the points are only an aid to the eye. . . . .	87
5.3	Temporal variation of the volume of the plasma plume in vacuum, air at 100 mTorr and magnetic field. The lines connecting the points are only an aid to the eye. . . . .	88
5.4	The expansion of the plasma in three different positions of the target at 1000 ns delay with respect to the ablating laser pulse. (a) Target is at the middle of the poles; (b) the target is few mms towards the upper pole of the magnet; (c) target is more towards the lower pole. . . . .	90
5.5	A cross sectional area of the plume showing the direction of current within and at the boundary. The $\mathbf{J} \times \mathbf{B}$ force at the boundary accelerates the plume boundary giving rise to lobes which move towards the poles. . . . .	91
5.6	The velocity of the plume front with time. . . . .	92
5.7	The temporal behavior of maximum and mean intensity of ICCD photographs. The inset in fig. (b) shows expanded version of the variation of intensity in case of magnetic field. . . . .	93

5.8	The temporal variation of electron density calculated from the ICCD photographs. . . . .	94
5.9	The temporal behavior of electron temperature calculated from the ICCD photographs. . . . .	96
5.10	The $n_e$ and $T_e$ of the plasmoid expanding in vacuum, calculated from ICCD photographs has been fitted with equation of the form, $y = b_0 t^p$ . . . . .	97
5.11	Time resolved emission spectra of CII species in vacuum with magnetic field at (a) 4 mm, (b) 6 mm, (c) 8 mm and (d) 10 mm respectively along with the best fitted curve (solid line) and the fitting Gaussian functions (dotted lines).In the inset the dotted line represents the emission spectra without magnetic field and solid line represents FFT smoothed spectra of the magnetic field case. . . . .	98
5.12	Time resolved emission spectra of CIV species in vacuum with magnetic field at (a) 4 mm, (b) 6 mm, (c) 8 mm and (d) 10 mm respectively along with the best fitted curve (solid line) and the fitting Gaussian functions (dotted lines).In the inset the dotted line represents the emission spectra without magnetic field and solid line represents FFT smoothed spectra of the magnetic field case. . . . .	99
5.13	Time resolved emission spectra of CIII species in vacuum with magnetic field at (a) 14 mm, (b) 16 mm, (c) 18 mm and (d) 20 mm respectively along with the best fitted curve (solid line) and the fitting Gaussian functions (dotted lines).In the inset the dotted line represents the emission spectra without magnetic field and solid line represents FFT smoothed spectra of the magnetic field case. . . . .	100

5.14	Time resolved emission spectra of CI species in vacuum with magnetic field at (a) 14 mm, (b) 16 mm, (c) 18 mm and (d) 20 mm respectively along with the bestfitted curve (solid line) and the fitting Gaussian functions (dotted lines). In the inset the dotted line represents the emission spectra without magnetic field and solid line represents FFT smoothed spectra of the magnetic field case. . . . .	101
5.15	(a) ICCD images of the plume breaking into two symmetric lobes (at 1000 ns) when focal spot is exactly between the two poles. (b) Plume breaking into two asymmetric lobes (at 1000 ns) when focal spot is nearer to one of the poles. (c) Pictorial representation of (a). (d) Pictorial representation of (b). L1, L2, C refers to lobe 1, lobe 2 and central lobe. F1/(F2), I1/(I2), S1/(S2), refers to fast, intermediate and slow components of lobe 1 and lobe 2 respectively. . . . .	102
5.16	Schematic diagram of the direction of current density $\mathbf{J}$ giving rise to fast, intermediate and slow component. . . . .	105
5.17	Variation of electron temperature with distance with and without magnetic field. . . . .	106
5.18	Schematic diagram of three positions of the target at P, Q and R in magnetic field. The graph below shows the magnetic field strength at those points. . . . .	108
5.19	Time integrated emission spectra at three different positions in magnetic field (a) target kept at P and spectrum taken at P'; (b) target kept at Q and spectrum taken at Q'; (c) target kept at R and spectrum taken at R' and (d) $B = 0$ case. . . . .	109
5.20	Variation of relative intensity of the lines of (a) CII (426.7 nm) and (b) CIII (407.0 nm) transition with distance when target is kept at different positions in magnetic field and without magnetic field. . . . .	111

5.21	C <sub>2</sub> Swan band emission at 6 mm from the target when it is kept at position P of magnetic field. Transitions corresponding to (a) $\Delta v = -1$ ; (b) $\Delta v = 0$ and (c) $\Delta v = 1$ are shown in an enlarged scale. . . . .	112
5.22	Variation of relative intensity of C <sub>2</sub> band (516.5 nm) with distance when target is kept at different positions in magnetic field and without magnetic field. . . . .	113
5.23	Variation of electron temperature with distance, with and without magnetic field for different positions in magnetic field calculated from relative line intensity of the same ionic species. . . . .	114
5.24	Variation of electron temperature with laser fluence with and without magnetic field at a fixed distance (4 mm) from the target surface. . . . .	115
5.25	Schematic diagram of the distortion and compression of magnetic field lines when target is kept at different positions in magnetic field. . . . .	117
5.26	Motion of electrons and ions due to electromagnetic interaction and curvature gradient drift (a) positive field gradient with radius of curvature opposite to the direction of propagating plasma; (b) with the gradient less than case (a); (c) negative field gradient with the radius of curvature in the same direction of propagating plasma and (d) no magnetic field. . . . .	118
5.27	A typical Langmuir probe signal at a distance of 4 mm from the target and at a probe potential of + 10 Volt . . . . .	120
5.28	I-V characteristics of Langmuir probe signal for the case of plasma in presence and absence of magnetic field. . . . .	120
5.29	Square of the probe current is plotted against probe voltage and along with a straight line fit. . . . .	121
6.1	(a) Plasma (heavy fluid) supported by magnetic fluid (light fluid) against gravity; (b) Ripples at the surface got enlarged due to $\mathbf{E} \times \mathbf{B}$ drift giving rise to Rayleigh Taylor instability. . . . .	126

- 
- 6.2 The temporal profile of CII transition at 5 mTorr air pressure with and without magnetic field. . . . . 129
- 6.3 (a) Six different target positions in nonuniform magnetic field; (b) The variation of magnetic field strength along the direction of propagation of plasma. 130
- 6.4 Variation of delay of the second peak as a function of distance from the target position T1, T2, T3, T4, T5 and T6 respectively. . . . . 131
- 6.5 The onset distance for the occurrence of delayed second peak for different position of the target. . . . . 132
- 6.6 The dark line represents the temporal profile of CIII transition at 12 mm and the dotted line is at 14 mm. P1, P2 and P3 are the first, second and third peak respectively. The third peak does not appear at 14 mm. . . . . 132
- 6.7 A schematic diagram showing the expansion of plasma in magnetic in presence of air. The Rayleigh-Taylor instability gives rise to cracks or fissures which allows air to diffuse into the plasma giving rise to delayed second peak. 134
- 6.8 The ICCD images and intensity profile of the plume from ICCD photographs at 1000 and 1500 ns and 2000 ns. . . . . 135
- 6.9 The temporal variation of the velocity of the plume front calculated from ICCD photographs. The slope of the curve gives the deceleration in magnetic field. . . . . 136

# List of Tables

1.1	Various diagnostics and the corresponding plasma parameters. . . . .	26
4.1	Velocity of different species of carbon in 0.1 mTorr, 5 mTorr and 100 mTorr of air. . . . .	68
5.1	Velocity of carbon species with and without magnetic field in vacuum. . . .	104

# List of Symbols

---

$a$	=	acceleration
$a_1$	=	velocity of sound
$A$	=	atomic mass number
$A_i$	=	ion broadening parameter
$A_p$	=	area of the ion probe
$A'$	=	transition probability of upper level
$A''$	=	transition probability of lower level
$b_1$	=	width of the mixing zone
$B$	=	magnetic field
$c$	=	velocity of light
$C_p$	=	specific heat at constant pressure
$C_v$	=	specific heat at constant volume
$D$	=	thermal diffusivity
$D_\mu$	=	correction factor for detecting system
$e$	=	electron charge
$E$	=	electric field
$E_i, E_k$	=	energy of the transitions
$E_L$	=	energy deposited by the laser beam
$E_p$	=	explosive release of energy
$E_{th}$	=	ablation threshold
$E'$	=	excitation energy of upper level
$E''$	=	excitation energy of lower level
$\Delta E$	=	energy defect in electronic collision
$f_0$	=	initial perturbation
$f'$	=	perturbation
$F_{u'u''}$	=	Frank Gordon Factor
$g$	=	acceleration due to gravity
$g'$	=	statistical weights of upper level
$g''$	=	statistical weights of lower level
$G(u')$	=	term value of the upper vibrational level
$h$	=	Plank constant
$H$	=	enthalphy
$\Delta H$	=	latent heat



---

$I$	=	intensity
$I_0$	=	current
$I_L$	=	intensity of laser irradiation
$I_p$	=	probe current
$I_t$	=	total intensity
$I_{e0}$	=	electron saturation current
$I_{+0}$	=	ion saturation current
$I_{lm}^{u'u''}$	=	band head intensity
$J$	=	surface current
$J_c$	=	Joule's constant
$k$	=	propagation/wave vector of laser light
$k_B$	=	Boltzman constant
$K_w$	=	absorption coefficient
$L_s$	=	latent heat of sublimation
$L_{th}$	=	thermal diffusion length
$m$	=	particle mass
$m_e$	=	electron mass
$m_i$	=	mass of ion
$m_p$	=	number of photons
$M_s$	=	Mach number
$n$	=	number density
$n_1$	=	constant
$n_c$	=	critical density
$n_e$	=	electron density
$n_i$	=	ion density
$n_m$	=	magnetic viscosity
$N_i$	=	total number of ions
$N_e$	=	total number of electrons
$N_D$	=	number of particles in Debye sphere
$N_T$	=	total number of ablated species
$N_u'$	=	population in upper vibration level
$P$	=	pressure
$P_0$	=	initial pressure
$P_c$	=	pressure of the compressed region
$P_r$	=	power radiated by a black body
$P_L$	=	laser power
$q_c$	=	charge of the ion
$Q$	=	heat
$r_b$	=	bounce radius
$R$	=	resistance
$R_c$	=	three body recombination
$R_f$	=	reflectivity
$R_m$	=	magnetic Reynold's number
$R_R$	=	radiative recombination
$R_{cr}$	=	radius of curvature

---

$s$	=	density gradient scale length
$s_t$	=	propagation distance
$S$	=	area
$t_{ei}$	=	electron-ion thermalization time
$T$	=	temperature
$T_0$	=	isothermal temperature
$T_e$	=	electron temperature of plasma
$T_{vib}$	=	molecular vibrational temperature
$\Delta T$	=	maximum temperature rise
$\bar{u}$	=	mean velocity
$U$	=	initial energy
$v$	=	velocity
$v_0$	=	initial velocity of plume
$v_c$	=	drift velocity due to field curvature
$v_g$	=	drift velocity due to field gradient
$v_d$	=	drift velocity
$v_i$	=	ion streaming velocity
$v_P$	=	probe voltage
$v_{DE}$	=	gravitational drift velocity
$v_{DG}$	=	$\vec{E} \times \vec{B}$ drift velocity
$W$	=	work done
$W_e$	=	electron impact parameter
$W_s$	=	heating due to surface current
$x$	=	distance moved by plume
$X$	=	dimension of expanding plasma
$X_0$	=	initial orthogonal edges
$X_f$	=	stopping distance of plume
$\Delta x_t$	=	thickness of target material eV/pulse
$Y$	=	coordinate
$Y_0$	=	initial orthogonal edges
$z$	=	charge number
$\bar{z}$	=	average charge
$Z$	=	coordinate
$Z_0$	=	initial orthogonal edges

---

$\tau_L$	=	laser pulse duration time
$\omega_p$	=	plasma frequency
$\ln \Lambda$	=	coulomb logarithm
$\alpha_R$	=	radiative recombination coefficient
$\alpha_c$	=	three body recombination rate
$\sigma$	=	cross section for charge transfer
$\sigma_c$	=	coloumb collision cross section
$\mu$	=	reduced mass of ion
$\beta_s$	=	slowing coefficient
$\omega_1$	=	angular frequency
$\rho_1$	=	density of plasma
$\rho_0$	=	density of ambient gas
$\chi$	=	excitation potential of transition
$\tau$	=	period of oscillation
$\tau_p$	=	growth time of perturbation
$\gamma_e$	=	specific heat ratio for electrons
$\gamma$	=	specific heat ratio
$\gamma_g$	=	growth rate of instability
$\nu_L$	=	frequency of laser light
$\mu_0$	=	permittivity of free space
$\rho_s$	=	density of solid material
$\epsilon_I$	=	ionization potential
$\omega_L$	=	angular frequency of laser light
$\nu$	=	frequency
$\alpha$	=	absorption coefficient
$\epsilon_r$	=	kinetic viscosity
$\theta$	=	temperature difference
$\eta$	=	plasma resistivity
$\lambda$	=	magnetic field skin depth
$\beta$	=	ratio of magnetic pressure by particle pressure
$\phi$	=	flux

# Chapter 1

## Introduction

---

The importance of detailed investigation regarding laser produced plasma is increasing day by day not only because of rich physics underlying the phenomena but due to its numerous technological applications starting from pulsed laser deposition of thin films to its use in providing unique laboratory test beds for investigation of many astrophysical processes. The latest experimental techniques like ultrafast photography and computer simulations using extensive computer codes have helped the scientists to reveal the complicated physics underlying the process.

The laser produced plasma on account of its great versatility that its temperature ranges from 1 eV to multi keV and velocity of  $10^8$  cm/sec (1000 km/s) can be used as a physical model to study various astrophysical phenomena. The laser produced plasma flowing with high velocity in a static external magnetic field can be used to study astrophysical processes of stellar interiors. The sun emits a highly conducting plasma at supersonic speed of about 500 km/s into the interplanetary space as a result of supersonic expansion of solar corona which is known as solar wind. The ablation plasma has characteristics very much like solar wind [1] i.e. streaming velocities of several hundred km/sec and temperatures of a few eV, except that the laser-plasma has much higher density and is much smaller in size than the solar wind. At low background gas pressure ( $P < 1$  Torr), collisionless phenomena such as

those occurring when solar wind impinges on magnetospheric and ionospheric plasmas and with obstacles such as comet, moons and planets dominate. At high pressure ( $> 1$  Torr) collisional interstreaming plasma effects such as blast wave formation [2] are generated which behaves like supernova shocks. Plasma (heavy fluid) expanding in magnetic field (light fluid) undergoes Rayleigh-Taylor instability at the boundary similar to that observed in AMPTE barium cloud experiment in the tail of magnetosphere (about 12 earth radii away) [3]. Marked striations appeared as the barium plasma expanded to its maximum radius. The collimation and stability properties of plasma flow across magnetic field is of particular relevance to the propagation of charged particle beams, solar wind evolution and astrophysical jets [4, 5]. These jets are similar to that observed in laboratory plasmas about 3 kG magnetic field via  $\vec{E} \times \vec{B}$  drift. The propagation of laser produced plasma in curved magnetic field resembles the flow of charged particle in curved magnetic field of earth in the earth magnetosphere which gives rise to ring current flowing westward [6]. Understanding astrophysical phenomena such as the theory of white dwarf structure (mean densities  $\sim 10^5 - 10^8$  gm/cm<sup>3</sup>) requires an understanding of high density effects; laser plasma interaction has been utilized to measure the microscopic structure of the dense plasmas. Quantitative measurements of radiative opacity is of considerable interest to astrophysicists where laser produced plasma can be utilized [7]. Turbulence structures are seen in a wide variety of space and astrophysical situations like solar wind behind the bow shock, supernova remnants and other astrophysical processes. These effects can be studied from laser produced plasma where turbulence is observed [8]. Since carbon has high cosmical abundance so spectroscopy of carbon plasma owes its importance to astrophysical processes [9].

Laser ablated plasma is a multifunctional fluid because of its chemical reactivity, working gas selectivity and high energy density. Therefore, applications of plasma in material technology such as thin film deposition [10], production of microclusters [11], micromachining of metals, plastics and ceramics [12], chemical treatment of surface layers [13], fabrication of microelectronic devices [14], propulsion of space vehicle [15], magnetohydro-

dynamic generators [16] and for environmental control have been developed extensively [17].

Laser ablation is being intensely studied and used in the computer chip industry for drilling printed circuit boards. Micromachining is also useful in surgery, most notably for kidney stones (lithotripsy) and eyes [18] (corneal and keratorefractive surgery). Laser ablation with very intense laser energies is being investigated as a possible X-ray source for X-ray lithography, as a possible commercial environmental friendly source of electricity by inducing fusion reactions (Inertial Confinement Fusion) [19], and as a possible laser gain medium for X-ray lasers.

The application of laser ablation in the deposition of thin films onto substrates is increasingly getting popular day by day due to its various advantages over other deposition techniques. This technique can be used to deposit thin film of almost any material irrespective of its optical properties [20] because under high power laser irradiation most of the materials turn optically opaque by an optical breakdown. Stoichiometry is maintained between the target material and the deposited film in this process. The technique offers very high instantaneous growth rate and deposition can be carried out at relatively lower temperature due to very high kinetic energy of the laser ablated plasma species [21]. The process is relatively simple, inexpensive and free of contamination. It is possible to obtain high density films with good adhesion due to the presence of energetic species during the deposition process. The laser ablated deposition is mostly done in presence of gas e.g. oxygen for the deposition of superconducting films [22, 23] to incorporate gas in the deposited films. Laser ablated carbon plasma in an ambient gas has been used for deposition of  $C_{60}$  and diamond like carbon on various substrates [24]. The dynamics of laser plasma is observed to change in presence of gas [25]. Thus, the knowledge of the dynamics of the plasma expanding in ambient atmosphere is indispensable for fabricating high quality films.

Magnetic field effectively controls the local plasma thermofluid characteristics from both macroscopic and microscopic view points [26, 27] and hence is important from the

point of view of industrial applications: The knowledge of laser produced plasma expanding in magnetic field helps to elucidate our understanding regarding beam heating of magnetically confined thermonuclear plasma [28], bipolar flows associated with young stellar objects, interaction of solar winds with planetary atmosphere, formation of jets [29] etc. Further more, laser produced plasma in an externally applied magnetic field has been found to be a rich source of X-ray emission [27]. Few works have also been reported about change of material properties in magnetic field [30, 31].

It is imperative to understand the physics of laser matter interaction in order to control various processes efficiently for various applications. A simplistic overview of laser matter interaction is presented below.

## 1.1 Laser Matter Interaction

The process of laser matter interaction is the subject of many theoretical [32-35] and experimental [36-39] studies. The process can broadly be divided in three regimes.

1. Interaction of laser beam with the target material resulting in evaporation of the surface layer (Evaporation regime).
2. Interaction of plasma with the incident laser beam resulting in an isothermal plasma and expansion (Isothermal regime).
3. Adiabatic expansion of the plume (Adiabatic regime).

The first two regimes start with the laser pulse and continue until the laser pulse duration. The last regime starts after the laser pulse terminates. Figure 1.1 shows different spatial zones of the plasma along with the different temperature and density regions plotted on the same scale. The laser light is incident from the right hand side on to a planar solid target. At  $t < 0$  the space is occupied by a cold dense material with a uniform density  $\rho_s$ . For  $t > 0$ , material is heated by the laser beam and four different zones are formed. In

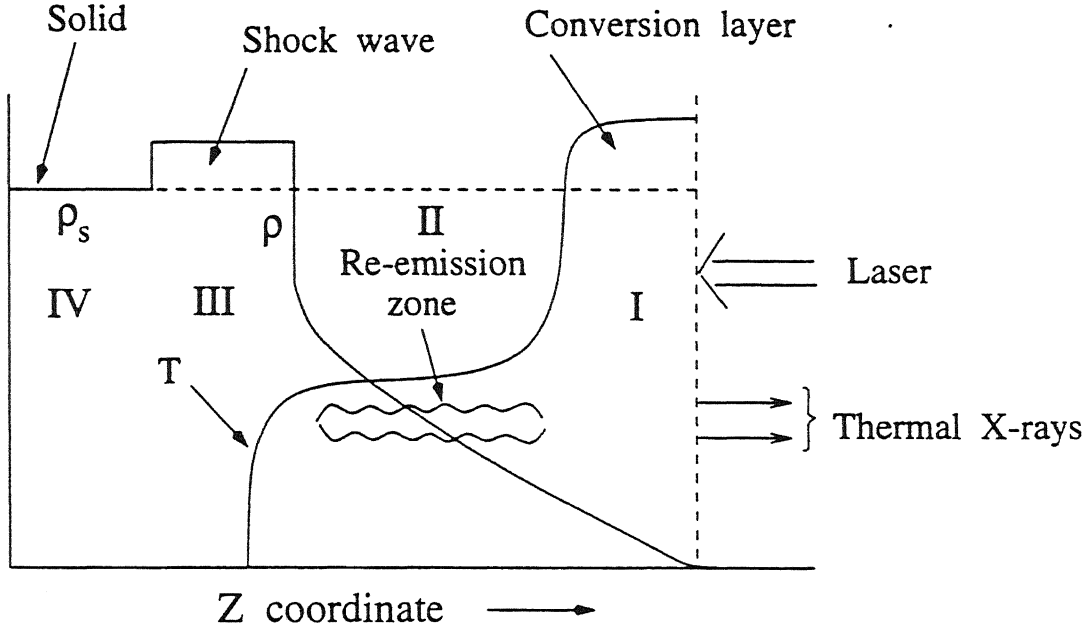


Figure 1.1: A schematic diagram showing different spatial zones of the plasma during laser matter interaction.

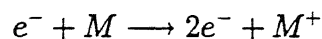
the *conversion layer (CL)* laser radiation is absorbed and partially converted into thermal x-rays. Its characteristics depend upon the wavelength of the laser light, electron heat conduction and the emission coefficient of the plasma for thermal radiation. It has lowest density and highest temperature of all the zones. It radiates equally towards the vacuum as well as towards the solid target. Next is the *re-emission zone (RZ)* where the radiation emitted towards the solid target is absorbed. It emits radiation through the conversion layer into the vacuum. Physically the re-emission occurs by multiple absorption and re-emission as the energy supplied by the conversion layer diffuses towards the solid target. The re-emitted radiation is transmitted through the optically thin conversion layer and contributes to the thermal x-ray radiation into vacuum. It has relatively lower temperature and higher density in comparison to conversion layer. These two zones (I and II) are coupled only by radiation. Next is *shock wave (SW)* region where the recoil momentum of the expanding layer is absorbed. However, because of its large density, the energy transmitted to the shock wave may be neglected. Finally, the *undisturbed solid* which is solid material zone whose density is unchanged. Since there is large difference in density the



plasma flow can be distinguished in different zones. The details of laser target interaction and laser plasma interaction is described below.

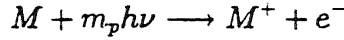
### 1.1.1 Laser-Target Interaction

The interaction of laser light with the target surface depends on factors like laser fluence, pulse width, wavelength of the laser light and temperature dependent optical and thermo-physical properties of the material [20, 40-41]. For low laser irradiation ( $\sim 10^6 \text{ Watt/cm}^2$ ) the absorbed radiation appears as heat which is evenly distributed throughout the material by thermal diffusion. In case of metals, the conduction electrons absorb the laser photons and are excited resulting in increase in kinetic energy of the electrons. Due to increase of kinetic energy of the electrons, the collision frequency increases which results in rise in temperature of the material [42]. At higher laser irradiation ( $> 10^6 \text{ Watt/cm}^2$ ), depending on the thermal conductivity, thermal diffusivity, reflectivity of the target material and the parameters of the laser pulse, intense local heating of the surface occurs resulting in a rise in surface temperature of the material. As the irradiation increases the temperature of the surface increases and a molten pool of depth  $(D\tau_L)^{1/2}$  is formed [20], where  $D$  is thermal diffusivity and  $\tau_L$  is the laser pulse duration time. A further increase in the irradiation will cause the surface temperature of the molten pool to reach boiling point resulting in evaporation. This will happen when the energy deposited approximately equals the latent heat of sublimation [20]  $L_s \text{ (erg/gm)} \simeq I_L \tau_L^{0.5} \rho_s^{-1} D^{-0.5}$  where  $\rho_s$  is the density of the solid target and  $I_L$  is the intensity of laser irradiation. Once the vapours are formed, the laser light will cause further heating resulting in plasma formation. There are mainly two mechanisms described below which help in electron generation and plasma formation [14]. The first mechanism involves absorption of laser radiation by electrons when they collide with neutrals. If electrons gain sufficient energy they can cause ionization



The electron concentration will increase exponentially with time leading to cascade breakdown.

The second mechanism called a multiphoton ionization involves the simultaneous absorption by an atom or molecule of a sufficient number of photons to cause its ionization or to eject an electron from the valence to the conduction band.



If  $\epsilon_I$  is the ionization potential (or band gap) the number of photons  $m_p$  must exceed the integer part of  $(\frac{\epsilon_I}{h\nu} + 1)$ . Multiphoton ionization is important only at short wavelength ( $\lambda < 1 \mu\text{m}$ ).

Both cascade and multiphoton ionization require high laser irradiance usually, in excess of  $10^8 \text{ Watt/cm}^2$ . However, breakdown of solids has been observed at low irradiance  $\sim 10^6 \text{ Watt/cm}^2$  in the presence of a static electric field [43]. If the solid is absorbing or has microscopic absorption sites, a third mechanism called thermal runaway has been proposed to explain the low thresholds.

The amount of material evaporated can be calculated using energy balance considerations. The energy deposited by the laser beam on the target ( $E_L$ ) is equal to the energy needed to vaporize the surface layers, the conduction losses in the target and the losses due to absorption of the laser energy by the expanding plasma. This is given by the energy threshold  $E_{th}$  which represents the minimum energy above which appreciable evaporation occurs. The thickness of the target material evaporated/pulse ( $\Delta x_t$ ) is given by [44]

$$\Delta x_t = (1 - R) \left[ \frac{E_L - E_{th}}{\Delta H + C_v \Delta T} \right] \quad (cm) \quad (1.1)$$

where  $R$ ,  $C_v$ ,  $\Delta T$  and  $\Delta H$  represent the reflectivity, specific heat at constant volume, maximum temperature rise and latent heat rise respectively. This equation is valid for conditions where the thermal diffusion length  $L_{th} = (2D\tau_L)^{1/2}$  is larger than the absorption length of the laser beam in the target material.

### 1.1.2 Laser-Plasma Interaction

The interaction of the laser beam with the solid target leads to vaporization of the surface resulting in emission of positive ions and electrons giving rise to a plasma. Once the

primary plasma is formed, the incoming laser radiation is absorbed by a process known as inverse Bremsstrahlung. In this process an electron comes in the field of an ion of charge  $ze$ , gets accelerated, absorbs a laser photon and separates out. The absorption coefficient is given by

$$\alpha = 3.69 \times 10^8 \left[ \frac{z^3 n_i^2}{T_e^{0.5} \nu^3} \right] \left[ 1 - \exp \left( \frac{-h\nu_L}{k_B T_e} \right) \right] \text{ cm}^{-1} \quad (1.2)$$

Where  $z$ ,  $n_i$  and  $T_e$  are respectively the average charge, ion density and temperature of the plasma and  $h$ ,  $k_B$  and  $\nu_L$  are the planck constant, Boltzmann constant and frequency of the laser light respectively. The term  $[1 - \exp(-h\nu_L/k_B T_e)]$  represents the loss due to stimulated emission which depends on the plasma temperature and laser frequency. For  $1.06 \mu\text{m}$  laser wavelength, the exponential term becomes unity for  $T_e < 13600 \text{ K}$  and can be approximated by  $h\nu_L/k_B T_e$  for  $T_e > 13600 \text{ K}$ . The absorption term shows a  $T^{0.5}$  dependence for low temperature and  $T^{1.5}$  for high temperature. The dependence of frequency also changes from  $\nu_L^2$  to  $\nu_L^3$  depending on the value of  $(h\nu_L/k_B T_e)$ . Eqn.(1.2) shows that rate of absorption depends on  $n_i^2$ . This results in increase in KE of the electrons which increases collision frequency. The energy absorbed by the electron is transferred to the ions by the electron ion collisions. The ions get more and more ionised resulting in increase in electron density. However, this process cannot go on indefinitely. The electromagnetic wave (laser) propagating through the plasma obeys the dispersion relation of the form

$$\omega_L^2 - \omega_p^2 = k^2 c^2 \quad (1.3)$$

$$\omega_p = \left( \frac{4\pi n_e e^2}{m_e} \right)^{1/2} \quad (1.4)$$

Where  $\omega_L$  is the angular frequency of laser light,  $k$  is the propagation vector,  $c$ , the velocity of light,  $e$ , the electron charge,  $n_e$ , the electron density  $m_e$ , the electron mass and  $\omega_p$  is the plasma frequency. For  $\omega_L > \omega_p$ ,  $k$  is real and the electromagnetic field propagates whereas for  $\omega_L < \omega_p$ ,  $k$  is imaginary and the wave is not propagated. At  $\omega_L = \omega_p$ , reflection of light occurs at a density called the critical density  $n_c = m_e \omega_L^2 / 4 \pi e^2$

At the beginning of the inverse Bremsstrahlung process  $\omega_L \gg \omega_p$  and rate of absorp-

tion depends on  $n_i^2$ . The absorbed energy causes an increase in the kinetic energy of the electrons i.e. an increase in electron temperature which in turn produces further ionization with a consequent increase in  $n_e$  and eventually approaches  $n_c$  the critical density. The critical density extends across a plane surface some distance into the plasma. The value of  $n_c$  is  $3.15 \times 10^{21}/\text{cm}^3$  for  $1.06 \mu\text{m}$  wavelength laser light from Nd:YAG laser. At this distance the plasma becomes opaque to the incoming radiation at the surface which causes laser light to get reflected. Laser light can no longer reach the target surface to generate new plasma. However, plasma growth does not cease. Because of the heating which follows the absorption of energy by inverse Bremsstrahlung, the plasma is driven rapidly away from the target surface resulting in decrease in electron density and laser light again reaches the surface. The energy absorbed by the electron equilibrates very rapidly so that a well defined electron temperature is reached. The energy gained by the electrons is also shared with ions in collisions. These processes do not take place discontinuously but merge into a smooth self regulating regime with the generation, heating and expansion of plasma taking place throughout the laser pulse. The expanding plasma generates pressure which drives a shock wave into the solid material as shown schematically in Fig.1.2. The situation is analogous to rocket take off condition where the hot gas exhaust result into a net upward thrust.

The energy absorbed by the electron equilibrates very rapidly so that a well defined electron temperature is reached. The time required to attain equilibrium (the electron-ion thermalization time) is given by [45]

$$t_{ei} = 2.52 \times 10^8 \frac{AT_e^{3/2}}{n_e z^2 \ln \Lambda}. \quad (1.5)$$

Where A is the atomic mass number and  $\ln \Lambda \simeq 10$  represents the coulomb logarithm for laser plasma. For laser produced carbon plasma,  $t_{ei}$  is considerably less ( $\sim 10^{-10}$  sec) than the duration of a Q-switched laser pulse ( $10^{-8}$  sec) and so a good degree of thermalization is expected in the plasma.

At higher irradiances ( $> 10^{12}$  Watt /  $\text{cm}^2$ ) the laser ablated plasma is heated to a

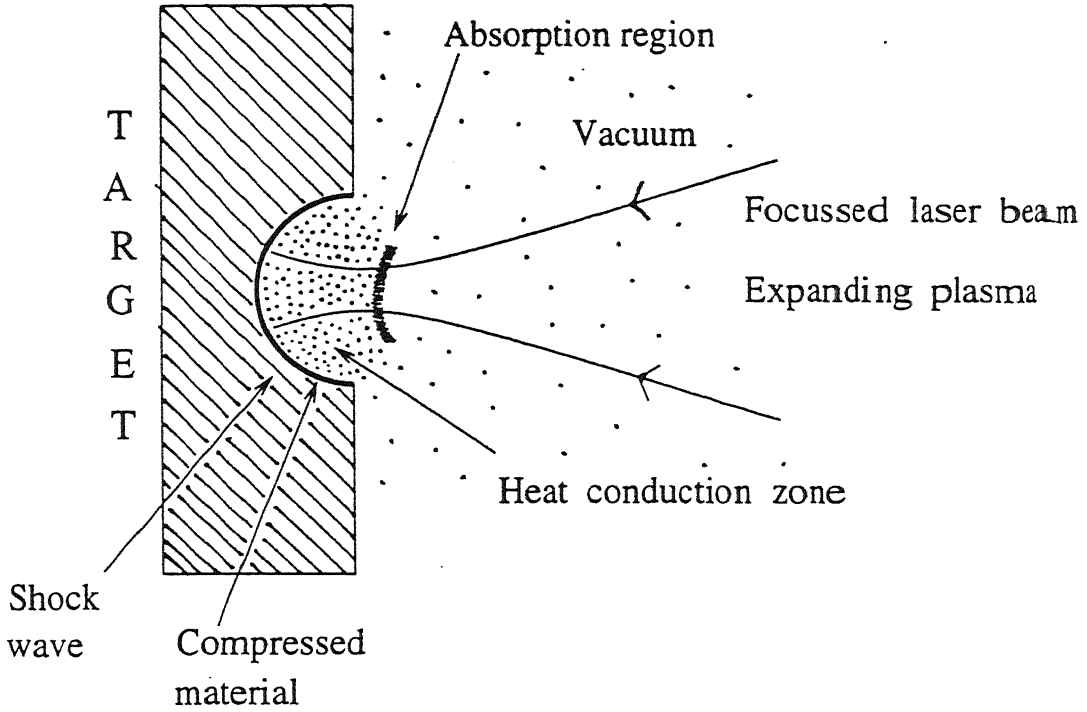


Figure 1.2: A schematic diagram showing laser plasma interaction in vacuum and the formation of shock wave moving into the target.

very high temperature in a thin absorbing layer at the surface of the dense regime and has only a small optical thickness, so the self regulating regime fails to exist. Absorption becomes non-collisional and takes place via resonance mode conversion at critical density. This regime has been investigated in one dimension by Fauquignan *et. al.* [46]. These plasmas are used for studying dynamics of strongly coupled plasmas [8], short wavelength lasers [47, 48] and for astrophysical like plasmas [8].

In the initial stages of plasma expansion when the particle density is of the order of  $10^{19} - 10^{20}/\text{cm}^3$ , the mean free path of the particles is short, and the plasma behaves as a continuum fluid. The equation of gas dynamics can be applied to simulate its expansion [49].

$$\frac{\partial n}{\partial t} + \nabla \cdot (nv) = 0 \quad (1.6)$$

$$nm\left(\frac{\partial v}{\partial t}\right) + (v \cdot \nabla)v = -\nabla P \quad (1.7)$$

where  $n$  is the number density,  $m$ , the mass of the particle,  $v$ , the velocity and  $P$  is the pressure. The density of the plasma can be expressed as [44]

$$n(x, y, z, t) = \frac{N_T t}{\sqrt{2\pi^{1.5}} \tau_L X(t) Y(t) Z(t)} \exp \left[ -\frac{x^2}{2X(t)^2} - \frac{y^2}{2Y(t)^2} - \frac{z^2}{2Z(t)^2} \right] \quad (1.8)$$

where  $N_T$  is the total number of ablated species at  $t = \tau_L$  (pulse width).  $X(t)$ ,  $Y(t)$  and  $Z(t)$  are the dimensions of the expanding plasmas in the three orthogonal directions. Assuming plasma to be an ideal gas, the pressure at any point can be expressed as

$$P(x, y, z, t) = n(x, y, z, t) k_B T \quad (1.9)$$

It has been shown that gas dynamic equations follow similarity transformation [50] in which the velocity can be expressed as

$$v = \frac{x}{X(t)} \frac{dX(t)}{dt} \hat{i} + \frac{y}{Y(t)} \frac{dY(t)}{dt} \hat{j} + \frac{z}{Z(t)} \frac{dZ(t)}{dt} \hat{k} \quad (1.10)$$

The equation of motion derived from the above equations is

$$X(t) \left[ \frac{1}{t} \frac{dX}{dt} + \frac{d^2 X}{dt^2} \right] = Y(t) \left[ \frac{1}{t} \frac{dY}{dt} + \frac{d^2 Y}{dt^2} \right] = Z(t) \left[ \frac{1}{t} \frac{dZ}{dt} + \frac{d^2 Z}{dt^2} \right] = \frac{k_B T_0}{m} \quad t \leq \tau_L. \quad (1.11)$$

Where  $T_0$  is the isothermal temperature of the plasmas. The above equation determines the initial expansion of three orthogonal plasma edges. The initial dimensions of the plasma are of the order of mm in the transverse direction whereas in the perpendicular direction they are less than 1  $\mu\text{m}$ . Eqn.(1.11) shows that during initial expansion stage, when the velocities are small, the acceleration is very high. With an increase in expansion velocity, acceleration starts to decrease and ultimately becomes zero resulting in an elongated plasma shape. Since the plasma dimensions are much smaller along the target normal than in the transverse direction, the expansion is anisotropic in nature.

### 1.1.3 Adiabatic Expansion of the Plume

After the termination of laser pulse, no particles are evaporated or injected into the inner edge of the plasma and the expansion is mostly adiabatic. The thermal energy rapidly gets converted into kinetic energy giving higher expansion velocity of the plasma. Using

the adiabatic equation of state for the expansion of plume after the termination of laser pulse, we have

$$T[X(t)Y(t)Z(t)]^{\gamma-1} = \text{Constant} \quad (1.12)$$

$$\frac{1}{P} \left[ \frac{\partial P}{\partial t} + \mathbf{v} \cdot \nabla P \right] - \frac{\gamma}{n} \left[ \frac{\partial n}{\partial t} + \mathbf{v} \cdot \nabla n \right] = 0 \quad (1.13)$$

$$\frac{\partial T}{\partial t} + \mathbf{v} \cdot \nabla T = (1 - \gamma)T \nabla \cdot \mathbf{v} \quad (1.14)$$

where  $T$  is the temperature,  $n$  and  $P$  remains similar as before

$$n(x, y, z, t) = \frac{N_T}{\sqrt{2\pi^{1.5}} X(t)Y(t)Z(t)} \exp \left[ -\frac{x^2}{2X(t)^2} - \frac{y^2}{2Y(t)^2} - \frac{z^2}{2Z(t)^2} \right] \quad (1.15)$$

Solving the above equation one obtains the following equation of motion for the adiabatic regime,

$$X(t) \left[ \frac{d^2 X}{dt^2} \right] = Y(t) \left[ \frac{d^2 Y}{dt^2} \right] = Z(t) \left[ \frac{d^2 Z}{dt^2} \right] = \frac{kT_0}{m} \left[ \frac{X_0 Y_0 Z_0}{X(t)Y(t)Z(t)} \right]^{\gamma-1} \quad t > \tau_L. \quad (1.16)$$

where  $X_0$ ,  $Y_0$ ,  $Z_0$  are the initial orthogonal edges of the plasma after the termination of laser pulse ( $t=\tau_L$ ) that is after the isothermal regime. In this regime, the initial transverse dimensions are much larger than the perpendicular dimension which correspond to the expansion length in isothermal region. As the velocities are dictated by these lengths, the highest velocity is in the direction of smallest dimension. This gives rise to the characteristic plasma shape elongated outward from the surface.

## 1.2 Computer Simulation

The description of laser matter interaction given in the last section is very simplistic and does not take into account many important processes like loss of energy through Bremsstrahlung radiation by electrons etc. The studies related to laser produced plasma involve variety of complex phenomena like driver (laser or ion beam) interaction with the plasma, charged particle transport and collisional processes, nuclear fusion reaction kinematics, hydrodynamics and thermodynamics of the plasma etc. The simultaneous presence of these phenomena necessitates invoking of numerical methods in the form of

computer codes which simulate various processes taking place in the plasma. Each and every process having some significance is considered in the model and is dealt with one by one along with their inter-effects. The term simulation is referred to as "It is an activity whereby one can draw conclusions about the behavior of a given system by studying the behavior of a corresponding model whose cause and effect relationship is same as (or similar) to those of the original system". Computer simulation study is actually a form of numerical experimentation in which mathematical model takes the place of an experimental facility. In the past, several computer codes have been developed with the ultimate aim of studying laser produced plasma and inertial confinement fusion. The name of few of them are MEDUSA [51], CASTOR [52], LASNEX [53], MINIRA [54], ILESTA [55], HIMICO [56], MULTI (1-D) [57] *etc.* We have modified 1-D Lagrangian code Medusa (version MED-101) for our work [58].

### 1.3 Laser Ablated Plasmas in the Presence of an Ambient Atmosphere

The interaction of laser ablated plumes with background gases is receiving increased attention due to its increasing need in technological applications and is the subject matter of theoretical and experimental investigations. Knight [33] developed a theoretical model where homentropic expansion of vapor against an ambient atmosphere has been examined applying conservation of mass, momentum and energy across the Knudsen layer. Belantone *et al* [59] generalised the model where entropy can vary with time that is the homentropic assumption of previous case is relaxed and the more general case of flow can be examined but its usage is restricted to a relatively low intensity regime. Aden *et al* [32] extended the previous case from one dimensional to three dimensional model which matched well with their experimental data and showed that there exists a material dependent minimal laser intensity where the vapor properties at the vaporization front become independent from further expansion of the plasma against the ambient gas. Macfarlane *et al* [34] had given a one dimensional model where radiation hydrodynamics calculations



are performed to study the structure and evolution of blast waves resulting from laser-generated plasma expansions for the ambient pressure ranging from 25 mTorr to 5 Torr. Giuliani *et al* [35] had given a numerical model where laser target and debris-background interactions are modeled solving mass continuity, total momentum and separate ion and electron internal energy equations. The model is appropriate for background pressures greater than 1 Torr. Ananin *et al* [60] had given a model for plasma expansion at low pressure ambient gas of the order of 0 - 1 Torr. The analysis is based on multifluid gas dynamics approach because of diffusion of external gas particles into the laser plasma. The blast wave formation and shock is well described analytically by self similar solutions derived by Sedov [61] which works well at higher pressure. The model is true for an instantaneous point explosion and with negligible radiation losses. However, the model is insufficient for getting the detailed thermodynamic and hydrodynamic properties of the blast wave. In low gas pressure the plume propagation could be described by Monte Carlo simulation [62]. Recently a numerical model has been proposed where Navier Stokes equation for the case of vacuum is modified by incorporating viscous drag force and diffusive force. The boundary conditions relate to Rankine-Hugoniot conditions for shock wave [58].

The behavior of laser produced carbon plasma expanding in an ambient atmosphere has been investigated experimentally in the recent past. Carbon plasma expanding in an ambient air [39], helium [63], argon [64] atmosphere has been studied extensively. Line emission enhancement in laser-ablated carbon plasmas in ambient helium and argon gas at various pressure is studied by Abhilasha and Thareja [65]. Role of ambient gas (helium and argon) on laser ablated plumes for thin carbon film deposition has been discussed by Thareja *et al* [66]. Geohegan *et al* [67] has discussed the role of He, Ne, Ar and Xe at high pressure (300 Torr) on the propagation dynamics of laser ablated graphite. The interaction of laser ablated plumes with background gas is receiving increased attention due to its importance for film growth by pulsed laser deposition [68-75] particularly for deposition of high  $T_c$  superconductors [76-78], polymeric thin films [79], diamond like carbon films [80-82], TiN films in presence of  $N_2$  [83] and ceramic thin films [84]. At higher

gas pressures laser ablation can be utilized to produce novel clusters such as fullerenes and doped fullerenes [85, 86]. Real time investigation of the plume dynamics during laser ablation of germanium in an oxygen environment has been reported by Vega *et al* [87]. Correlation between target-substrate distance and oxygen pressure in pulsed laser deposition of  $\text{YBa}_2\text{Cu}_3\text{O}_7$  has been discussed by Kim *et al* [88]. Anomalous enrichment of  $\text{C}_2^-$  ions by the laser ablation of graphite in Ar jet has been observed by Park *et al* [89]. Formation of shock wave structure during expansion of a laser plasma in a low-density [90-92] and high density gas [93] has also been investigated.

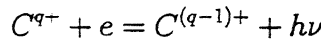
There have been several reports on propagation of laser produced plasmas in ambient atmosphere, however, the dynamics of carbon plasma expansion in ambient gas at low pressure is still not clear. The principal diagnostics technique like emission spectroscopy [34, 94-97], laser induced fluorescence [38, 98], langmuir probe [99-102], streak photography [103, 71], ICCD photography [104, 105] etc have been used to study laser produced plasmas. The plasma propagating in low pressure ambient atmosphere splits into two components, fast and slow components [25]. Some researchers proclaim that Rayleigh-Taylor instability occurring due to the difference in density of the propagating plasma and the external ambient gas to be the major cause of this stratification into slow and fast components [103, 25]. For high background pressure and at later time a blast wave model describes well the position of luminous shock front whereas at low pressure and at early time better fit is obtained from classical drag force model [78]. However, these models fail to predict the fast component of the propagating plume. Attempts have been made to simulate the occurrence of slow and fast components numerically by introducing a dynamic source effect that accelerates the expansion of laser ablated material in the direction perpendicular to the target [106]. A theoretical model based on a combination of multiple inelastic scattering and hydrodynamic formulation gives good fit to experimental data for Si in He and Ar [100]. The stratification of the plasma plume as observed by fast photography is in accordance with time resolved emission spectroscopy [105].

The plasmas produced in an ambient atmosphere differ significantly from that pro-

duced in vacuum. Laser plasma expansion in low density gas can broadly be divided into two categories viz. 0-1 Torr and above 1 Torr. At low pressure (0-1 Torr), the mean free path of plasma ions either exceeds or is comparable with the dimension of the experimental chamber ( $\sim 10$  cm), there is a strong interpenetration of the laser plasma and the ambient low density gas [60]. Above 1 Torr pressure the laser plasma expansion results in the appearance of a shock wave structure in the gas [106]. Various processes like recombination, charge transfer, collisional and collisionless interactions, shock/blast wave interactions, microinstabilities in the laser plasma occur during laser plasma expanding in ambient gas. They are briefly described below.

### 1.3.1 Recombination Process

When an ion and electron collides, particularly at low relative velocity, they have a finite probability of recombining into a neutral atom. To conserve momentum a third body must be present. If this third body is an emitted photon, the process is called radiative recombination. If it is a particle, the process is called three-body recombination [107, 108]. For the radiative recombination



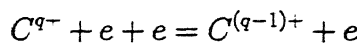
The radiative recombination rate  $R_R$  being given by

$$R_R = \left[ \frac{dn_e}{dt} \right]_R = -\alpha_R n_e n_i \quad (1.17)$$

where  $\alpha_R$  is the radiative recombination coefficient,

$$\alpha_R = 2.7 \times 10^{-13} z^2 T_e^{-3/4} \quad \text{cm}^3/\text{s} \quad (1.18)$$

where  $n_e$  and  $n_i$  are the electron and ion densities, respectively;  $T_e$  is electron temperature in eV and  $z$  is ionic charge. Three body recombination process is defined as



Three body recombination rate  $R_c$  being given by

$$R_c = \left[ \frac{dn_e}{dt} \right]_c = -\alpha_c n_e^2 n_i \quad (1.19)$$

where  $\alpha_c$  is the three body recombination coefficient,

$$\alpha_c = 9.2 \times 10^{-27} z^3 T_e^{-9/2} \ln[(z^2 + 1)^{1/2}] \quad \text{cm}^6/\text{s} \quad (1.20)$$

From Eqs. (1.18) and (1.20) it follows that radiative process is important only close to the target surface and the three body recombination is a dominant process beyond a few mm from the target surface.

### 1.3.2 Charge Transfer

When an ion enters into the vicinity of a neutral/ionic particle, there is a finite possibility that an electron may be transferred from the neutral/ionic particle to the other ion and thereby exchange takes place [109]. This process is referred to as charge transfer and is represented by



The quantity  $\Delta E$  is called the energy defect in the electronic collision. The energy dependence of the cross section for a particular charge-transfer reaction depends upon the magnitude of the energy defect. The charge-exchange rate of ions is given by the relation

$$R = n_i \langle v_i \sigma \rangle \quad (1.22)$$

where  $v_i$  is ion streaming velocity, and  $\sigma$  the cross-section for the charge transfer. The cross section for the ion-ion charge transfer interaction is given by [109]

$$\sigma(z_1, z_2) = \frac{4\pi z_1^2 z_2^2 e^4 \ln \Lambda}{\mu^2 \bar{v}_i^4 [1 + m_{i2}/m_{i1}]} \quad (1.23)$$

where index 1 refers to the laser plasma ions, 2 to the ambient gas ions,  $z$  is the charge number,  $\ln \Lambda \simeq 10$  is the Coulomb logarithm for the laser plasma,  $\bar{v}$  the mean velocity of laser plasma ions,  $m_i$  the mass of ion and  $\mu$  the reduced mass of ions. The cross-section  $\sigma$ , for the conditions of our experiment is  $\simeq 10^{-18} \text{cm}^2$ . Seely *et. al.* [110] have examined the

charge exchange process occurring between C VII and Ar III in expanding laser produced carbon plasma in details.

### 1.3.3 Shock / Blast wave

In case of plasma expanding in an ambient gas ( $\simeq 1$  Torr), the laser plasma acts like a plunger which forms a shock wave in the gas and there is a contact boundary between the gas and the laser plasma as shown in Fig.1.3. The background gas is compressed into a thin shell at the shock front. As the shock front expands, more and more of the background gas is swept up by the shock wave resulting in decrease in the expansion velocity of the laser produced plasma. This kind of unsteady shock wave is known as blast wave. For high background pressure a blast wave model [50, 111, 112] has been used to describe the luminous shock front caused by the expansion of laser produced plasmas. This model is similar to a shock wave caused by an point explosion with an explosive release of energy  $E_L$ , through a background gas (density  $\rho_0$ ). The propagation of shock front by the background gas follows the distance-time relationship

$$S_t = C_0(E_L/\rho_0)^{1/5}t^{2/5} \quad (1.24)$$

where  $C_0$  is a constant. The above expression for the shock front holds good for the expansion in high pressure ambient gas. At low pressure a classical drag model shows better agreement where the ejected pulse of ablation products regarded as an ensemble experience a viscous force proportional to its velocity through the background gas. The equation of motion is

$$a = -\beta_s v \quad (1.25)$$

$$v = v_0 \exp(-\beta_s t) \quad (1.26)$$

$$x = x_f [1 - \exp(-\beta_s t)] \quad (1.27)$$

where  $\beta_s$  is the slowing coefficient,  $v_0$  is the initial velocity and  $x_f = v_0/\beta_s$  is the stopping distance of the plume.

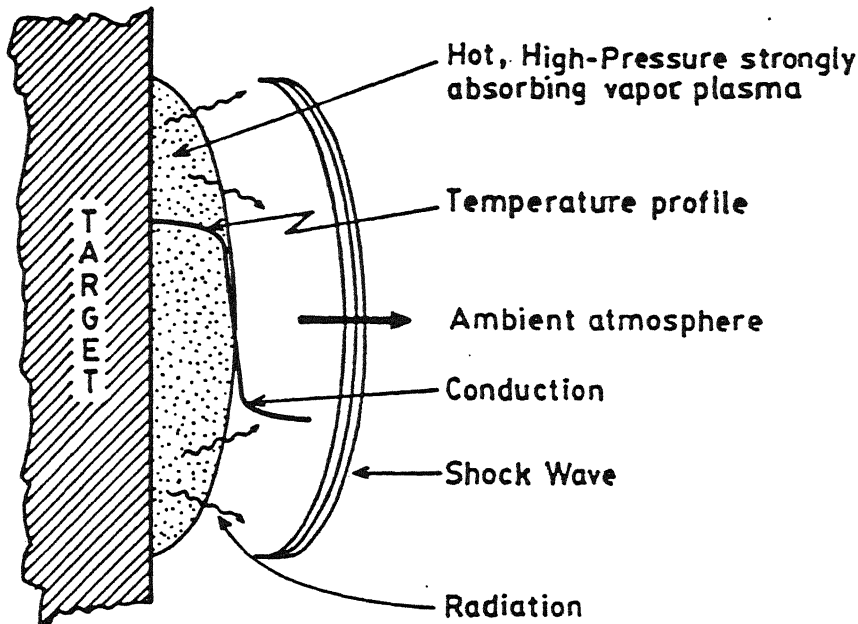


Figure 1.3: A schematic diagram showing the expansion of laser produced plasma and the formation of shock wave into the ambient gas.

### 1.3.4 Microinstabilities

Due to difference in density of the two immiscible fluids the interface develops some kind of corrugations or perturbations which if grow with time give rise to instabilities. There are three standard methods normally used to determine the stability or the properties of the instabilities associated with a given plasma equilibrium [113].

The simplest is the *intuitive approach*, in which the equilibrium is subjected to a perturbation that alters the forces acting on the plasma. If these modified forces act to increase the initial perturbation the plasma is unstable. This approach does not give quantitative information about growth rates, but it does give insight into the instability mechanism and show which equilibrium situations require further analysis, as well as providing information about which modes are likely to be unstable.

The second approach is based on *energy considerations*. An equilibrium state of a plasma is stable if potential energy is a minimum and unstable otherwise. To investigate the stability of a plasma with this method it is necessary to calculate the change

in potential energy of the plasma due to a given perturbation. The plasma equilibrium is stable if the change in potential energy is positive for *all* perturbations allowed by the plasma equations. In the presence of even one allowed perturbation for which the change in potential energy becomes negative, the plasma becomes unstable. Using this criteria it is possible to estimate the values of parameters of the plasma which take the system to unstable state. However, it is not a useful method for determining the growth rate of a particular instability.

A third approach to determine the stability of a plasma equilibrium is *normal mode analysis*. It assumes that if the equilibrium under investigation is perturbed, the linearized plasma equations for the time development of the perturbation can be solved, subject to the appropriate boundary conditions, assuming a time dependence of the form  $\exp(-i \omega_1 t)$ . This procedure gives an equation for  $\omega_1$  in terms of the equilibrium parameters. The  $\omega_1$ 's from this equation may be real, imaginary, or complex. If all the  $\omega_1$ 's are real, then the perturbation variables oscillate harmonically and the plasma is said to be in a stable state. If any or all of the  $\omega_1$ 's have positive imaginary parts, the system is unstable. However, the normal modes will grow in time. Normal-mode analysis provides complete information about the instabilities associated with a particular plasma equilibrium. The development of any initial perturbation can be followed up to the limits imposed by the linearization of the equations. Unfortunately, normal-mode analysis can be applied only in those cases where the plasma equilibrium is simple enough to allow solution of the plasma differential equations.

One common example which often occurs at the interface of two moving fluids is Rayleigh Taylor (RT) instability. RT instability occurs at the interface of the two fluids of different densities when accelerated in a perpendicular direction to their interface; this interface is unstable or stable according to whether the acceleration is directed from heavier to the lighter medium or vice-versa [114, 25]. In other words Rayleigh Taylor instability occurs when the density grows in the direction against the accelerating force. A heavy fluid supported against gravity by a light fluid is a common example of Rayleigh Taylor

instability. The details of the Rayleigh Taylor instability and the calculation of growth using the third approach is presented in Chapter 6.

## 1.4 Equilibrium in Plasmas

In complete thermodynamic equilibrium [45] (with both kinetic and radiative equilibrium at the same temperature  $T$ ) every atomic processes occurring in the plasma is balanced by an equal and opposite process. In this case the following conditions are satisfied : (a) all particles, electrons, neutral species and ions obey the Maxwell velocity distribution law; (b) the population distributions over the states of any atom or ion are given by the Boltzmann formula; (c) the number of ions in stage  $z$  relative to the number in stage  $(z-1)$  is given by the Saha equation, (d) the intensity distribution of the radiation as a function of frequency and temperature is given by the Planck's formula. All these conditions are characterized by the same temperature  $T$ . Rarely, especially in terrestrial plasmas, a perfect thermodynamic equilibrium is approached; the very fact that radiation is emitted from a plasma prevents thermodynamic equilibrium from occurring.

The commonest plasma model conforms to local thermodynamic equilibrium (LTE). In LTE it is assumed that collisional events, in particular the events involving electrons, determine the behavior of the system. The collisions are assumed to be governed by the same laws that hold in total thermodynamic equilibrium. The temperature used is the electron temperature,  $T_e$ , since electrons dominate the collision process. The radiation distribution however is not given by Planck's equation and radiative effects are assumed to play an insignificant role in determining the equilibrium in the plasma. For LTE to hold, the electron density must be sufficiently high. According to McWhirter [115], for LTE to hold  $n_e$ , the number of electrons per  $\text{cm}^3$  must satisfy;

$$n_e \geq 1.6 \times 10^{12} T_e^{1/2} \chi^3 \quad (1.28)$$

where  $\chi$  is the excitation potential (in eV) of the transition. At low electron densities a second limiting type of equilibrium called coronal equilibrium (so called because it describes



conditions in the solar corona) may be attained. In this case excitation and ionization occur as the result of electron collisions whereas de-excitation and recombination occur by the emission of radiation. The plasma is assumed to be optically thin so that re-absorption of the emitted radiation is negligible.

## 1.5 Laser Plasma in Magnetic Field

The physics of plasma flow across magnetic field lines is important in many laboratory and space plasmas. The familiar qualitative picture of a plasma moving in transverse magnetic field fall into one of the two extreme categories

(1) In case of a low pressure plasma, the magnetic field diffuses into the plasma resulting in polarization of the plasma, *i. e.* an electric field  $E$  is established which is perpendicular to both  $B$  and the plasma velocity. The plasma moves across the  $B$  field by  $\vec{E} \times \vec{B}$  drift. This case has been discussed qualitatively by Schmidt [116] and a more complete discussion has been given by Bostick [117].

(2) In case of high pressure plasma, the  $B$  field is excluded from the plasma interior. If the plasma pressure exceeds the magnetic pressure, the plasma "punches" its way across. To produce a field-free cavity of volume  $V$  in a field  $B$  requires energy  $W$  which is stored as potential energy in the plume, given by

$$W = \frac{B^2}{2\mu_0} V \quad (1.29)$$

where  $\mu_0$  is the permeability of free space and  $B$  is expressed in kG,  $V$  in  $\text{cm}^3$  and  $W$  in J,  $W = 4 \times 10^{-3} B^2 V$ . The maximum volume to which the plasma can expand is found by setting  $W$  equal to the plasma energy [118]. As the plasma expands in the field, currents are generated in the surface which result in Ohmic heating. In this way some of the expansion energy is converted into thermal energy. The interface between the plasma and the region of greater field strength is unstable against small perturbations, another form of Rayleigh-Taylor instability.

The expansion of laser produced plasma expanding in magnetic field has been dis-

cussed theoretically by several authors. The simple model of a cylindrical plasma which expands freely, parallel to its axis, along the magnetic field lines was discussed by Shkuropat and Shneerson [119] whereas that across a magnetic field was investigated by Bhadra [120] who for simplicity assumed a spherically symmetric uniform magnetic field. Bernstein and Fader [121] considered the case of a spherical, resistive, collision dominated plasma, which was assumed to retain its spherical shape as it expands in a uniform magnetic field. Haught *et. al.* [122] included a viscous term and calculated the temperature, position and velocity of the plasma boundary from a particle of LiH, 40  $\mu\text{m}$  in diameter, in a magnetic field of 10 kG. The expansion of a uniform spherical plasma into a uniform background plasma in a uniform magnetic field was discussed by Wright [123] who found an analytic solution for the magnetic field configuration that is how the magnetic field lines change during the early stages of the expansion. Hains [124] showed that departures from azimuthal symmetry can impact a rotation to an isolated plasma in a magnetic field.

Cavaliere *et. al.* [125] suggested that a conducting plasma created inside a fixed conducting cylinder compresses the field lines if it expands perpendicular to the field lines. This configuration increases the effective field and has a strong confining effect on the plasma. Martineau and Tonon [126] investigated the developments of a plasma heated by a laser pulse of 6.6 GWatt peak power in a magnetic field of 1 MG within a conducting cylinder of radius 2 cm. Oscillations were observed along the minor axis, perpendicular to the field whereas plasma expanded along the major axis, along the field. The contribution of inverse Bremsstrahlung and of induced Compton effect to the absorption of energy from the laser beam were both calculated and found to be roughly equal.

Schwirzke and Tuckfield [127] have pointed out that if a plasma expands sufficiently in a magnetic field for the collision frequency to be small, two-stream instabilities may develop which increase the resistivity of the plasma and thus reduce the rate of cooling by thermalizing some of the energy of expansion. Dunn and Lubin [128] discussed the radiation emitted from a plasma expanding in a magnetic field. In addition to normal cyclotron radiation from the volume of the plasma, whose intensity varies as  $B^2$  and as

$T_e$ , a surface contribution was calculated whose intensity varies as  $B$  and as  $T_e^{1/2}$ . Lubin suggested that the time history and the extent of the interaction of the expanding plasma could be determined from a study of the emission spectrum in the vicinity of cyclotron frequency. Behavior of plasma moving in nonuniform magnetic field showed that the plasma plume splits into two lobes which move towards the poles of the magnet [129].

In eighties and nineties extensive work had been reported on plasma instabilities in magnetic field and plasma jets. The plasma expanding in high magnetic field ( $> 3$  kG) gives rise to plasma jets. Mostivych and Stamper [130] had observed highly collimated plasma jets by laser irradiation of solid barium targets. The plasma jet was observed to narrow or "focus" in the plane perpendicular to the field, while in the plane of the field the plasma expanded along the field lines and displayed flutelike striations. The narrowing of the plasma jet was explained in terms of the configuration of the plasma polarization fields, while flute structure was identified as an electron-ion hybrid (E.I.H) velocity-shear instability. E.I.H instability was also observed by Peyser *et. al.* [131] where intense laser pulse was focussed onto the interior wall of a hollow glass cylinder to provide some degree of collimation to the emerging plasma. Fast framing camera photographs showed markedly different geometrical features for plasma expanding in magnetic fields from  $B = 0$  kG to  $B = 10$  kG. At 10 kG strong jets were observed whereas below 3 kG no jet was observed. Dimonte and Wiley [132] studied the expansion of laser ablated plasma in a magnetic field with a Faraday-rotation magnetic imaging probe and fourier-analyzed optical plasma images and observed plasma instabilities which evolve from short to long wavelengths. Nishiyama *et. al.* [133] have studied the behavior of an argon plasma jet in external electric and magnetic field experimentally and through numerical simulation using three fluid model. Ripin *et. al.* [134] has observed linear and nonlinear features of a strong plasma-magnetic field interchange Rayleigh-Taylor instability in the limit of large ion Larmor radius, which undergoes rapid linear growth culminating in face-shearing flute tips. Okada *et. al.* [135] observed flute-like instability in a cylindrical column of laser produced plasma generated in a uniform magnetic field. Kent *et. al.* [136] observed

transverse Kelvin-Helmholtz instability which occurs in a fluid with a gradient in mass flow velocity, in a rotating plasmas (Q machins). Ganguli et. al. [137-141] examined in detail the instability of a plasma characterized by a sheared flow transverse to the ambient magnetic field. Lehnert [142] discussed the boundary conditions of a magnetically confined plasma and related induced surface current which are generated by free-boundary displacement currents across an inhomogeneous externally applied magnetic field. The study is important from the point of stability criteria. Recently signature of Rayleigh-Taylor instability of a plasma expanding in concave magnetic field has been observed [143].

A few reports have been made regarding material studies in magnetic field. Dirnberger et. al. [30] observed enhanced excitation and ionization of magnesium plasma in presence of magnetic field. The results are interpreted in terms of a magnetohydrodynamic interaction. Lash et al [31] had observed enhancement in the ionization due to increased electron confinement [144] in a laser ablated aluminium plasma in a transverse magnetic field. Significant changes in optical emission spectra were observed in laser ablated carbon plasma expanding in magnetic field [70]; enhanced collisions between ablated species due to cyclotron motion are held responsible for the observed change in behavior. Surprisingly, all these experiments were done in nonuniform magnetic field but the effect of nonuniformity of magnetic field was not investigated. Recently we have observed that curvature and gradient of magnetic field greatly controls the plasma behavior [145].

## 1.6 Diagnostics

In the present work, laser produced carbon plasma expanding in different ambient conditions had been studied by emission spectroscopy, ICCD photography and Langmuir probe. Since many different diagnostics have been used to study laser ablated plasma, a summary of the diagnostics utilized and the parameter that each measures are presented in Table 1.1.

Table 1.1: Various diagnostics and the corresponding plasma parameters.

Diagnostics	Plasma parameters
Emission Spectroscopy [94-97, 146-153]	Electron temperature Electron density
Ion Probe Diagnostics [101, 102, 154-159]	Electron temperature Electron density
Photography & Imaging [71, 103-105, 175]	Velocity of the plasma plume. Electron temperature Electron density
Laser Induced Fluorescence [99-100, 170-174]	Electron temperature
Time of Flight Mass Spectroscopy [160-163]	Velocity of the species, states of ionizations
Absorption Spectroscopy [164-169]	Electron density , temperature
Interferometry [130, 177]	Electron density
Laser beam Deflection Method [179]	Density gradient

## 1.7 The Present Work

In the present work the dynamics of laser ablated carbon plasma expanding in vacuum, low pressure ambient atmosphere and nonuniform magnetic field has been reported. The diagnostics used to reveal the behavior of laser produced carbon plasma in different ambient conditions are emission spectroscopy - the time integrated and time resolved, ICCD photography and Langmuir probe.

Chapter 2 deals with the details of the experimental techniques and instruments used in the experiments.

Chapter 3 deals with computer simulation studies of laser produced carbon plasma expanding in high pressure ambient gases. One dimensional Lagrangian Code Medusa which simulates the temporal and spatial evolution of laser ablated plasma in vacuum is modified for the plasma expansion in high pressure ambient atmosphere [58]. The temporal evolution of simulated plasma front for the case of plasma expanding in He, Ne, Ar and Xe gas at 300 Torr matches well with the experiment. The modified code can also simulate the plasma parameters viz. pressure, temperature, density of the plasma expanding in any gas at any higher pressure.

The behavior of laser produced carbon plasma expanding in vacuum and low pressure ambient atmosphere [105] (5 mTorr and 100 mTorr) is presented in Chapter 4. The temporal profile of CI transition  $2p^3\ ^3D^0 - 8f\ F(5/2)$  at 399.7 nm, CII transition  $3d\ ^2D - 4f\ ^2F^0$  at 426.7 nm, CIII transition  $3s\ ^3S - 3p\ ^3P^0$  at 465.0 nm and CIV transition  $3s\ ^2S - 3p\ ^2P^0$  at 580.1 nm were recorded. The transitions show a single peak structure in vacuum. In low pressure ambient atmosphere they show a double peak structure except that in CIV. The nature of double peak structure is different for different species and changes from 5 mTorr to 100 mTorr ambient pressure. The ICCD images of plasma plume show stratification of the plasma plume at 5 mTorr. Based on the above observations the formation of double peak structure and stratification of the plasma plume is explained.

Chapter 5 describes the behavior of laser produced carbon plasma in nonuniform

magnetic field in vacuum. The ICCD photographs of the plasma expanding in a nonuniform magnetic field show oscillatory behavior of the plasma front at early time as predicted theoretically [178]. At a later time ( $\sim 1000$  ns) the plume is observed to split into two lobes which move toward the poles of the magnet. The ICCD images of the plasma plume are used to calculate the plasma parameters viz. electron density and temperature as a function of time for plasma expanding in vacuum, ambient gas and magnetic field. Oscillations are observed in plasma parameters. Multiple peaks are observed in the temporal profile of CI, CII, CIII and CIV transitions because of formation of two asymmetric lobes [129]. Each lobe has three components viz. fast, intermediate and slow. The time integrated spectra of carbon plasma is taken keeping the target at different positions in magnetic field. It is observed that the curvature and gradient of magnetic field greatly affect the behavior of emission spectra [145]. The emission lines of ionic species as well as neutrals are excited and molecular  $C_2$  Swan band emission is observed when the plasma moves in convex part of magnetic field with positive field gradient. The observed change in emission characteristic is attributed to the compression of the field lines due to moving plasma and recombination of electrons due to curvature gradient drift.

The expansion of laser produced carbon plasma in nonuniform magnetic field in presence of ambient atmosphere is presented in Chapter 6. A delayed second peak is observed which is not present in case of plasma expansion in only air or only magnetic field [143]. By keeping the target positions at different regions of magnetic field it is observed that delayed second peak occurs only in that region of magnetic field where field lines are concave to the moving plasma. The possibility of Rayleigh Taylor instability along with diffusion of external air as the cause of delayed second peak is discussed.

Chapter 7 summarizes the results of present work.

## Chapter 2

# Experimental Techniques

---

An overview of various experimental techniques used to study laser ablated plasma is described in Chapter 1. Various experimental techniques used to study the dynamics of laser ablated plasma expanding in vacuum, low pressure ambient gas and nonuniform magnetic field are described in detail in the present section.

Nd:YAG (Spectra Physics, Model DCR-4G) laser along with its harmonics was used for laser ablation. It delivers energy upto 1 mJ/pulse with full width at half maxima (FWHM) of 8 ns at fundamental with a repetition rate 10 pulses per second. The laser beam has a Gaussian limited mode structure, with beam divergence less than 0.5 mrad and spot diameter of 8 mm. The energy of the laser was monitored using a laser power meter (Ophir Model 30A) by placing the meter in the path of the main beam. Laser energy was varied by changing the voltage on the laser oscillator and amplifier. Burn patterns taken at different energies show no significant variation in the mode pattern.

The interaction chamber and the experimental configuration used for ablation studies is shown in Fig.2.1. The laser beam was focused onto the spectroscopic grade pure graphite target rod attached to the target holder in the chamber. When laser ablation studies were done in presence of magnetic field, the target was kept in the magnetic field as shown in the inset of Fig.2.1. The target rod was continuously rotated and translated with the



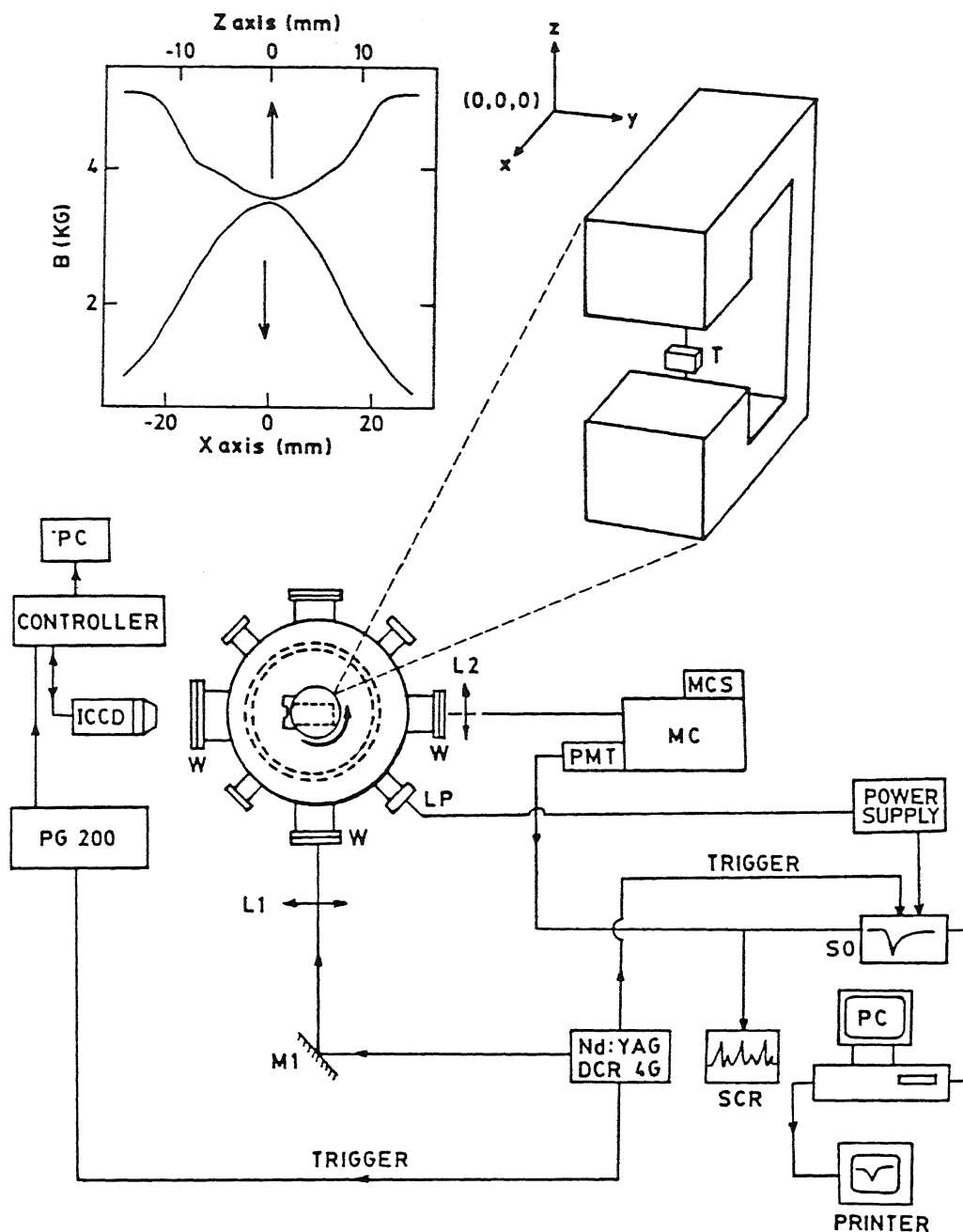


Figure 2.1: Schematic of the experimental set up used in the experiment. Position of the magnet and target is shown separately. T: Target, MC: Monochromator, SO: Storage Oscilloscope SCR: Strip Chart Recorder, PG200: Pulse Generator, L1/L2: Convex Lens, ICCD: Intensified Charged Coupled Device. LP : Langmuir Probe. The magnetic field along Z and X axis is shown in the inset.

help of an external stepper motor so as to allow each laser pulse to interact with the fresh target surface. The interaction chamber is made up of mild steel with eight output ports. One of the output ports is used for laser entrance and the two perpendicular ports were used for recording the optical emission from the ablated plume. The interaction chamber was evacuated to a pressure better than  $10^{-3}$  Torr using a rotary / diffusion pump. The ambient gas was fed into the chamber through a needle valve connected to the interaction chamber. Experiments were carried out in presence of air at various pressures ranging from  $10^{-3}$  -  $10^{-1}$  Torr.

## 2.1 Optical Emission Diagnostics

A high temperature and high density plasma was created by focussing the laser beam using a 50 cm lens on to the pure graphite target. The plasma radiation emitted from the target was imaged onto the entrance slit of a monochromator (Jobin Yvon, HRS-2) with a lens, so as to have one to one correspondence with the plasma and its image onto the slit of the monochromator. The monochromator was continuously tuned using a microprocessor controlled scan system [180]. The output from the monochromator was detected with a photomultiplier tube (Hamamatsu, IP28) and recorded on a strip chart recorder or displayed on the screen of the storage oscilloscope (Iwatsu, TS-8123) interfaced with PC. The recorded optical emission data are used to evaluate the electron temperature using the emission lines intensity ratio, electron density using Stark broadened profile of a transition and the vibrational temperature using the intensity of Swan band heads. Investigation of the optical emission of the plasma plume also gives information about the optical and temporal evolution of the species produced such as excited atoms, ions and molecules during laser target interaction.

### 2.1.1 Electron Temperature

Various methods of calculating electron temperature using spectroscopic observations are described in the literature [181, 182]. We have used the relative intensities of the spectral

lines from a given ionization state for estimating electron temperature. Assuming plasma in local thermodynamic equilibrium (LTE), the electron temperature can be estimated using, [181, 183]

$$k_B T_e = \left[ \frac{E' - E''}{\ln \left( \frac{I'' \lambda'' g' A'}{I' \lambda' g'' A''} \right)} \right] \quad (2.1)$$

where  $E''$  and  $E'$  are the excitation energies of the lower and upper levels, respectively.  $I''$  and  $I'$  are the intensities,  $g''$  and  $g'$  are the statistical weights, and  $A''$  and  $A'$  are the transition probabilities and  $\lambda''$  and  $\lambda'$  are the wavelengths of various transitions.  $k_B$  and  $T_e$  represent the Boltzmann constant and electron temperature, respectively. The slope of the curve  $(E' - E'')$  against  $\left[ \ln \left( \frac{I'' \lambda'' g' A'}{I' \lambda' g'' A''} \right) \right]$  gives electron temperature, the parameters used for estimating electron temperature are available in the literature [184]. The measured electron temperature using intensity of CIII species in our work lies between 4-7 eV.

### 2.1.2 Electron Density

The Stark broadened profile of a transition for which the Stark-broadening parameters are available in the literature, can provide electron densities of the plasma [39, 185, 186]. Stark-broadening arises due to the coulomb interaction of the emitted species with both the electrons and ions expanding in the plume. The line profiles were recorded keeping the monochromator resolution to maximum [40]. Observed lines with true half width being given by, [182, 36]

$$\Delta\lambda_{true} = \Delta\lambda_{observed} - \Delta\lambda_{instrument} \quad (2.2)$$

where  $\Delta\lambda$  of a line (FWHM) is given by

$$\Delta\lambda = 2W_e \left( \frac{n_e}{10^{16}} \right) + 3.5A_i \left( \frac{n_e}{10^{16}} \right)^{\frac{1}{4}} \times (1 - 1.2N_D^{-\frac{1}{3}}) W_e \left( \frac{n_e}{10^{16}} \right) \quad (\text{\AA}) \quad (2.3)$$

First term in the Eqn.(2.3) gives contribution from electron broadening and second term is the ion broadening correction;  $W_e$  is the electron impact parameter which can be interpolated at different temperatures and  $A_i$  is the ion broadening parameter, both  $W_e$  and  $A_i$

are weak functions of temperature,  $n_e$  is the electron density and  $N_D$  is number of particles in Debye sphere given by

$$N_D = 1.72 \times 10^9 \frac{[T(\text{eV})]^{\frac{3}{2}}}{[n_e(\text{cm}^{-3})]^{\frac{1}{2}}} \quad (\text{cm}^{-3}) \quad (2.4)$$

Eqn.(2.3) is valid only if  $N_D \geq 1$  and  $0.05 < A_i(n_e/10^{16})^{\frac{1}{4}} < 0.5$ . Using our measured temperature of 5.49 eV and density  $\sim 10^{17} / \text{cm}^3$  (at 4 mm), we get the number of electrons in the Debye sphere equal to 70 and the parameter  $A_i(n_e/10^{16})^{\frac{1}{4}}$  equal to 0.06. Thus the use of Eqn.(2.3) for density measurement is justified. The ionic contribution to the broadening is observed to be much smaller and can be neglected in a typical laser ablated plasma [36, 187], Eqn.(2.3) simplifies to

$$\Delta\lambda = 2W_e \left( \frac{n_e}{10^{16}} \right) \quad (\text{\AA}) \quad (2.5)$$

We have used Eqn.(2.5) for estimating electron density of C II transition ( $3P^2P^0 - 4s^2S$ ) at 392.0 nm. Electron density using 1.06  $\mu\text{m}$  laser wavelength and irradiance of  $1.22 \times 10^{11}$  Watt/ $\text{cm}^2$  is found to be  $10^{16}$ - $10^{17} \text{ cm}^{-3}$ .

### 2.1.3 Plasma Expansion Velocity

To calculate the expansion velocity of the plasma species, the temporal profiles of various transitions of interest were recorded at different distances from the target surface. The velocity of the plasma species is calculated from the delay of the peak of the signal at different distances with respect to the trigger pulse [39]. The velocity of CIII species at distance of 4 mm from the target surface in vacuum is estimated to be  $1.76 \times 10^6 \text{ cm/sec}$ .

### 2.1.4 Vibrational Temperature

The vibrational temperature was estimated using  $C_2$  Swan band head intensities [188]. the relative population in each vibrational level  $N_{u'}$  can be obtained using a theoretical Franck-Condon factor [189]  $F_{u'u''}$  and the band head intensity  $I_{em}^{u'u''}$  observed at frequency  $\nu$ ,

$$N_{u'} = \frac{CI_{em}^{u'u''}}{D_u F_{u'u''} \nu^4} \quad (2.6)$$

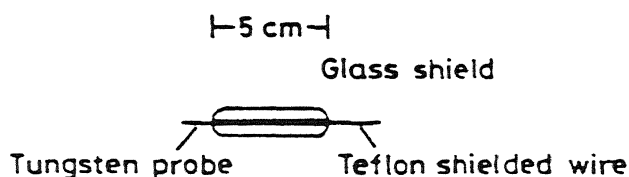


Figure 2.2: A schematic sketch of the probe.

where  $C$  is a constant and  $D_u$  represents the correction factor for the detecting system.  $u'$  and  $u''$  are the vibrational levels of the upper and lower electronic states respectively. Since in thermal equilibrium the population  $N_{u'}$  of the initial state is proportional to  $\exp [-G(u') h c / k_B T_{vib}]$ , we have

$$\frac{N_{u'}}{N_{w'}} = \frac{I^{u'u''}}{I^{w'w''}} = (Constant) \exp \left[ \frac{-[G(u') - G(w')]}{k_B T_{mb}} \right] \quad (2.7)$$

where  $G(u')$  and  $G(w')$  is term value of the upper vibrational level  $u'$  and  $w'$ ,  $T_{mb}$  is the molecular vibrational temperature. Plotting the log of the ratio of band head intensities of two transitions against the difference of term value of the upper vibrational level, gives vibrational temperature. The vibrational temperature for the  $C_2$  molecule is estimated to be 1.96 eV.

## 2.2 Ion Probe Diagnostics

The ion probes are simple and extremely useful for in-situ diagnostics of the flowing plasmas. Ion probes provide the local information on plasma conditions unlike emission or absorption spectroscopy, laser-induced fluorescence or imaging techniques which are useful along the line of sight [100]. The schematic of the experimental arrangement for the ion probe diagnostics is shown in Fig.2.1, where the port which is at an angle of  $45^\circ$  of the interaction chamber with respect to laser entrance port was used for ion-probe diagnostics. Langmuir probe consisted of a tungsten wire of 0.6 mm diameter and a power supply. Figure 2.2 shows a schematic sketch of the probe. The probe to target distance could be varied continuously. The ion probe was connected through a teflon shielded wire to the power

supply outside the vacuum chamber. The power supply consisted of a variable -180 V to +180 V DC supply. Output signal due to the electron / ion current from the probe was fed to a storage oscilloscope through a 50  $\Omega$  terminator. The digitized ion probe signals were fed to the PC for further data processing. The peak of the ion probe signal ( $I_p$ ) was plotted against the probe voltage ( $V_p$ ) to get the  $I_p$ - $V_p$  characteristics. The electron temperature and ion density were calculated using the  $I_p$ - $V_p$  characteristics of the ion probe.

### 2.2.1 Electron Temperature

The evaluation of plasma parameter from the ion probe characteristics depends on the shape of the probe, probe dimension and collision length etc. Assuming Maxwellian velocity distribution of the charge carriers, the total probe current ( $I_p$ ) flowing through the probe is given by [190].

$$I_p = I_{+0} + I_{e0} \exp \left( \frac{eV_p}{k_B T_e} \right) \quad (2.8)$$

Where  $I_{+0}$ ,  $I_{e0}$ ,  $V_p$ ,  $e$ ,  $T_e$ , represent the ion saturation current, electron saturation current, applied probe voltage, charge on the electron and electron temperature respectively. Below electron saturation current, Eqn.2.8 can be used to estimate  $T_e$  by using the formula,

$$T_e = \left[ \frac{\partial \ln(I_p - I_{+0})}{\partial V_p} \right]^{-1} \quad (2.9)$$

### 2.2.2 Ion Density

The knowledge of the variation of the ion current with applied probe voltage offers the possibility to estimate the plasma ion density. Several ways of estimating ion density using ion probe characteristics are available in the literature [190]. The derivative of the square of the probe current with respect to the probe potential yields a straight line for the cylindrical probes, the slope of the straight line gives the density,

$$N_i = \left[ \frac{4\pi m_e (-dI_p^2/dV_p)}{3A_p^2 e^3} \right]^{\frac{1}{2}} \quad (2.10)$$

where  $N_i$  represents the ion density,  $A_p$  is the area of the ion probe,  $e$  and  $m_e$  are the charge and mass of the electron respectively.

## 2.3 Fast Photography

Fast side on views of the expanding plasma plume were made by recording the overall visible emission from the plasma plume with a gated intensified CCD camera system (ICCD I76G/2, Princeton Instruments Inc.). The complete system comprises an ICCD detector, ST-130 controller, PG 200 pulse generator. The controller is interfaced directly to a Personal Computer.

**ICCD detector :** A 50 mm Nikon telephoto lens attached at the detector front is used to image the region of plasma. The imaging field of view and the different ports of ICCD detector are shown in Fig.2.3 (a) and (b) respectively. The detector has the following distinct sections. The front enclosure contains the image intensifier and the CCD. The CCD is seated on a cold finger that is in turn seated on a thermoelectric (Peltier effect) cooler, driven by closed loop proportional control circuitry. The back enclosure contains the heat removal block where coolant is circulated. A thermal sensing diode attached to the cooling block of the detector monitors its temperature. Heat generated at the exhaust plate of the cooler is conducted to the enclosure of the detector where it is carried away by water or other coolant. ICCD is never run without water or circulating coolant. Continuous flushing of the detector with nitrogen or dry air is required for ICCD while they are cooled. Two copper and brass fittings are used to connect the coolant ports on the sides of the detector. Either port may be used as the inlet point. Detector is not operated if the relative humidity in the lab is greater than 40%.

The detector consists of a CCD device optically interfaced to the microchannel plate image intensifier through an optical-fiber coupler. This fiber optic coupling is very sensitive. With a fiber coupled detector the combined high gain of the image intensifier and the low read out of the CCD array results in a detector capable of responding to a single photoelectron. The microchannel plate (MCP) intensifier prevents photoelectrons from reaching the phosphor / CCD array until a gate voltage is applied. In the shutter mode for the ICCD, the photo cathode potential is held approximately 200 volts more positive

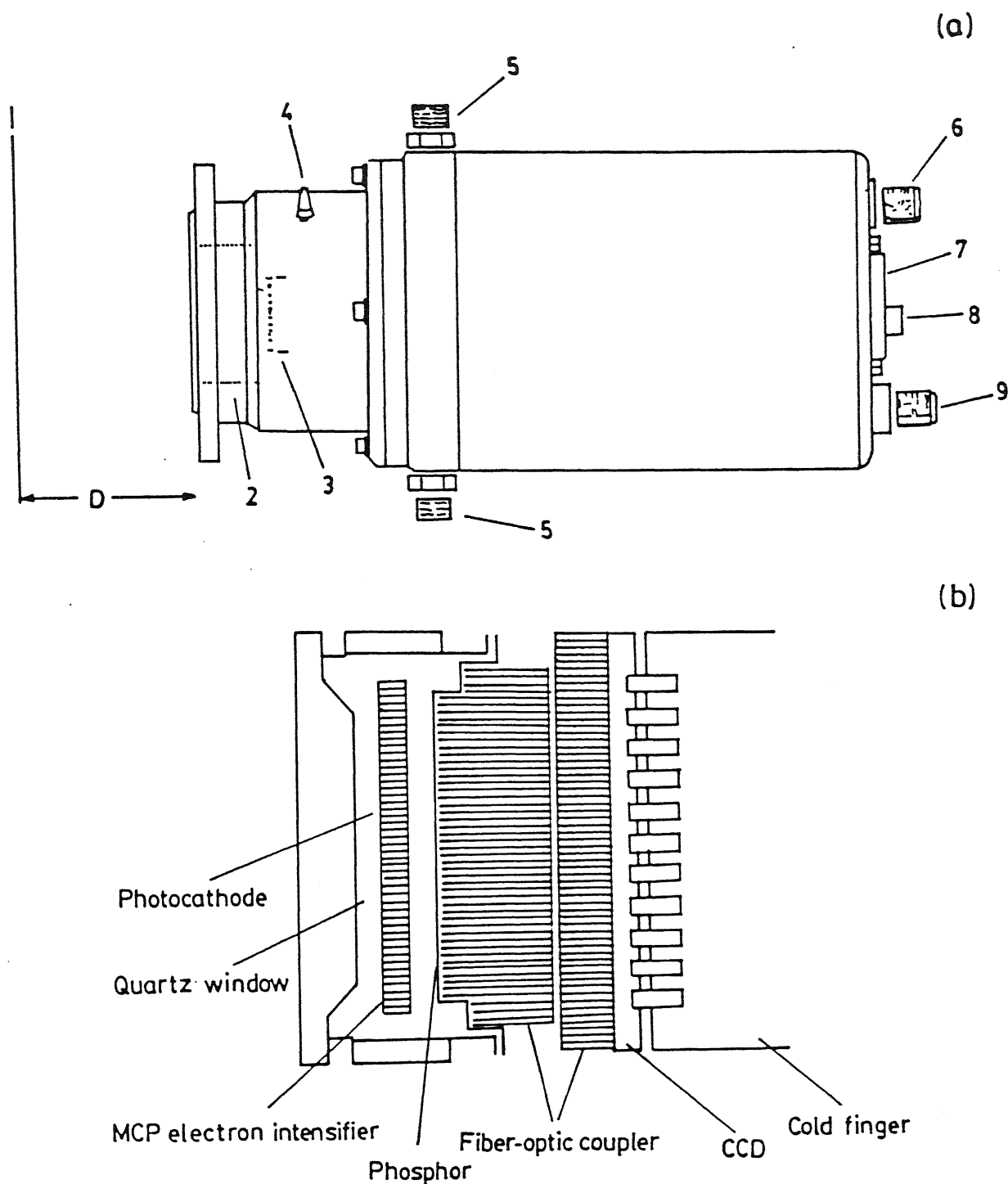


Figure 2.3: (a) A schematic sketch of the ICCD detector and imaging field of view; 1. Object, 2. Image Intensifier, 3. CCD, 4. Nitrogen input port, 5. Coolant ports, 6. Gate shutter switch, 7. DB 25 connector for cable to controller, 8. BNC connector for HV signals from pulser, 9. Potentiometer for setting intensifier gain and (b) Different ports of ICCD.



and therefore the photoelectron image can not reach the MCP. At an exact predetermined time (with respect to triggering onset) the pulse generator produces a negative pulse of approximately 200 volts amplitude. This pulse when applied to the photocathode renders it (for the duration of pulse) more negative than MCP and therefore the "photo electron image" is transmitted to the MCP and intensified. MCP is composed of more than  $10^6$  individual miniature electron multipliers with an excellent input to output spatial geometric accuracy. Intensified gain is varied by adjusting the voltage across the MCP or the voltage across the MCP output and the phosphor. The second parameter is factory adjusted as it affects both the gain and the resolution of the intensifier.

To get an image from the CCD detector to appear on the computer screen, it must first be read, digitized and transferred to the computer. A block diagram of the path of the image signal is shown in Fig.2.4. CCD is viewed as a two dimensional grid of individual photo diodes (pixels, 576 X 384) each connected to its own storage bucket (called wall). Each pixel senses the intensity of light falling on its collection area and stores corresponding amount of charge in its associative bucket. These buckets are shifted to the bucket of shift register and then to measurement circuitry. ICCD's can get destroyed if exposed to excessive light levels, higher than twice the ADC saturation levels, so care is taken not to expose it to room light.

**PG-200 programmable gate pulse generator :** The PG-200 programmable gate pulse generator combines the functions of a high voltage gate pulse generator and a sophisticated timing source / delay generator. It is primarily intended to provide high speeding gating of proximity-focused MCP image intensifier. It is interfaced to the ICCD series detector equipped with internal 1 M $\Omega$  terminator. This instrument operates at high voltages.

**ST-130 controller :** The interfacing of the ICCD detector and computer is through the controller. It controls all the timing operations. During read out, an analog signal representing the charge of each pixel is sent to the controller and digitized as shown in Fig.2.4. The number of bits per pixel is based on both the hardware settings and the

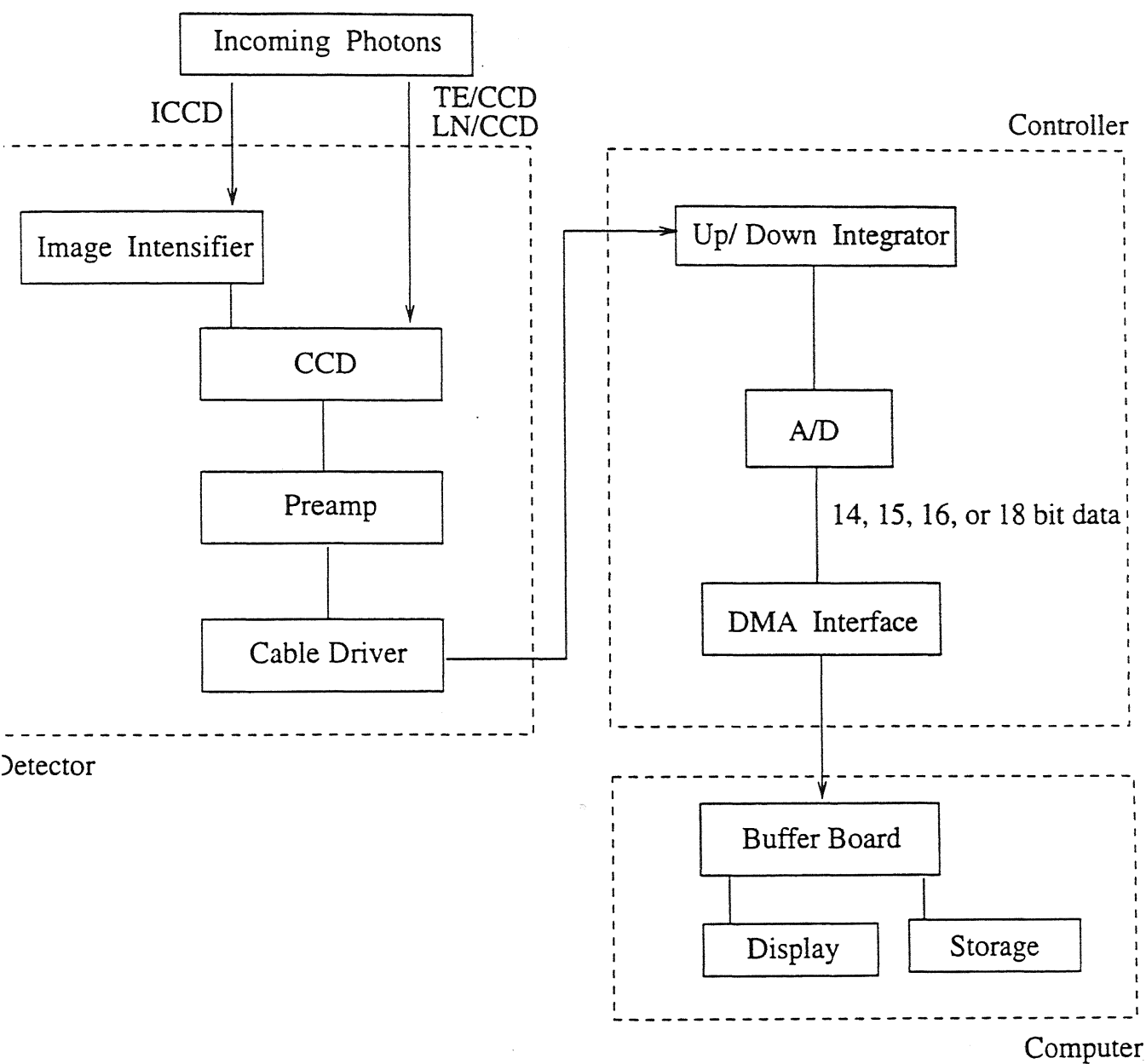


Figure 2.4: A block diagram of the light path in the detector system.

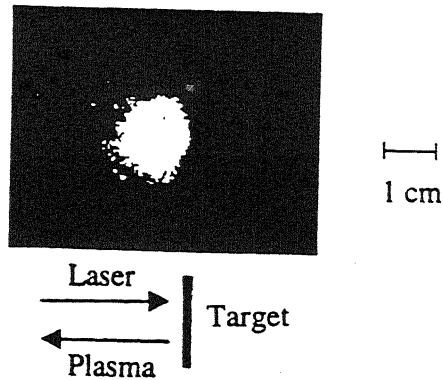


Figure 2.5: Typical ICCD image of the plasma plume at 200 nsec delay from the ablating pulse.

settings programmed into the controller. Recorded images are analyzed using the supplied software.

Plume expansion was recorded utilizing the overall visible emission from the plasma plume with a gated, intensified CCD camera system. Light was collected from throughout the plasma volume to form a weighted two dimensional image of the plume intensity. As explained above, MCP prevents photoelectrons from the photo emissive detector surface from reaching CCD array until a gate voltage pulse is applied. Fast gate pulses (acting as the shutter for the camera) were supplied at variable times after the firing of the laser for "Stop action" images of the plume expansion. Gate width was fixed at 20 ns implying that the electrons from the detector can reach the CCD array for 20 ns. Delay time is the time after the firing of laser pulse at which the gate voltage is applied. An important experimental parameter is the exposure time chosen for the ICCD images i.e. the time for which the CCD is exposed to the emitted radiation. Over exposure results in loss of details in bright regions of interest while under exposure misses the fainter regions.

Measurement of the front edge of the laser plume as a function of time helps one estimate the initial velocity and the stopping distances of the plume [104]. The software provided with the camera was tailored to calculate maximum, minimum, total and mean intensity of the plasma plume. The colour code helps observe different intensity regions of the plume. Figure 2.5 gives a typical ICCD image of carbon plasma after 200 nsec from the time of ablating pulse.

## Chapter 3

# Numerical Modeling of Laser Matter Interaction in Presence of an Ambient Gas

---

### 3.1 Introduction

The study of laser-matter interaction has been a subject of paramount importance in recent years. There have been reports on laser-matter interaction in the presence of an ambient gas [60, 92], electric field [191, 192] and magnetic field [193]. Various analytical models for the plasma expansion in ambient gas have been developed [44] but they fail to predict details about the plasma behavior because they do not take care of the many important processes (for example Bremsstrahlung radiation, heat transport due to suprathermal electrons etc.) and hence a detailed theoretical description is necessary. The genesis of this study is to understand the interaction of a high power pulsed laser beam with a solid target in presence of an ambient gas and to develop a comprehensive numerical model for the

---

<sup>0</sup>The work presented in this Chapter is based on :

1. "Numerical modeling of laser matter interaction in the presence of an ambient gas." A. Neogi and R. K. Thareja, *Pramana* 50, 63 (1998).

process. Computer simulation studies help optimise the plasma parameters essential for various technological applications and studying astrophysical processes without actually doing the experiment.

The present Chapter deals with the case of intermediate intensity regime.  $10^8$ - $10^{12}$  Watt/cm<sup>2</sup> of laser power and high ambient gas pressure. We have used a modified version of the laser fusion code MEDUSA [51], MED101. This is an one dimensional Lagrangian code which calculates hydrodynamic and thermodynamic parameters of the laser produced plasma in vacuum. MED101 is a well developed code which can take care of the double and triple layered targets and can calculate X-ray laser gain. We have made modifications [58] in this code to implement it for ambient gas. The Rankine-Hugoniot relations for shock waves are used to calculate the changing boundary conditions that is temperature and pressure. The Navier Stokes equation is changed due to Reynolds stress arising due to turbulent boundary layer mixing and at later stage due to diffusion and interparticle collisions. The thermodynamics of the system is also changed accordingly. The equations are solved using finite difference method.

The modified code MED101 is used to simulate the experimental results where the laser produced carbon plasma expanded into a background of He, Ne, Ar and Xe gas.

## 3.2 Numerical Model

### 3.2.1 In Vacuum

A brief outline of the one dimensional Lagrangian code MEDUSA is presented below. A detailed description and the mathematics of the original code is given by Christiansen et al [51]. The plasma is assumed to consist of a charge neutral mixture of electrons and various species of ions. MEDUSA treats the thermodynamical properties of the electrons as one subsystem with internal energy  $U_e$  per unit total mass, temperature  $T_e$ , pressure  $P_e$  and specific heat ratio  $\gamma_e$  and the ions as second subsystem with a corresponding set of variables. Electric and magnetic fields are neglected and the two subsystems are coupled together by a common velocity and by energy exchange due to collisions between them.

This is the one fluid two temperature model, the whole of the plasma is considered as one fluid in which electrons and ions have different temperatures. The internal energy per unit mass is denoted by  $U$  (subscript  $e$  and  $i$  are omitted),

$$U = \frac{PV}{(\gamma - 1)} \quad (3.1)$$

where  $P$  is pressure,  $V$ , the volume per unit mass and  $\gamma$  the specific heat ratio. The two subsystems have independent equations of state

$$U = U(\rho, T), \quad P = P(\rho, T) \quad (3.2)$$

where  $\rho$  is the density of the plasma.

According to the first law of thermodynamics,

$$\frac{dQ}{dt} = \frac{dU}{dt} + \frac{dW}{dt} \quad (3.3)$$

where  $Q$ ,  $U$  and  $W$  represent heat, internal energy and work done.

$$S = \frac{dQ}{dt} = C_v \frac{dT}{dt} + \beta_T \frac{d\rho}{dt} + P \frac{dV}{dt} \quad (3.4)$$

$$C_v = \left( \frac{\delta U}{\delta T} \right)_\rho, \quad \beta_T = \left( \frac{\delta U}{\delta \rho} \right)_T \quad (3.5)$$

The source terms  $S_i$  and  $S_e$  for ions and electrons respectively are written as;

$$S_i = H_i - R + Q_s \quad (3.6)$$

$$S_e = H_e + R + L + X \quad (3.7)$$

where  $H$  represents the flow of heat due to thermal conduction,  $R$  is the rate of energy exchange between ions and electrons,  $L$  the rate of Bremstrahlung emission,  $X$  the rate of absorption of laser light and  $Q_s$  is the rate of viscous shock heating. In plasma, if shock wave is formed, thermal conduction or energy transport is due to electrons whereas

viscosity or momentum transport is due to the ions. The ions are heated up due to viscous pressure of the shock wave which is represented by  $Q_s$ , the viscous shock heating. Mathematical expression of each term appearing in Eqn.(3.6) and (3.7) are given below (in SI unit)

(1). The flow of heat due to thermal conduction (  $H$  ) in Eqn.(3.6) and (3.7) is given by

$$H = \frac{1}{\rho} \nabla \cdot \kappa \nabla T \quad (3.8)$$

where  $\kappa$  is thermal conductivity. Expressions for thermal conductivity due to ions ( $\kappa_i$ ) and electrons ( $\kappa_e$ ) are given by [193]

$$\kappa_i = 4.3 \times 10^{-12} T_i^{\frac{5}{2}} (\log \Lambda)^{-1} \bar{M}^{-\frac{1}{2}} \bar{z}^{-2} (\bar{z}^2)^{-1} \quad (3.9)$$

$$\kappa_e = 1.83 \times 10^{-10} T_e^{\frac{5}{2}} (\log \Lambda)^{-1} \bar{z} (\bar{z}^2)^{-1} \quad (3.10)$$

where  $T_i$  and  $T_e$  are the ion and electron temperature,  $\log \Lambda$  is the Coulomb logarithm given by Eqn.(3.11),  $\bar{M}$  and  $\bar{z}$  are the average mass and charge number given by Eqn.(3.12) and (3.13) respectively

$$\Lambda = 1.24 \times 10^6 T_e^{\frac{3}{2}} \frac{n_e^{-\frac{1}{2}}}{z} \quad (3.11)$$

$$\bar{M} = \sum_k f_k M_k \quad (3.12)$$

$$\bar{z} = \sum_k f_k z_k \quad (3.13)$$

where  $M_k$ ,  $z_k$  are the mass and charge number of the individual species.

(2). The exchange of energy between ions and electrons (  $R$  ) in Eqn.(3.6) and (3.7) depends on the difference of temperature between them and is given by

$$R = \frac{1}{\rho} \omega_{ex} n_e k_B (T_i - T_e) \quad (3.14)$$

where  $\omega_{ex}$  is energy exchange rate given by [194]

$$\omega_{ex} = \frac{M^{-1} z^2 e^4 n_i \log \Lambda m_e^{\frac{1}{2}}}{32 \sqrt{2} \pi \epsilon_0^2 m_H} (k_B T_e)^{-\frac{3}{2}} \quad (3.15)$$

where  $m_e$  and  $m_H$  represent electron mass and proton mass respectively. Substituting for  $\omega_{ex}$  in Eqn.(3.14) we get

$$R = 0.59 \times 10^{-8} n_e (T_i - T_e) T_e^{-\frac{3}{2}} \bar{M}^{-1} z^2 \log \Lambda \quad (3.16)$$

(3). The plasma loses heat mainly through Bremsstrahlung radiation. This occurs when electrons come close to the nucleus, get accelerated and emit photon. The Bremsstrahlung radiation emitted by the electrons is represented by  $L$  in Eqn.(3.7). The radiation is assumed to escape from the plasma and is thus an energy loss ( $L < 0$ ) term. For a Maxwellian gas  $L$  is [194],

$$L = - \frac{z^2 e^6 n_e \bar{v}_e}{24 \pi \epsilon_0^3 c^3 m_e m_H \bar{M} h} \quad (3.17)$$

Inserting for  $v_e$ , the electron velocity, Eqn.(3.17) becomes

$$L = -8.5 \times 10^{-14} n_e T_e^{\frac{1}{2}} \bar{z}^2 \bar{M}^{-1} \quad (3.18)$$

(4). Absorption is assumed to occur via inverse Bremsstrahlung at densities below the critical density. If  $P_L(R_0)$  is the laser power incident on the plasma boundary at  $r = R_0$  then at any point  $r$  inside the plasma from the boundary we have

$$P_L(r, t) = \exp[-\alpha(R_0 - r)] P_L(R_0, t) \quad (3.19)$$

Here  $\alpha$  is the absorption coefficient defined earlier [Eqn.(1.2)]. The term  $X(r, t)$  in Eqn.(3.7) is defined as laser power absorbed per unit mass,

$$X(r, t) = \frac{P_L(r, t)}{d\bar{M}} \quad (3.20)$$

where  $d\bar{M}$  is an infinitesimal mass element.

(5). The ions are heated up due to viscous heating caused by the shock wave, the viscous heat term is given by [19]

$$Q_s = q \frac{\partial V}{\partial t} \quad (3.21)$$



where  $q$  is a viscous pressure given by

$$q = b^2 \rho \left( \frac{\partial v}{\partial x} \right)^2, \quad \frac{\partial V}{\partial t} < 0 (\text{Compression}) \quad (3.22)$$

$$q = 0, \quad \frac{\partial V}{\partial t} > 0 (\text{Expansion}) \quad (3.23)$$

where  $b$  is a coefficient of viscosity usually chosen as  $b = 2^{1/2}$ .

(6). The plasma is considered to be a fluid, the motion of the plasma is governed by the Navier-Stokes equation,

$$\rho \frac{dv}{dt} = -\nabla P \quad (3.24)$$

where  $P$  is the total pressure and  $v$  is the velocity given by

$$v(r, t) = \frac{dr}{dt} \quad (3.25)$$

(7) It is necessary to specify both hydrodynamic and thermodynamic boundary conditions at the inner and outer boundaries. For the inner boundary we choose

$$v(r = 0) = 0.$$

At a moving outer boundary point  $r=R_0$  we distinguish the following four cases.

1. If pressure at the external boundary is zero and no thermal flux, usually referred to as zero thermal flux case,

$$P(R_0) = 0$$

2. The velocity of the external boundary is zero, ion and electron temperature of external boundary is changing as some function of time,

$$v(R_0) = 0, T_i(R_0) = T_i(t), T_e(R_0) = T_e(t).$$

3. The pressure applied at the outer most boundary is some function of time and no thermal flux (zero thermal flux),

$$P(R_0) = P(t)$$

4. The velocity of the external boundary is changing as some function of time and no thermal flux (zero thermal flux).

$$v(R_0) = v(t)$$

Case 1 is used for general problems involving the absorption of laser light, case 2 is used to study simplified thermal conductive problems, and cases 3 and 4 are used to study simplified hydrodynamics problems e. g. compression and expansion of a plasma.

These equations are solved using finite difference method. The whole length of the plasma is divided into finite number of meshes and time is divided into large number of small time steps. The plasma parameters like position of the plasma front, velocity, temperature, pressure and density etc. are calculated as a function of time and space. The original code which calculates the plasma parameters in vacuum is modified for the case of plasma expansion in high pressure ambient gas and is described in detail in the next section.

### 3.2.2 In Ambient Gas

The plasma expanding in ambient gas can broadly be divided into two regions in accordance with external gas pressure. (1) If the external gas pressure is low such that the mean free path of the plasma particles exceeds or is comparable with the dimension of experimental chamber ( $\sim 10$  cm). In this case shock wave does not form and there is a strong interpenetration of laser plasma and the ambient gas [60]. The calculated shock thickness is less than the mean free path of the plasma particles [98]. (2) The external pressure is high (say  $> 1$  Torr) and the mean free path is much less than the dimension of the experimental chamber. In this case shock wave forms in the ambient gas, the calculated shock thickness is considerably greater than the mean free path of the plasma particles. The present Chapter deals with the physics of plasma expansion in high pressure external gas and the formation of shock wave.

When the velocity of fluid in motion (or any disturbance) either becomes comparable with or exceeds that of sound (supersonic fluid) it gives rise to shock wave in the ambient

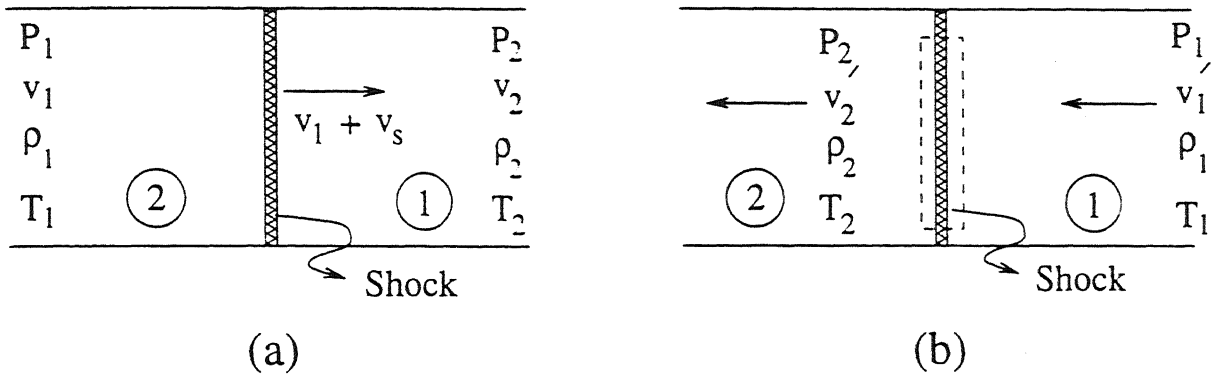


Figure 3.1: (a) The moving shock front as seen from reference frame fixed to earth; (b) The stationary shock front as seen from reference frame moving with the shock front.

medium. Mathematically, we can define a shock wave as any abrupt disturbance that propagates through the gas causing a change of state. The laser produced plasma expanding in high pressure ambient gas giving rise to shock wave in the medium is a typical example [92].

Figure 3.1(a) shows the propagation of a plane shock wave propagating from left to right in a medium with speed  $v_1 + v_s$ , assuming the fluid ahead of and behind the shock wave in a steady state described by the state variables in the figure. The flow velocity ahead of the shock is taken to be  $v_1$ , and the gas behind the shock is then set into motion with a velocity  $v_2$ . If  $v_1$  is set equal to zero it becomes a special case where flow velocity ahead of the shock is zero and shock moves with velocity  $v_s$ . We will solve for general case when  $v_1 \neq 0$ . Our goal is to determine the gas properties behind the shock wave such as density  $\rho_2$  and the flow velocity  $v_2$ .

To analyze the shock wave it is convenient to shift to a coordinate system moving along with the shock as shown in Fig.3.1(b). The conservation equations for any control volume are

The continuity equation :

$$\frac{\partial \rho}{\partial t} + \frac{\partial}{\partial x}(\rho v) = 0. \quad (3.26)$$

The momentum equation :

$$\frac{\partial}{\partial t}(\rho v) + \frac{\partial}{\partial x}(P + \rho v^2) = 0. \quad (3.27)$$

The energy equation :

$$\frac{\partial}{\partial t}(\rho U + \frac{\rho v^2}{2}) + \frac{\partial}{\partial x} \left[ \rho v \left( H + \frac{P}{\rho} \right) \right] = 0. \quad (3.28)$$

$$\text{Where,} \quad U = C_v T \quad (3.29)$$

$$\text{and} \quad H = U + \frac{P}{\rho} \quad (3.30)$$

Equation of state (for perfect gas) :

$$P = \rho R T. \quad (3.31)$$

For steady state flow the time derivative vanishes and the Eqns.(3.26 - 3.28) reduce to

$$\rho_1 v'_1 = \rho_2 v'_2 \quad (3.32)$$

$$P_1 + \rho_1 v'^2_1 = P_2 + \rho_2 v'^2_2 \quad (3.33)$$

$$H_1 + \frac{v'^2_1}{2} = H_2 + \frac{v'^2_2}{2} \quad (3.34)$$

$$P = \rho R T \quad (3.35)$$

where  $v'_1$  and  $v'_2$  are the velocities in the moving frame attached to the moving shock. In the stationary coordinate system flow velocities  $v_1$  and  $v_2$  are different from  $v'_1$  and  $v'_2$ . The thermodynamic properties such as pressure, density, temperature and speed of sound are not influenced by the transformation of coordinate system. The relations between the

flow velocities in the two transformations can be expressed as

$$v'_1 = v_s \quad (3.36)$$

$$v'_2 = v_s + (v_1 - v_2). \quad (3.37)$$

The flow Mach number,  $M_1$  is defined by

$$M_1 = \frac{v'_1}{a_1} = \frac{v_s}{a_1} = M_s \quad (3.38)$$

where  $a_1$  represents the velocity of sound. From the relation Eqns.(3.32 - 3.35) and Eqns.(3.36 - 3.38) and using the relation  $a_1 = \gamma R T$  in  $P = \rho R T$  one obtains

$$\frac{v_2 - v_1}{a_1} = \pm \frac{2}{\gamma + 1} \left( M_s - \frac{1}{M_s} \right) \quad (3.39)$$

$$\frac{P_2}{P_1} = \left[ \frac{2\gamma}{(\gamma + 1)} M_s^2 - \frac{(\gamma - 1)}{(\gamma + 1)} \right] \quad (3.40)$$

$$\frac{\rho_2}{\rho_1} = \frac{(\gamma + 1) M_s^2}{(\gamma - 1) M_s^2 + 2} \quad (3.41)$$

$$\frac{T_2}{T_1} = \left[ \frac{2\gamma M_s^2 - (\gamma - 1)}{(\gamma + 1)^2 M_s^2} \right] [(\gamma - 1) M_s^2 + 2] \quad (3.42)$$

For strong shocks,  $M_s \gg 1$ , Eqn.(3.41) reduces to

$$\frac{\rho_2}{\rho_1} \longrightarrow \frac{\gamma + 1}{\gamma - 1} \quad (3.43)$$

As the plasma moves at a velocity of  $10^6 - 10^7$  cm/sec into an ambient gas it acts as a supersonic piston giving rise to a shock wave which moves at a faster velocity than the piston [16]. For high pressure gas there is a constant discontinuity between the piston and the swept up gas and there hardly is any intermixing of the two. A rough sketch of the process is given in Fig.3.2. Region I, the undisturbed gas where pressure and temperature are  $P_0$  and  $T_0$ , region II is the compressed gas ahead of the plasma front and the region

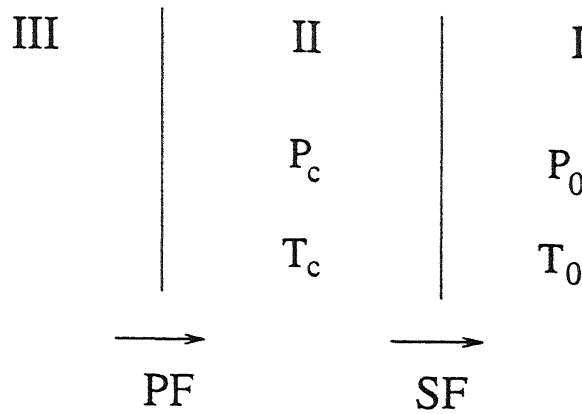


Figure 3.2: Region III is expanding plasma, region II is compressed gas and region I is the undisturbed gas shown in the reference frame fixed to the earth.  $P_0 / (P_c)$  and  $T_0 / (T_c)$  refer to pressure and temperature in region I and II respectively.

III is the plasma region. Between region III and II is the plasma front which is referred to as supersonic piston. Between region I and II is the shock front which is moving faster than the plasma front.

The velocity of the plasma front  $v_p$  and the velocity of shock front  $v_s$  are related by the expression [16]

$$v_s = \frac{(\gamma + 1)}{4} v_p + \sqrt{\frac{(\gamma + 1)^2}{16} v_p^2 + a_1^2} \quad (3.44)$$

The boundary condition on the region III is defined by the pressure and temperature of the region II. Here the pressure ( $P_c$ ) and temperature ( $T_c$ ) in compressed gas region II across a stationary shock front are given by (from Eqs. (3.40) and (3.42))

$$P_c = P_0 \left[ \frac{2\gamma}{(\gamma + 1)} M_s^2 - \frac{(\gamma - 1)}{(\gamma + 1)} \right] \quad (3.45)$$

$$T_c = T_0 \left[ \frac{2\gamma M_s^2 - (\gamma - 1)}{(\gamma + 1)^2 M_s^2} \right] [(\gamma - 1) M_s^2 + 2] \quad (3.46)$$

It follows from Eqn.(3.45) and Eqn.(3.46) that the boundary condition is changing with time, the changed boundary conditions are

$$\begin{aligned} P(R_0) &= P_0 \text{ if } M_s \leq 1 \\ &= P_c \text{ if } M_s > 1 \\ T_e(R_0) &= T_0 \text{ if } M_s \leq 1 \\ &= T_c \text{ if } M_s > 1 \end{aligned} \quad (3.47)$$

If the Mach number is less than or equal to unity then shock waves are not formed and the boundary conditions are defined by  $P_0$  and  $T_0$  but if Mach number is greater than unity then shock waves are formed and pressure and temperature are given by  $P_c$  and  $T_c$  respectively.

The boundary condition for the temperature is applicable to the electron temperature only. It is because of the higher concentration of electrons at the plasma front due to their higher mobility compared to ions. The velocity is being calculated at every step. That is, after every small time step the code calculates the plasma front velocity and simultaneously calculates the shock front velocity and the corresponding pressure at the boundary and with that pressure it calculates the next plasma front velocity and the process continues.

When plasma moves into an ambient gas it is almost similar to the case of hot jet coming out into ambient atmosphere. The moving plasma undergoes turbulent boundary layer mixing due to which it experiences viscous force on its boundary. According to Prandtl's mixing length theory, the total Reynolds stress due to turbulent mixing in the boundary layer is given by the expression [195].

$$\tau = \rho_0 \epsilon_r \frac{\delta v}{\delta y} = \rho_0 x_1 b_1 [v_{max} - v_{min}] \frac{\delta v}{\delta y} \quad (3.48)$$

where  $\rho_0$  is the density of ambient gas,  $\epsilon_r$  is kinematic viscosity,  $v_{max}$  is the velocity of the center of flow and  $v_{min}$  is at the boundary.  $x_1$  is an empirical constant to be determined from experiment,  $b_1$  is the width of the mixing zone.

At the outermost boundary, velocity is zero, so  $v_{min} = 0$  and writing  $v_{max} = v$ , Eqn.(3.48) simplifies to

$$\tau = \rho_0 x_1 v^2 \quad (3.49)$$

The shear force experienced by a particular mesh will be

$$F_{drag} = \tau(\delta l) \quad (3.50)$$

$\delta l$  is the length of a particular mesh which is varying with time. The Navier-Stokes equation ( Eqn.(3.24) ) changes to

$$\rho \frac{dv}{dt} = -\nabla p - \tau(\Delta l) \quad (3.51)$$

As the plasma front expands into the ambient gas the pressure just inside the boundary decreases and the pressure outside increases. At a later time the pressure inside the plasma front is comparable to the pressure outside. At that time the piston becomes leaky and outside gas diffuses into the plasma giving rise to collisions due to which the expanding plasma experiences a large resistive force,

$$F_{diff} \propto \left( \frac{P_{ext}}{P_{int}} \right)^{c_1} \rho_0$$

or

$$F_{diff} = c_2 \left( \frac{P_{ext}}{P_{int}} \right)^{c_1} \rho_0 \quad (3.52)$$

$p_{ext}$  is the pressure just outside the plasma front and  $p_{int}$  is the pressure just inside the plasma front. On addition of a diffusive term the modified Navier-Stokes equation reads

$$\rho \frac{dv}{dt} = -\nabla P - \tau(\Delta l) - F_{diff} = -\nabla P - \rho_0 x_1 v^2 - c_2 \left( \frac{P_{ext}}{P_{int}} \right)^{c_1} \rho_0 \quad (3.53)$$

This equation contains three constants viz.  $x_1$ ,  $c_1$  and  $c_2$  to be determined from the experiments.

The thermodynamics of the system changes in the presence of the ambient gas. The kinetic energy (KE) lost due to drag and diffusion is expressed as heat which increases the



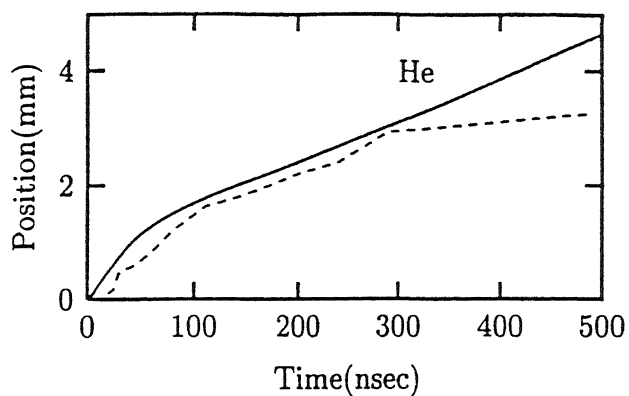
temperature of the expanding plasma. Some heat is also lost to the gas. For the sake of simplicity it is assumed that the heat lost to the surrounding gases is negligible, loss in KE is expressed as heat is,

$$\frac{1}{2}m[v_i^2 - v_f^2] = mC_p\theta(J_c) \quad (3.54)$$

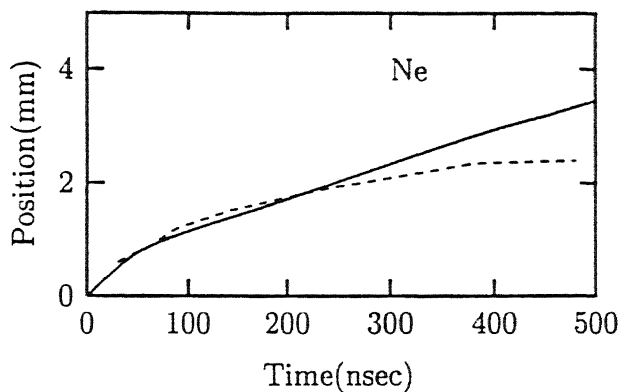
$J_c$  is joules constant,  $C_p$  is specific heat at constant pressure and  $\theta$  is the temperature difference. The heat lost to the shock wave and the work done in compressing the gas has been taken care of by the boundary conditions because it changes the pressure and temperature inside the plasma.

### 3.3 Results

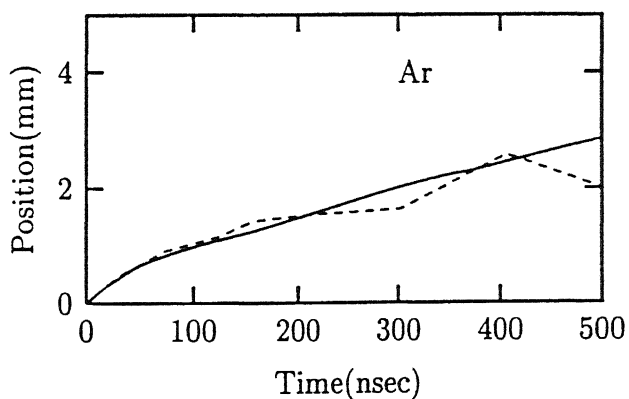
With the modifications as above viz. including the viscous and diffusive force in the Navier Stokes equation and changing the boundary conditions, the simulation is carried out (with an initial step of  $t=10^{-18}$  sec having mesh size of 60) and matched with the experimental data [93]. Here graphite target was ablated using KrF laser ( $\lambda = 248$  nm, 30-ns FWHM,  $2 \times 2$  mm<sup>2</sup> spot size on the target, fluence=20 J/cm<sup>2</sup>). The ablation was carried out in four different buffer gases at a pressure of 300 Torr. The temporal evolution of the plasma front as it propagates in He, Ne, Ar and Xe gas is shown in Fig.3.3(a) - 3.3(d). with a dotted line. One of the simulated curves for a particular gas (say Xe) is compared to the experimental curve and constants  $x_1$ ,  $c_1$  and  $c_2$  in Eqn.(3.53) are determined. It was found that  $x_1 = 2.0 \times 10^5$  /m<sup>2</sup>,  $c_1 = 1$  and  $c_2 = 1.0 \times 10^9$ /m<sup>2</sup>. These constants once determined are then used to get other simulated curves (in case of He, Ne and Ar) which are compared with respective experimental curves. The simulated results shown in solid line match well with the experimental results, shown in dashed line till 300 nsec. The plasma front propagates faster in lighter gas (like He) than denser gas (like Xe). It is interesting to note that after 300 nsec the simulated value is more than that of the experimental one. This is because after 300 ns the diffusion increases to such an extent that a reflected shock is generated within the plasma plume which moves in the opposite direction, towards the



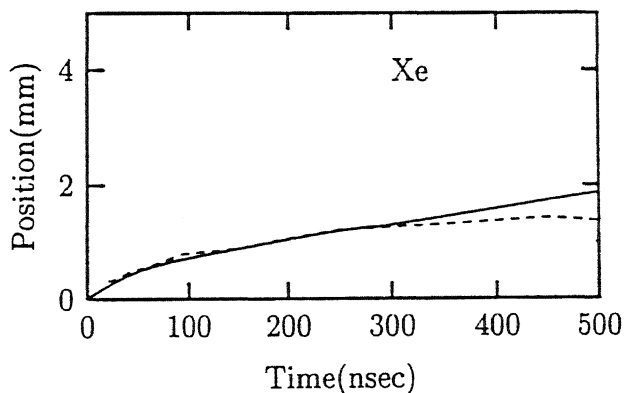
(a)



(b)



(c)



(d)

Figure 3.3: The position of the plasma front versus time in four different ambient gases (a) He (b) Ne (c) Ar and (d) Xe. Experiment (---) Simulation (—).

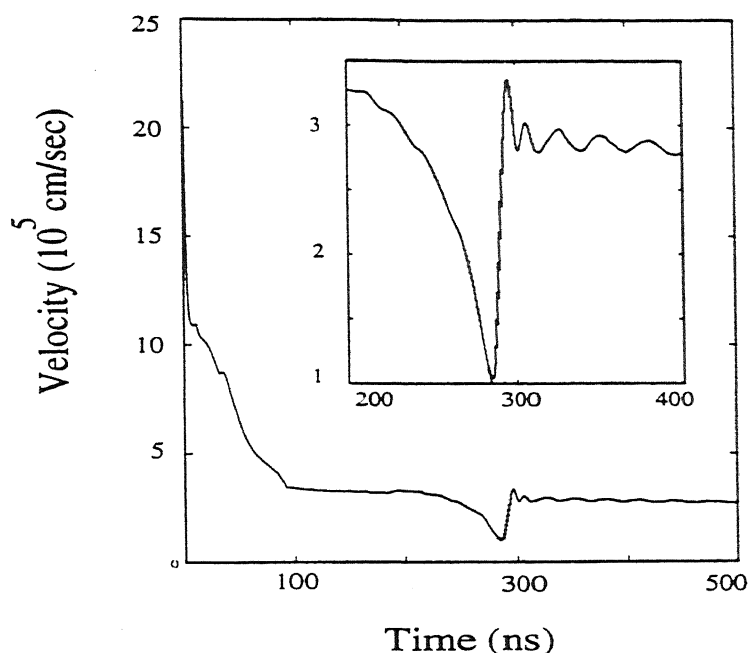


Figure 3.4: The simulated temporal profile of velocity of the plasma front in Xe gas. The inset shows the oscillations observed at around 300 ns on an enlarged scale.

target surface, damping the motion of the plasma as observed in the experiment. If there is mixture of fluids whose composition is different at different points then the equations of fluid dynamics have to be considerably modified [196]. A different set of equations are needed to model this part which are not considered by us.

Figure 3.4 shows simulated temporal profile of plasma front velocity with Xe gas as the background. The velocity decreases with time but at around 290 ns fluctuations in velocity are observed. Figure 3.5 shows the intensity of the shock wave going into the plasma as a function of time as observed in simulation. The shock intensity is maximum at around 290 ns, that is at the same time when velocity suddenly drops and increases again. Experimentally it was observed that a shock wave had gone into the plasma front at around 300 ns causing instability in the velocity of the plasma front. The simulated results match very well with the experiment. It has also been observed in simulation that the intensity of shock wave going into the plasma in case of He is orders of magnitude

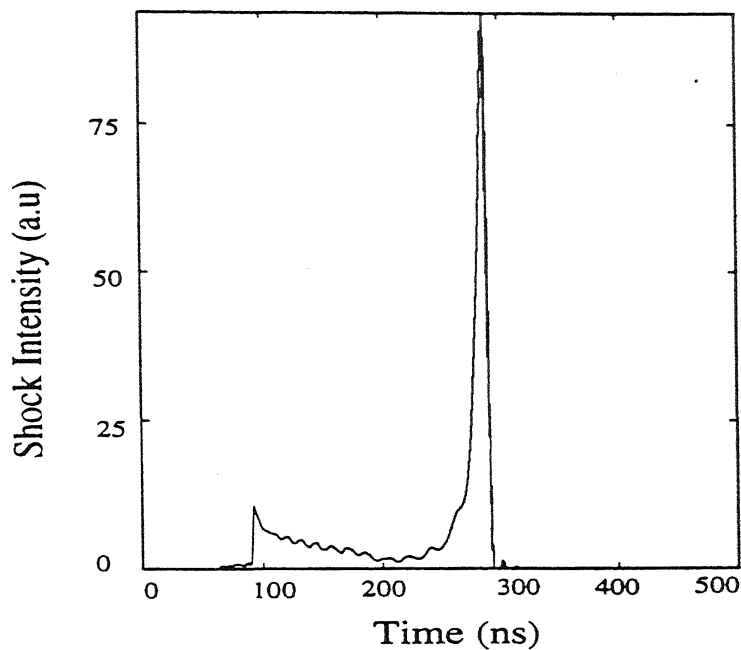


Figure 3.5: The simulated temporal profile of shock intensity at the plasma front in case of plasma expanding in Xe gas.

lower than that of Xe. It is because Xe being a denser gas gives a greater thrust to the moving plasma compared to that of He. Figure 3.3(d), that is position of the plasma front expanding in Xe and Fig.3.4 that is the velocity of the plasma front in the same ambient condition is replotted in Fig.3.6, with a common time axis, position and velocity axes are shown along the Y axis in left and right respectively. The whole graph is divided into seven different regions to show that slope of the position graph obtained by simulation gives the simulated velocity graph. For e.g. in region (f) the slope of the position curve suddenly tends to 0, the velocity also tends to 0 at that point as seen in the velocity curve whereas in region (d) and (g), the velocity is constant.

The simulated temporal profile of temperature, density, pressure and electron density of the plasma front in case of Xe (dashed line) and He (solid line) as buffer gas are shown in Fig.3.7 - 3.10. Xe being denser than He gives higher resistance to the moving plasma resulting in higher temperature, pressure, density and electron density of the plasma front. The temperature of the plasma front attains a maximum value at 30 nsec (Fig.3.7) which is the pulse duration of the laser used and then decreases due to the cooling effect of the inert

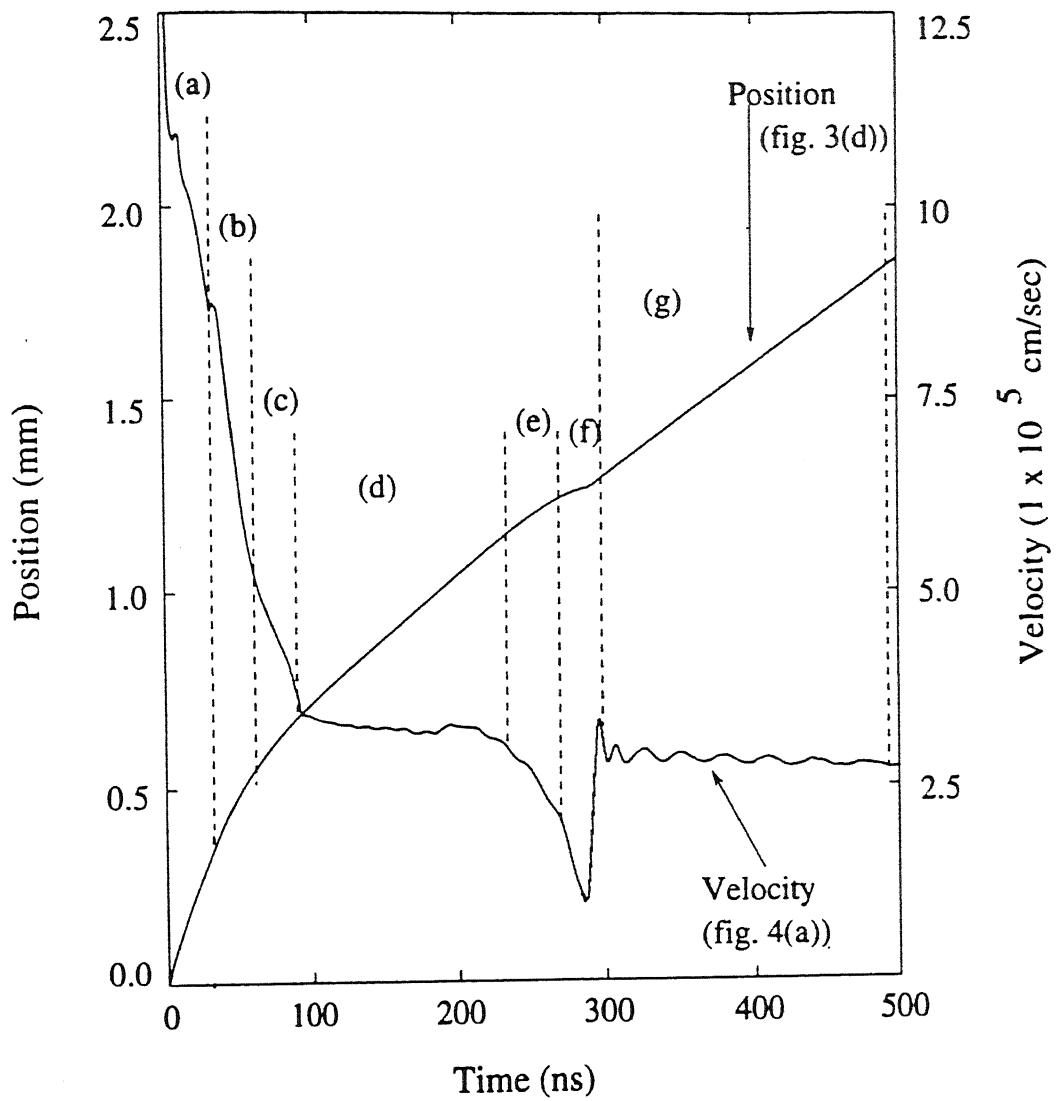


Figure 3.6: Fig.3.3(d) and Fig.3.4 are replotted with a common time axis.

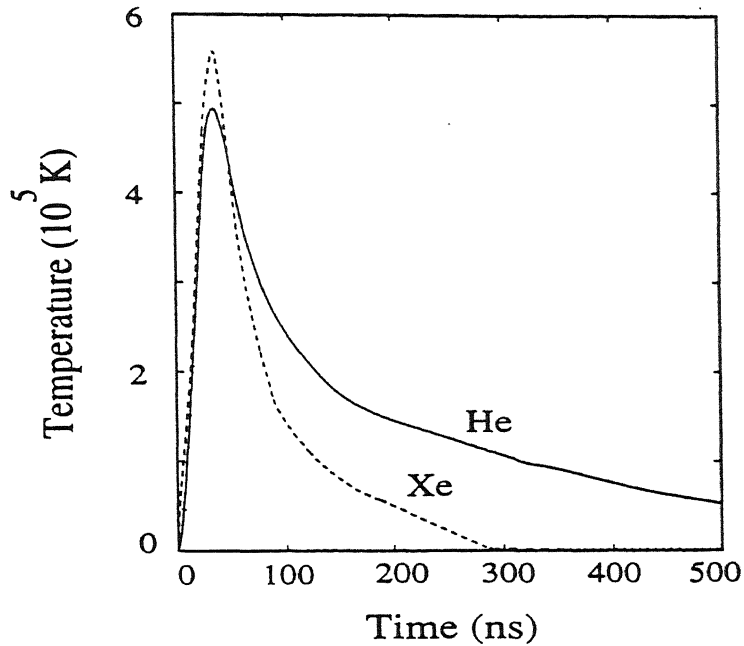


Figure 3.7: Temperature of the plasma front expanding in Xe and He as obtained from simulation. Dotted line is for the case of Xe and solid line for He as ambient gas.

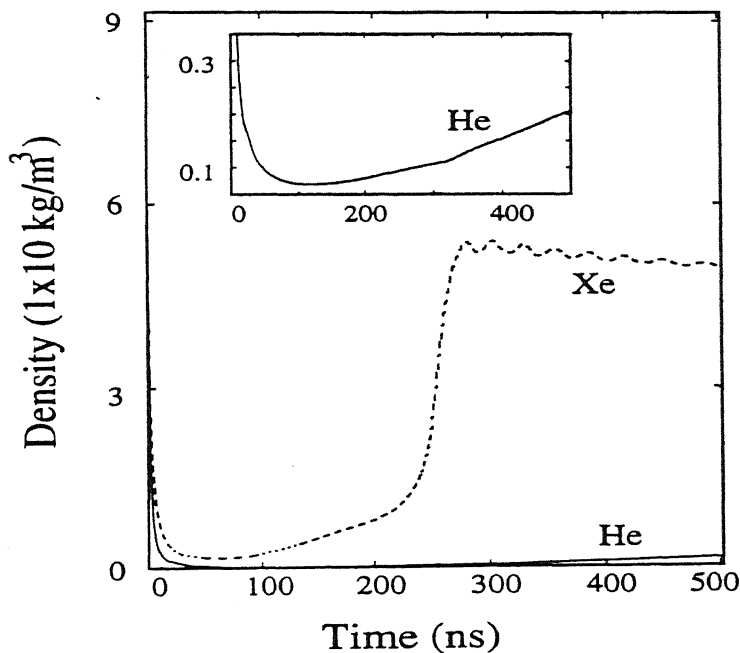


Figure 3.8: Density of the plasma front expanding in Xe and He as obtained from simulation. Dotted line is for the case of Xe and solid line for He as ambient gas. The inset shows density of the plasma front expanding in He on enlarged scale neglecting the initial points.

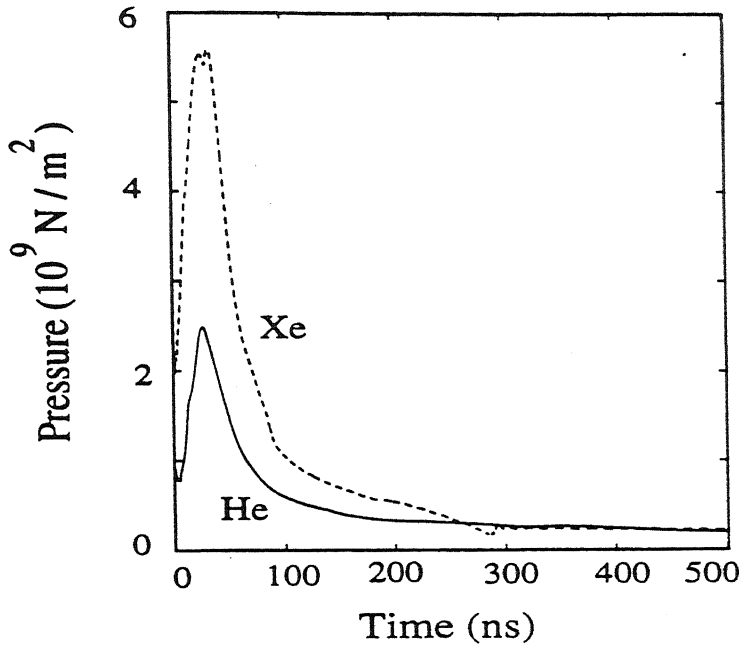


Figure 3.9: Pressure of the plasma front expanding in Xe and He as obtained from simulation. Dotted line is for the case of Xe and solid line for He as ambient gas.

gases. The density profile in case of Xe (Fig.3.8) shows a sudden rise at around 290 nsec due to shock wave coming into the plasma. However, rise in density at around 290 nsec (Fig.3.8) and fall in its temperature at the same time (Fig.3.7) give no significant change in pressure as expected from the perfect gas equation of state. Figure 3.9 shows a simulated pressure profile at 290 ns. The inset in Fig.3.8 and Fig.3.10 show the density profiles and electron density profiles for He on a magnified scale. It shows that electron density increases similar to that of Xe but increase is gradual and low in case of He compared to Xe where change is abrupt and high because of its higher density.

Figure 3.11 shows the effect of different terms which are added in the Navier-Stokes equation other than the boundary conditions. The viscous drag term plays the major role in decelerating the plasma front. The diffusive term comes into play at around 300 ns and is much less compared to viscous drag.

We applied our model to another experiment where excimer laser produced copper plasma was expanding in Ar, He, N<sub>2</sub> and H<sub>2</sub> at 5 mbar ambient pressure. Figure 3.12 gives the simulated temporal profile of electron density for four different gases. It is observed

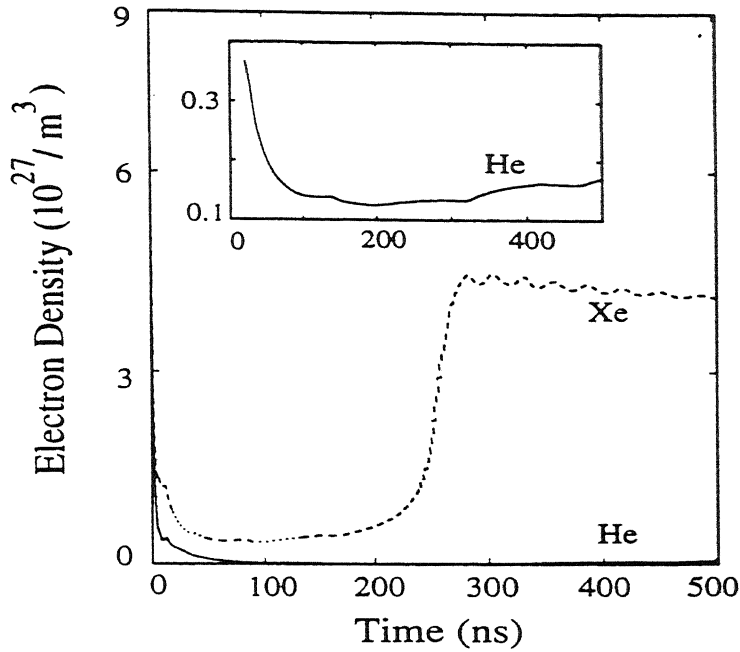


Figure 3.10: Electron density of the plasma front expanding in Xe and He as obtained from simulation. Dotted line is for the case of Xe and solid line for He as ambient gas. The inset shows electron density of the plasma front expanding in He on enlarged scale neglecting the initial points.

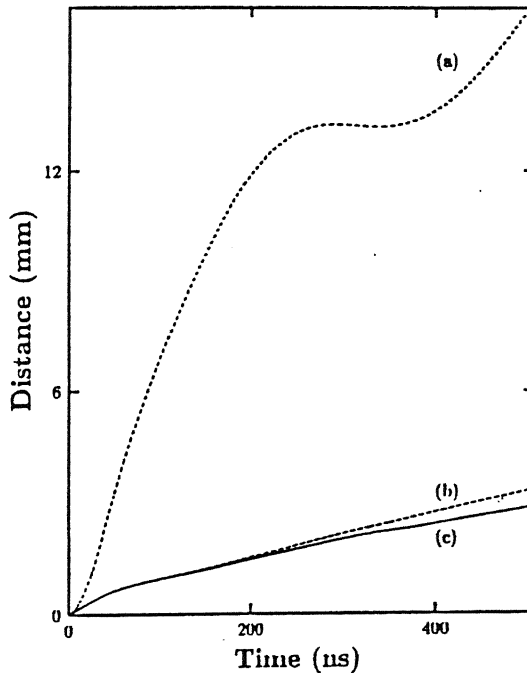


Figure 3.11: The simulated position of the plasma front as obtained from (a) Eqn.(3.24) i.e. no change in Navier-Stokes equation, (b) Eqn.(3.51) i.e. on adding viscous drag term only, (c) Eqn.(3.53) i.e. on adding viscous drag term and diffusive force term.



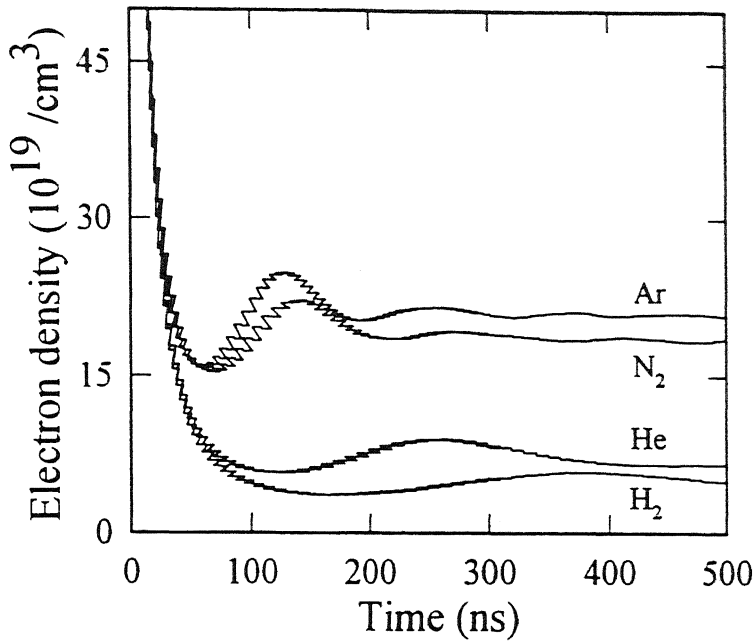


Figure 3.12: The electron density of the plasma front expanding in Ar, N<sub>2</sub>, He, H<sub>2</sub> as obtained from simulation.

that electron density is highest in the case of Ar followed by N<sub>2</sub>, He, and H<sub>2</sub> in agreement with the experimental observations [93].

Finally we applied our model to our own experiment in which laser ablated carbon plasma expanded in 100 mTorr air where the shock wave just forms. It is found that the position of the plasma front obtained from ICCD photographs matches very well with the simulated value for 100 mTorr air as shown in Fig. 3.13. The temperature of the plasma plume in vacuum matches well with the simulated value as shown in Fig. 3.14.

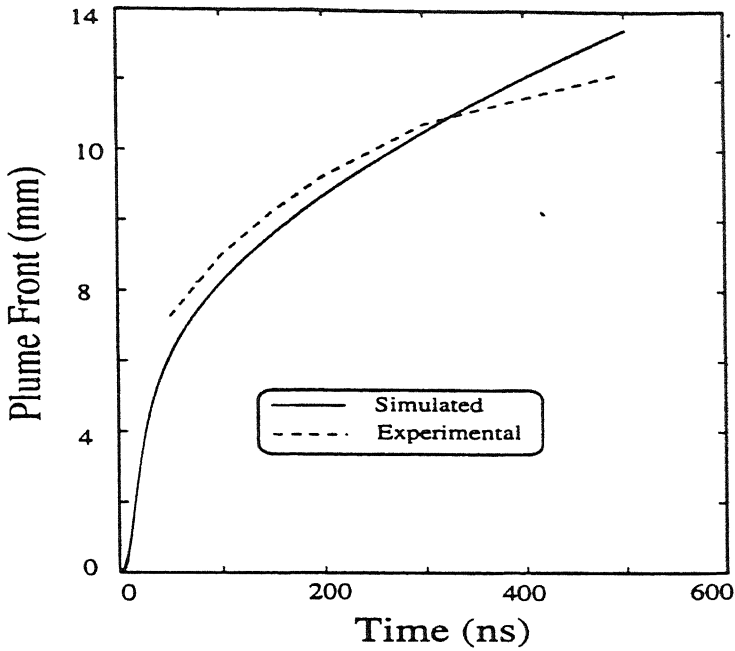


Figure 3.13: The position of the plasma front versus time in 100 mTorr ambient air. Experiment (---), Simulation (—).

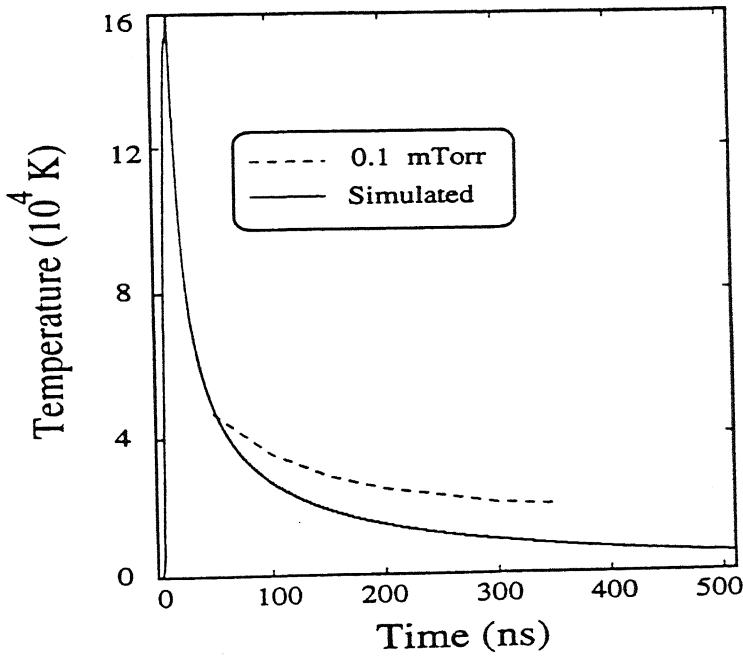


Figure 3.14: The temperature of the plasma plume versus time in vacuum. Experiment (---), Simulation (—).

## Chapter 4

# Laser Produced Carbon Plasma in Low Pressure Ambient Atmosphere

---

### 4.1 Introduction

A high temperature and high density transient plasma produced by focusing the output from a Q-switched laser onto a solid target has attracted a great scientific concern due to its recent technological applications, in particular to material research [10], fluid dynamics [196], cosmology [197], chemical physics [112] and many other fields. Laser ablated plasmas of metals in presence of background gas have been used in the recombination phase for the generation of laser oscillations [198, 199] and as strong x-ray and vacuum ultra-violet sources [200, 201]. The interaction between the laser plasma and ambient gas provides information on collisional, collective and electromagnetic processes in astrophysical and laboratory plasmas [8]. Since the background gas effectively controls the plasma parameters important for numerous technological applications, the knowledge of

---

<sup>0</sup>The work presented in this Chapter is based on :

1. "Dynamics of laser produced carbon plasma expanding in low pressure ambient atmosphere", A. Neogi, A. Mishra and R. K. Thareja, *J. Appl. Phys.* **83**, 2831 (1998).

the dynamics of the plasma plume expanding in ambient atmosphere is indispensable.

There have been several reports regarding the propagation of laser produced plasmas in ambient atmosphere, however, the dynamics of carbon plasma expansion in ambient gas at low pressure is still not clear. In the present Chapter a detailed study of laser produced carbon plasma expanding in vacuum (0.1 mTorr) and low pressure ambient atmosphere (5 mTorr and 100 mTorr) is presented using ICCD photography and time resolved emission spectroscopy. The plasma plume is observed to break into fast and slow components in 5 mTorr air. Double peak structure is observed in the temporal profile of CI, CII and CIII transitions. Probable reasons for the stratification of the plasma and double peak behavior are discussed.

## 4.2 Experimental Details

The experimental set up used in the present study is described in Chapter 2. The energy of the laser pulse was 800 mJ/pulse, and was focussed on to the rotating graphite target resulting in irradiance of  $\sim 1.22 \times 10^{11}$  Watt/cm<sup>2</sup>. The plasma expanding in 0.1 mTorr, 5 mTorr and 100 mTorr air was studied using ICCD photography and emission spectroscopy.

## 4.3 Results and Discussion

### 4.3.1 ICCD Photography

Figure 4.1 shows ICCD photographs of the plasma plume at three pressures 0.1 mTorr, 5 mTorr and 100 mTorr at various delays with respect to ablating laser pulse with 20 ns exposure time. Each image is normalized to its maximum intensity. In vacuum the images were visible till 500 ns and became highly diffused beyond 500 ns. On increasing the pressure to 5 mTorr a significant increase in intensity was observed. At 600 ns the plume breaks into two components, fast and slow. The velocity of the two components is estimated to be  $1.0 \times 10^6$  cm/sec and  $7.5 \times 10^5$  cm/sec and hence termed as fast and slow components. The fast component is bulky consisting of the major part of the plume and the slow component is the minor component as shown in Fig.4.1. This trend was seen

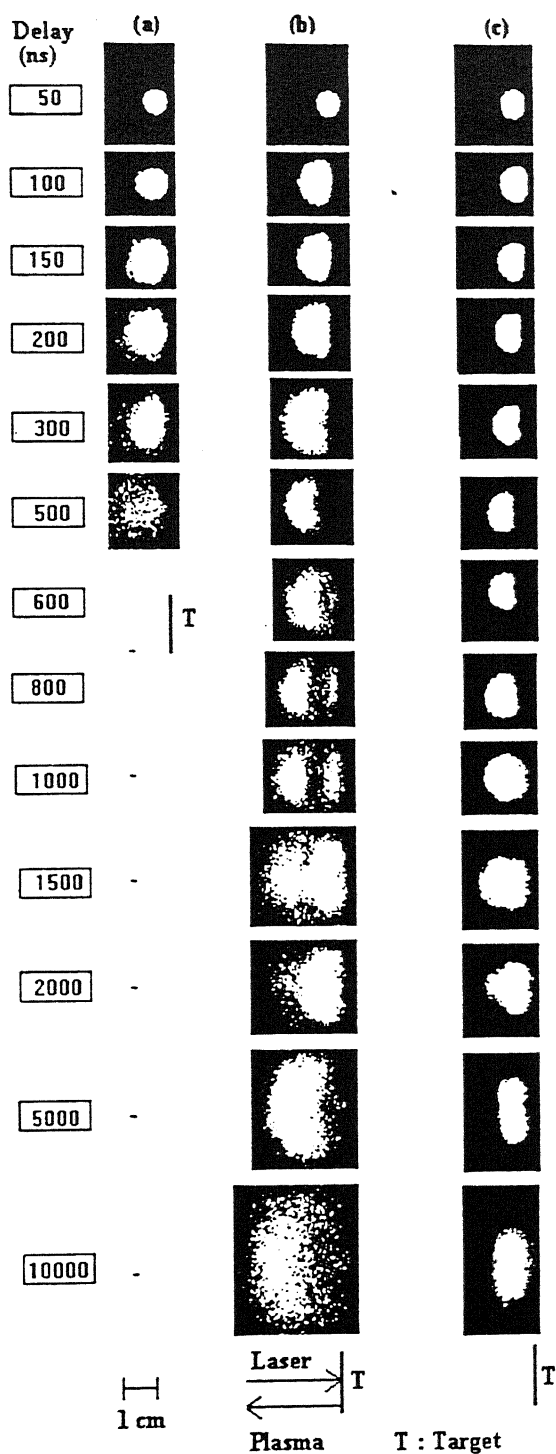


Figure 4.1: The ICCD photographs of the carbon plasma plume (exposure time = 20 ns) at various time delays (a) 0.1 mTorr, (b) 5 mTorr and (c) 100 mTorr.

in all other subsequent photographs. However, at 1500 ns the slow component became bulky with the fast component becoming the minor component. At around 2000 ns only one component is observed. At later times the plume remains as a single component of an irregular shape similar to that observed by Anan'in et al [25]. At 100 mTorr the stratification of the plasma plume is not observed. The dimensions of the plume get reduced due to pressure of the ambient gas from outside.

### 4.3.2 Emission Spectroscopy

The time resolved emission spectra of carbon plasma were recorded at different distances away and parallel to the target surface by moving the monochromator in a plane perpendicular to the target surface. The temporal profile of CI transition  $2p^3\ ^3D^0 - 8f\ F(5/2)$  at 399.7 nm, CII transition  $3d\ ^2D - 4f\ ^2F^0$  at 426.7 nm, CIII transition  $3s\ ^3S - 3p\ ^3P^0$  at 465.0 nm and CIV transition  $3s\ ^2S - 3p\ ^2P^0$  at 580.1 nm were recorded at different distances from the target surface at various pressures of air. Each of these transitions is one of the strongest transitions in their respective ionic states. The emission lines are identified using the information available in the literature [184]. Velocity, intensity and nature of the temporal profile of all different species are studied in vacuum (0.1 mTorr) and low pressure ambient atmosphere (5 mTorr and 100 mTorr) [The Fortran program used to calculate these parameters is included in the appendix A].

The velocity of each of the species CI, CII, CIII and CIV is calculated from the delay of the peak of the signal at different distances with respect to the trigger pulse [10,12]. It is observed that CIV ions have the highest velocity followed by CIII, CI and CII ions in case of vacuum. The expansion velocity of various species at a distance of 4 mm from the target surface is shown in Table 4.1.

The difference in velocity for the different ions and neutrals can be explained in terms of mobility which is proportional to charge to mass ratio ( $q_i/m_i$ ). CIV ions have the highest mobility followed by CIII, CII and CI. As the plasma expands in vacuum, the electrons strive to overtake the ions resulting in an uncompensated space charge and electric field

Table 4.1: Velocity of different species of carbon in 0.1 mTorr, 5 mTorr and 100 mTorr of air.

Species	Velocity ( $10^6$ cm/sec)		
	P = 0.1 mTorr	P = 5 mTorr	P = 100 mTorr
CI	1.58	1.75	1.62
CII	1.24	1.90	2.16
CIII	1.76	1.71	1.50
CIV	1.90	1.65	1.54

that decelerates the electrons and accelerates the ions [77]. This results in higher velocity for high ionic state. The reason for the observed velocity of CII lower than that of CI is not clear. It may be due to the fact that CII ions experience Coulomb repulsion on account of higher positive charge of CIII. The increase in pressure to 5 mTorr decreases the velocity of CIII and CIV ions as expected but the velocity of CI and CII ions increases as compared to their vacuum value. Here CII ions have the highest velocity followed by CI, CIII and CIV, as shown in Table 4.1. With a further increase in pressure to 100 mTorr, the velocity of CI species decreases (still greater than that in vacuum) along with CIII and CIV ions but the velocity of CII ions increases.

Figure 4.2 shows the variation in spectral line intensity of CI, CII, CIII and CIV transition with distance for three different pressures, 0.1 mTorr, 5 mTorr and 100 mTorr. The intensity of the spectral lines of the ionic species increases in presence of gas. Furthermore, it is observed that the line intensity in case of CIII transition increases as pressure is increased from 0.1 mTorr to 5 mTorr but it decreases again at 100 mTorr. This decrease in intensity after a certain critical pressure ( $\sim 100$  mTorr) is observed for species with higher charge (CIII, CIV) and not for species with lower charge (CI, CII). On the other hand, the intensity of CII and CI species increases in 100 mTorr after a certain critical distance compared to 5 mTorr. This increase in line intensity with external gas pressure and subsequent decrease after a certain critical pressure has also been observed earlier and the reasons for the above observation have been discussed by Abhilasha and Thareja [65].

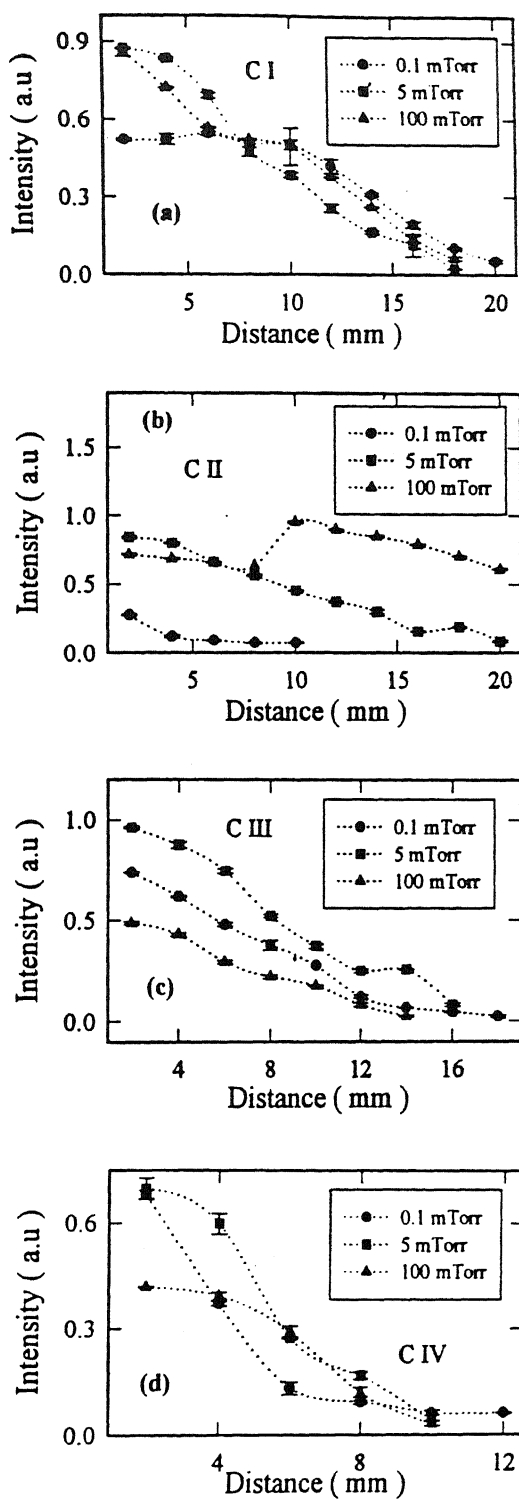


Figure 4.2: Spatial variation of the emission intensity of (a) CI, (b) CII, (c) CIII and (d) CIV transition in 0.1 mTorr, 5 mTorr and 100 mTorr of air.



Rise in emission line intensity in presence of gas (5 mTorr) is caused due to enhanced collisions of the plasma species with the external gas particles. However, when pressure is increased (100 mTorr), the external gas acts as a heat sink which lowers the temperature and favors three body recombination. The higher species recombine to give lower species which results in decrease in emission intensity for higher species (CIII and CIV) and increase in emission intensity for lower species (CII).

Now we discuss the nature of the temporal profile of various transitions in case of vacuum (0.1 mTorr), 5 mTorr and 100 mTorr of ambient pressure. In vacuum a single peak structure is observed for the transition of all the species. In presence of gas ( 5 mTorr and 100 mTorr ) a peculiar double peak structure is observed in the temporal profile of CI transition at 399.7 nm, CII transition at 426.7 nm and CIII transition at 465.0 nm as shown in Fig.4.3. Though the appearance of this double peak structure is reported due to stratification of the plasma into slow and fast components [25] but the reasons for this behavior are still not clear. Moreover, many important features of this double peak structure are overlooked. Some of the salient features of this structure observed experimentally by us are summarized below.

Double peak in the temporal profile is observed at 8 mm (from the target surface) for CI, CIII transition and at 10 mm for CII transition when pressure in the chamber is 5 mTorr. The peak which appears early in time i.e. the delay with respect to the ablating laser pulse is less, is termed as fast peak P1 whereas that which appears later or the delay with respect to ablating laser pulse is more is termed as slow peak P2. No double peak structure is observed for CIV transition. When pressure is increased to 100 mTorr, the onset distance for double peak decreases by 2 mm.

At 5 mTorr, it is found that the velocity of P1, the fast peak, is greater than that in vacuum where only single peak is observed as shown in Fig.4.3(a and b). The velocity of P2, the slow peak, is lower than the velocity of P1 for the transitions of CI, CII and CIII species. Figure 4.4(a-c) show the spatial variation of velocity of P1 and P2 at 5 mTorr and 100 mTorr case for the case of CI, CII and CIII transitions respectively. When the

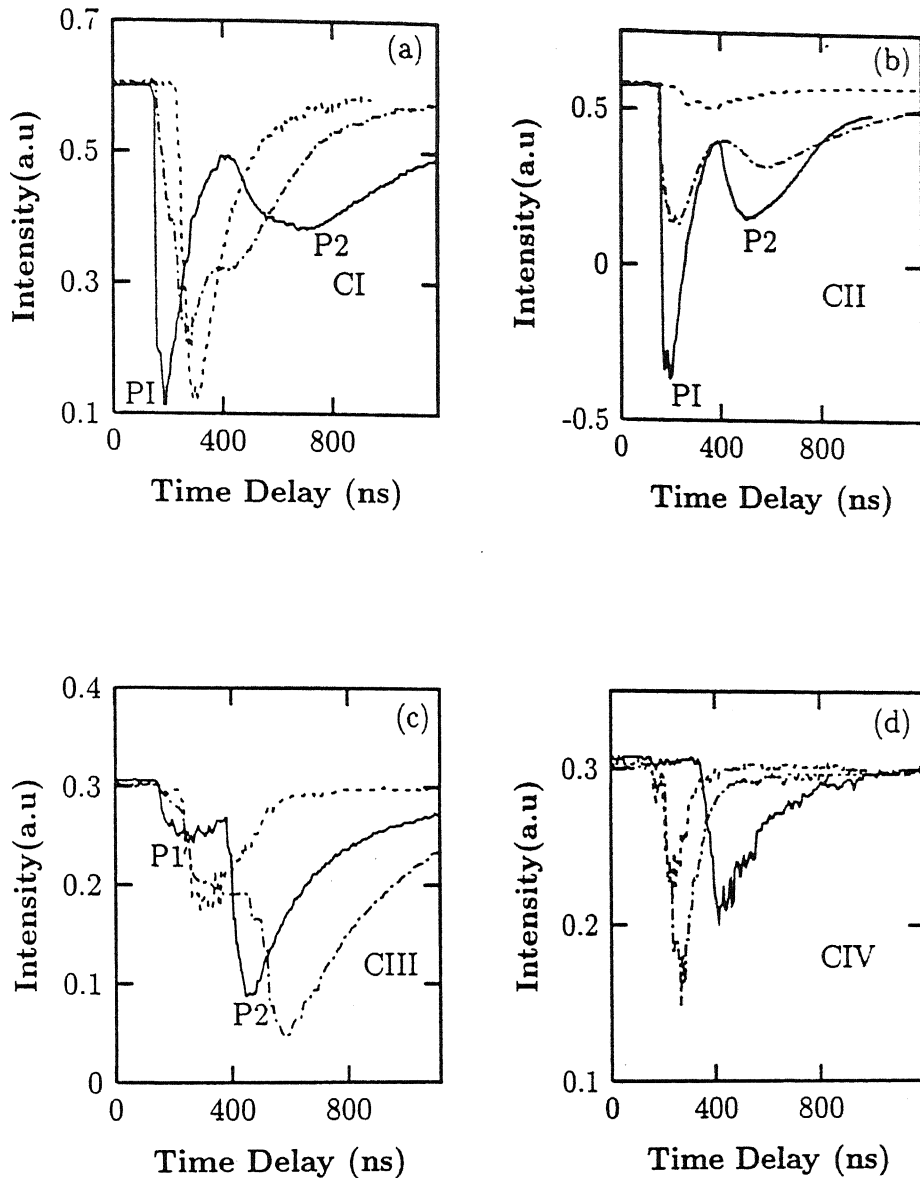


Figure 4.3: Temporal profile of CI transition at 399.7 nm, CII transition at 426.7 nm, CIII transition at 465.0 nm and CIV transition at 580.1 nm. P1 and P2 are respectively first and second peak (shown only for the 100 mTorr case). Dashed line (---) is for  $P = 0.1$  mTorr at a distance of (a) 10 mm (b) 10 mm (c) 12 mm (d) 8 mm. Dashed dot line (-.-.-) is for  $P = 5$  mTorr at a distance of (a) 10 mm (b) 10 mm (c) 12 mm (d) 8 mm. Solid line (—) is for  $P = 100$  mTorr at a distance of (a) 10 mm (b) 10 mm (c) 8 mm (d) 8 mm.

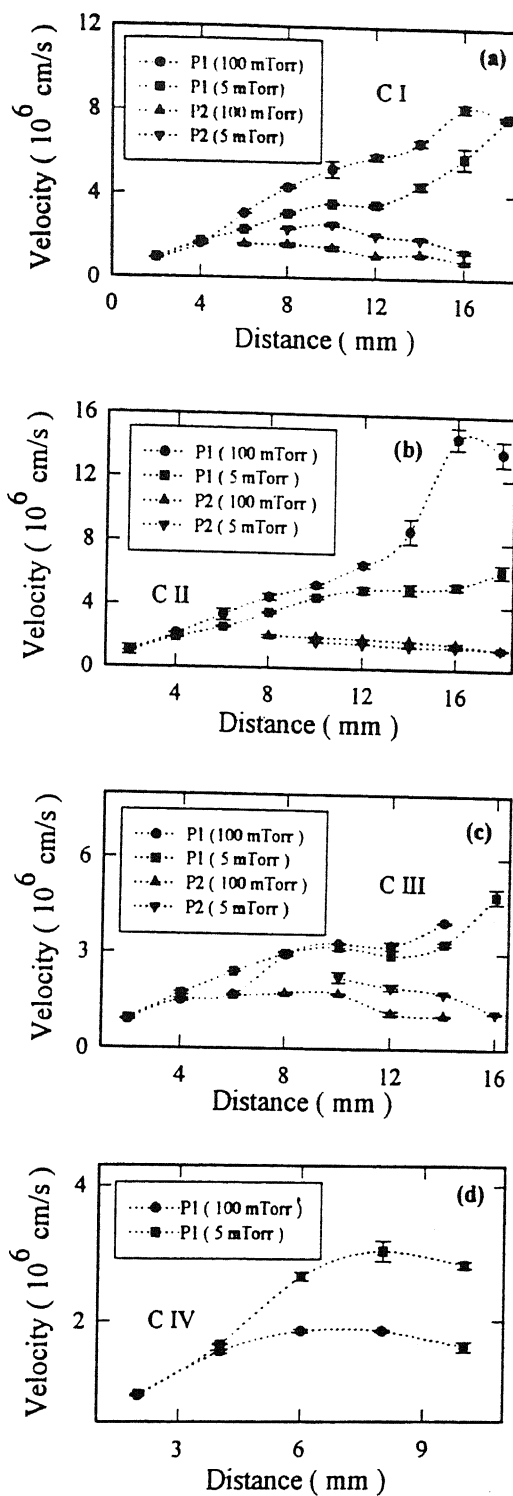


Figure 4.4: Velocity of fast ( $P_1$ ) and slow peak ( $P_2$ ) for (a) CI, (b) CII and (c) CIII species at 5 mTorr and 100 mTorr air respectively, (d) velocity of CIV species at 5 mTorr and 100 mTorr air respectively.

pressure of the ambient gas is increased from 5 mTorr to 100 mTorr it is found that velocity of P1 increases and that of P2 decreases (except in CII). Figure 4.4(d) shows the spatial variation of velocity of CIV species. The velocity of CIV ions decreases with the increase in pressure of the external gas and no double peak structure is observed (Fig.4.3(d)).

P1 accelerates with distance (till 18 to 20 mm) whereas P2 decelerates for 5 mTorr and 100 mTorr pressure for the transitions of CI, CII and CIII. A sudden rise in the acceleration of P1 at 14 to 16 mm for all the three transitions is observed.

It is observed that in case of 5 mTorr pressure, P1 is stronger than P2 till 12 mm for CI, till 14 mm for CII, till 10 mm for CIII respectively [Fig.4.3(a), (b), (c)] whereas at distances greater than 12, 14 and 10 mm for CI, CII and CIII respectively P2 is stronger than P1 as shown in Fig.4.5. The figure shows the temporal profile of CI, CII and CIII transition at 14 mm, 16 mm and 14 mm respectively. When pressure is increased to 100 mTorr, P1 remains stronger than P2 at all the distances for CI and CII transition as shown in Fig.4.3(a) and (b) whereas for CIII transition, P2 is stronger than P1 for all distances, Fig.4.3(c). The ICCD photographic observations are in accordance with spectroscopic observations where it is observed that P1 is stronger than P2 at earlier distance and P2 is stronger than P1 at later distance for all the three transitions.

The reasons for the stratification of the plasma plume expanding in low pressure ambient atmosphere as observed through ICCD photography, velocity of the different carbon species and double peak nature of the temporal profile of the carbon species and their relative intensities as observed through time resolved emission spectroscopy is explained below.

As the plasma front moves in an ambient gas, at earlier distances with respect to the target surface, the gas in front of it gets compressed due to its inability to move as fast as the plasma front. The plasma front gives a thrust on to the compressed gas which sends an equal and opposite compression pulse resulting in the compression of the plasma front. Once the compression pulse is over the thin compressed plasma front uncompresses itself due to which the velocity of the fast moving species closer to the plasma front decreases

whereas the velocity of the species in the core increases to conserve the momentum of the plume. Experimentally we have observed that the velocity of CI and CII ions increases whereas that of CIII and CIV ions decreases at 4 mm on changing pressure from 0.1 mTorr to 5 mTorr [Table 4.1].

A probable cause for the stratification of the plasma plume in case of 5 mTorr air may be the direct collisional ionization of the air close to the plasma front by the high energetic plasma constituents emanating from the ablated plume. These ionized species diffuse into the plasma front and collide with various carbon species in the plume. Since the Coulomb collision cross section depends on the velocity and charge, various carbon species in the plume will have different collision cross section. The collision cross section ( $\sigma_c$ ) due to Coulomb collision depends on the charge and velocity as [202]

$$\sigma_c \propto \frac{q_i^4}{v^4} \quad (4.1)$$

where  $q_i$  the charge of carbon species and  $v$ , the velocity of the species. The species with higher velocity and lower charge [CII] have lower collision cross section compared to the species with lower velocity and higher charge [CIII, CIV]. A rough estimate of the ratio of the collision cross section of the species CII : CIII : CIV is 1 : 22 : 79 for the 5 mTorr case. Since the collision cross section determines the relative number of collision so species with higher collision cross section [CIII, CIV] undergo more number of collisions compared to [CI, CII] (lower collision cross section). The collided species give rise to slow component P2 whereas uncollided species give rise to fast component P1. That is why it is observed that in case of CIII and CIV slow peak P2 is stronger whereas in case of CI and CII fast peak P1 is stronger. Due to the ongoing collision process P2 becomes stronger than P1 at a larger distance for all the species as shown in Fig.4.5.

In case of 100 mTorr double peak structure is observed spectroscopically but no stratification is observed in the ICCD photographs. The phenomena of stratification decreases in case of 100 mTorr due to the onset of shock wave ahead of the plasma front [78] which hinders the motion of the fast component. Furthermore, the dimension of the plume gets

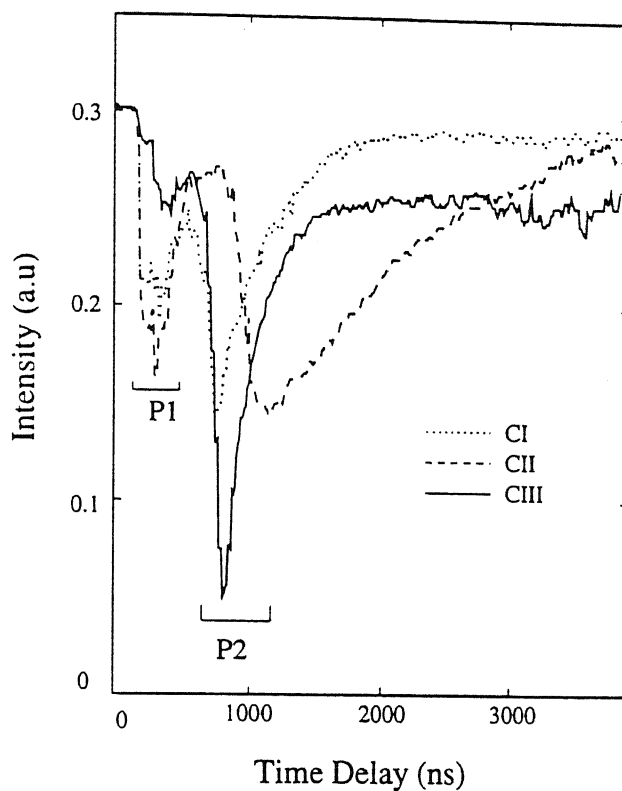


Figure 4.5: The temporal profile of CI transition (at 14 mm), CII transition (at 16 mm), CIII transition (at 14 mm) at 5 mTorr of air. The slow peak  $P_2$  is dominant in all the three cases.

reduced due to higher pressure from all sides and two separate fast and slow components are not resolved. However, in spectroscopy each species is observed individually so double peak structure is still observed in case of 100 mTorr whereas in case of ICCD photographs we observe the total emission from all the species, light emitted by fast and slow ions of different species merge together and the formation of stratification is lost.

As the shock front expands in 100 mTorr air, more and more background gas is swept up by the shock wave and the expansion velocity of the plasma plume decreases. This kind of non-steady shock wave is called a blast wave. Using Sedov's approach, the motion of the blast wave front is governed by the relation Eqn.(1.24)

$$S_t = C_0 \left( \frac{E_L}{\rho_0} \right)^{\frac{1}{3}} t^{\frac{2}{3}} \quad (4.2)$$

where  $C_0$  is a constant which depends on specific heat ratio of gas,  $E_L$  is the laser energy and  $\rho_0$ , the density of the ambient gas. The above equation is derived for a strong explosion and assuming that the entire mass encompassed by the explosion wave is concentrated in a thin layer behind the front surface [50]. The R-t plot giving the displacement of the luminous front with time at 100 mTorr along with a fit to shock model  $S_t = a_0 t^p$  is shown in Fig.4.6. The value of p is found to be 0.28 comparable to the theoretical value of 0.4.

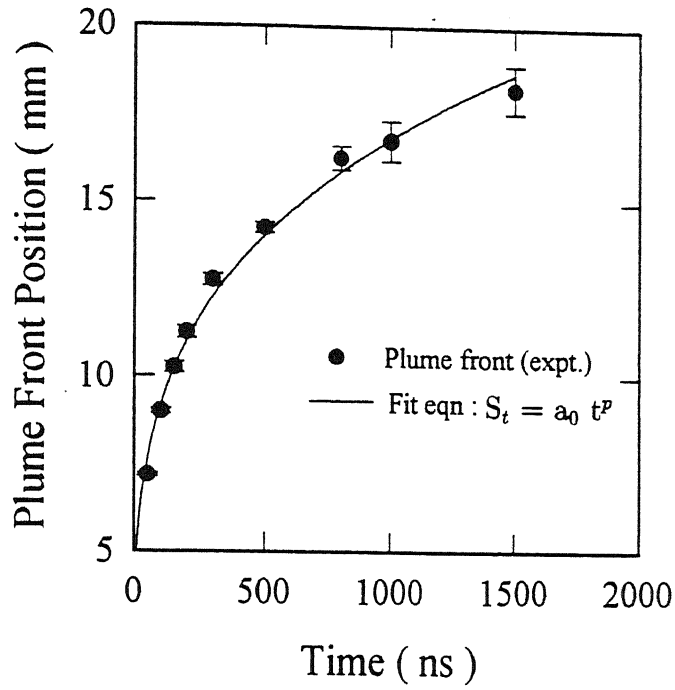


Figure 4.6: Experimentally observed plume front is fitted with the equation  $S_t = a_0 t^p$



# Chapter 5

## Laser Produced Carbon Plasma in a Nonuniform Magnetic Field

---

### 5.1 Introduction

The expansion of plasma produced by focussing an intense pulsed laser beam in a magnetic field is a rich and complicated phenomenon occurring in many laboratory environments. Among a number of external control parameters, magnetic field can be applied to control the local plasma thermofluid characteristics from both macroscopic and microscopic viewpoints [26, 27] important for studying astrophysical processes and various technological applications

This Chapter deals with the studies of LPP expansion in nonuniform magnetic field using three diagnostics viz. ICCD photography, time resolved and time integrated emission

---

<sup>0</sup>The work presented in this Chapter is based on :

1. "Laser-produced carbon plasma expanding in vacuum, low pressure ambient gas and nonuniform magnetic field", A. Neogi and R. K. Thareja, *Phys. Plasmas* **6**, xxxx (1999).
2. "Dynamics of laser produced carbon plasma expanding in a nonuniform magnetic field" A. Neogi and R. K. Thareja, *J. Appl. Phys.* **85**, xxxx, (1999).
3. "Optical emission spectra of laser ablated carbon plasma in curved magnetic field" A. Neogi and R. K. Thareja, Communicated to *J. Appl. Phys.*

spectroscopy, and Langmuir probe. The Chapter starts with the basic theory of plasma behavior in magnetic field. The shape of the plasma expanding in vacuum, ambient gas and nonuniform magnetic field is observed through fast photography. The images are used to estimate the plasma parameters like electron density, electron temperature etc. [178]. The temporal profile of the different species of the carbon viz. CI, CII, CIII, CIV shows multiple peaks in nonuniform magnetic field [129]. The time integrated spectra of carbon plasma show the effect of curvature and gradient of magnetic field on the intensity of spectral lines and molecular  $C_2$  emission [147]. Finally the use of Langmuir probe to monitor plasma behavior has been discussed.

## 5.2 Laser Produced Plasma in Magnetic Field

Energy, momentum and Ohm's law equation for the plasma plume expanding in magnetic field is given below [120].

### 5.2.1 Basic Equations of the Plasma in Magnetic Field

(1) Energy equation for plasma in magnetic field is derived from first law of thermodynamics ;

$$\frac{dQ}{dt} = \frac{dU}{dt} + \frac{dW}{dt} \quad (5.1)$$

where  $Q$ ,  $U$ , and  $W$  have usual meaning defined in Chapter 3, and

$$\frac{dQ}{dt} = P_L + W_s \quad (5.2)$$

where  $P_L$  is the laser power and  $W_s$  the heating due to surface current, and

$$\frac{dU}{dt} = \frac{d}{dt} \left[ \frac{3}{2} (N_e + N_i) k_B T \right] = \frac{3}{2} (N_e + N_i) k_B \frac{dT}{dt}, \quad (5.3)$$

$$\frac{dW}{dt} = P \frac{dV}{dt} = \frac{(N_e + N_i) k_B T}{\frac{4}{3} \pi r^3} \times 4 \pi r^2 \frac{dr}{dt}$$

$$\text{or} \quad \frac{dW}{dt} = \frac{3}{r} (N_e + N_i) T \frac{dr}{dt} \quad (5.4)$$

$$\text{and } W_s = \int i^2 R dV = \int \eta J^2 dV \quad (5.5)$$

where  $\eta$  is the plasma resistivity given by Spitzer [193] and  $\mathbf{J}$  is the surface current.

Magnetic field is assumed to decay exponentially into the plasma with skin depth  $\lambda$ , i.e. the depth at which field becomes  $1/e$  of its original value (at the boundary) as it propagates a distance  $\lambda$ ;

$$\text{i.e. } B \sim B e^{-r_1/\lambda}, \quad \text{for } 0 < r_1 < r \quad (5.6)$$

$$\text{Since } \mathbf{J} = \frac{\nabla \times \mathbf{B}}{4\pi},$$

from Eqn.(5.6), it follows

$$J = \frac{B}{\lambda} \frac{1}{4\pi} e^{-r_1/\lambda}, \quad (5.7)$$

$$W_s = \int \eta J^2 dV = \frac{\eta B^2}{8\pi\lambda} \left[ r^2 - r\lambda + \frac{\lambda^2}{2} (1 - e^{-\frac{2r}{\lambda}}) \right] \quad \text{at } r_1 = r \quad (5.8)$$

Combining Eqns.(5.1), (5.2), (5.3), (5.4) and (5.8) we get the energy equation in final form as

$$\frac{3}{2}(N_e + N_i) \frac{dT}{dt} + \frac{3}{r} \frac{dr}{dt} T(N_e + N_i) - P_L = \frac{\eta B^2}{8\pi\lambda} \left[ r^2 - r\lambda + \frac{\lambda^2}{2} (1 - e^{-\frac{2r}{\lambda}}) \right] \quad (5.9)$$

(2) The momentum equation is derived by equating the work done by the expanding plasmoid to the change in kinetic energy;

$$P \frac{dV}{dt} = \Delta \left( \frac{1}{2} \bar{M} v^2 \right) \quad (5.10)$$

In the presence of magnetic field the above equation changes to

$$P \frac{dV}{dt} = \Delta \left( \frac{1}{2} \bar{M} v^2 \right) + \int (\mathbf{J} \times \mathbf{B}) dV \frac{dr}{dt} \quad (5.11)$$

where the second term in the R.H.S arises due to expansion in magnetic field. From Eqns.(5.6) and (5.7) it follows

$$\int (\mathbf{J} \times \mathbf{B}) dV \frac{dr}{dt} = B^2 \left[ r^2 - 2r\lambda + 2\lambda^2 (1 - e^{-\frac{r}{\lambda}}) \right] \frac{dr}{dt} \quad (5.12)$$

Combining Eqn.(5.4) and (5.11), (5.12), we get

$$(N_e + N_i) \frac{T}{r} \frac{dr}{dt} - \frac{1}{2} \bar{M} \frac{d}{dt} \left( \frac{dr}{dt} \right)^2 = B^2 \frac{dr}{dt} \left[ r^2 - 2r\lambda + 2\lambda^2(1 - e^{-r/\lambda}) \right] \quad (5.13)$$

(3) The Ohm's law equation for the plasma motion in magnetic field is derived by equating the rate of change of total magnetic flux to the emf generated on the surface;

$$\frac{d}{dt} (Flux) = - \int \eta \mathbf{J} \cdot d\mathbf{l} = \frac{\eta r B}{2 \lambda} \quad (5.14)$$

where  $d\mathbf{l}$  is infinitesimal length along the plasma boundary

$$Flux = \int_0^r B(2\pi x) dx = \int_0^r B e^{-\frac{(r-x)}{\lambda}} (2\pi x) dx = 2\pi B \lambda \left[ r - \lambda(1 - e^{-r/\lambda}) \right]$$

∴ Ohm's law equation reduces to

$$\frac{d}{dt} \lambda \left[ r - \lambda(1 - e^{-r/\lambda}) \right] = \frac{\eta r}{4\pi \lambda} \quad (5.15)$$

Solving Eqn.(5.9), (5.13) and (5.15) for  $r$ , the radius of the plasma plume, one obtains an energy integral equation,

$$\begin{aligned} \frac{B^2}{3} [r_b^3 - r_0^3] &= \frac{3}{2} (N_e + N_i) k_B T_0 r_0^2 \left( \frac{1}{r_0^2} - \frac{1}{r_b^2} \right) + \frac{1}{2} \bar{M} v_0^2 \\ &+ 2B^2 \left[ \int_0^t F_2(r, \lambda) \frac{dr}{dt} dt \right] + \int_0^t (N_e + N_i) k_B \frac{f_1(t)}{r^3} \frac{dr}{dt} dt. \end{aligned} \quad (5.16)$$

where

$$f_1(t) = \int_0^t dt' \frac{2}{3} \frac{\eta(t') B^2 r(t')^2}{8\pi (N_e + N_i) \lambda(t')} \left[ r^2 - r\lambda + \frac{\lambda^2}{2} (1 - e^{-2r/\lambda}) \right],$$

$$\text{and} \quad F_2(r, \lambda) = r\lambda - \lambda^2(1 - e^{-r/\lambda})$$

where  $r_0$  and  $T_0$  are the initial radius and temperature of the plasmoid just after the laser pulse,  $N_e/(N_i)$  is total number of electrons or ions,  $\bar{M}$  the average mass of the plasmoid,  $B$ , the magnetic field and  $r_b$  is the radius of plasmoid where  $v = 0$ , this is usually referred to as "bounce" radius. The function  $f_1(t)$  is proportional to the resistivity  $\eta$  and  $F_2(r,$

$\lambda$ ) depends on the skin depth  $\lambda$ . The first and second terms on the right hand side of Eqn.(5.16) refer to thermal and kinetic energy respectively, third and fourth terms arise due to finite resistivity of the plasma. Radiation loses are not taken into account in arriving at Eqn. (5.16). Solving for  $r_b$ , we have

$$r_b^3 \simeq \frac{3}{2} \frac{\dot{M} v_0^2}{B^2} + \frac{9}{2} (N_e + N_i) k_B T_0 + 6 \int_0^t \frac{dr}{dt} F_2(r, \lambda) dt \\ + \frac{3}{B^2} (N_e + N_i) k_B \int_0^t \frac{f_1(t)}{r^3} \frac{dr}{dt} dt \quad (5.17)$$

It follows from Eqn.(5.17), the plot of  $r_b$  with time has an oscillatory nature. The radius of the plasma plume shows periodic bounce, i.e positions of  $v = 0$ . If the resistivity is zero the bounce radius remains constant and lines of force cannot diffuse into the plasma whereas if the resistivity is finite the magnetic field line slowly diffuses into the plasma and the bounce radius increases with time and oscillations stops.

### 5.2.2 Diamagnetic Behavior in Magnetic Field

The motion of plasma in magnetic field is analogous to a number of loops moving through a magnetic field. For a loop travelling through a magnetic field, the induced emf  $\varepsilon$  is given by

$$\varepsilon = -\frac{d\phi}{dt} = IR \quad (5.18)$$

where  $\phi$  is the flux,  $I$ , the current and  $R$  is the resistance. Plasma being conducting fluid, we can assume,  $R = 0$ . Eqn.(5.18) gives

$$-\frac{d\phi}{dt} = 0$$

or

$$\phi = \text{Constant} \quad (5.19)$$

It implies that magnetic flux through any surface in the fluid tends to remain constant as that surface moves with the fluid. Lines of force are "frozen in" with conducting fluid. Motion of field lines with respect to the plasma is possible only if resistivity is not zero. The magnetic flux across the plasma surface can change only if the magnetic field diffuses into the plasma which is determined by the resistivity of the plasma. The magnetic field behaves diamagnetically i.e. the field within the plasma is less than that in the surrounding space. This results in the retardation of the motion of the plasma across the field lines.

### 5.2.3 $\beta$ and Magnetic Reynold's Number $R_m$

As the plasma moves in a magnetic field  $\mathbf{B}$ , the charged particles experience a force perpendicular to the motion of the plasma and applied magnetic field due to which a surface current is generated perpendicular to the moving plasma. Mathematically,

$$\mathbf{F} = nq\mathbf{v} \times \mathbf{B} \quad (5.20)$$

where  $n$  is the number of particles

or

$$\mathbf{F} = \mathbf{J} \times \mathbf{B} \quad (5.21)$$

where  $\mathbf{J} = n q \mathbf{v}$ , is the surface current.

From Maxwell equation

$$\mathbf{J} = \frac{\nabla \times \mathbf{B}}{4\pi} \quad (5.22)$$

$$\therefore \mathbf{J} \times \mathbf{B} = -\frac{1}{4\pi} \mathbf{B} \times \nabla \times \mathbf{B} \quad (5.23)$$

But

$$\mathbf{B} \times \nabla \times \mathbf{B} = \nabla \left( \frac{B^2}{2} \right) - (\mathbf{B} \cdot \nabla) \mathbf{B} \quad (5.24)$$

On substituting Eqn.(5.24) in Eqn.(5.23) we get

$$\mathbf{J} \times \mathbf{B} = -\nabla \left( \frac{B^2}{8\pi} \right) + \frac{1}{4\pi} (\mathbf{B} \cdot \nabla) \mathbf{B} \quad (5.25)$$

where  $\frac{B^2}{8\pi}$  is the magnetic energy density which plays the role of magnetic pressure. The term  $\frac{1}{4\pi}(\mathbf{B} \cdot \nabla)\mathbf{B}$  arises due to curvature of the field. If the field is unidirectional i.e.  $\mathbf{B} \cdot \nabla = 0$ , Eqn.(5.26) reduces to

$$\mathbf{J} \times \mathbf{B} = -\nabla\left(\frac{B^2}{8\pi}\right) \quad (5.26)$$

$\beta$  is defined as the ratio of the particle pressure to the magnetic pressure, viz.

$$\beta = \frac{\text{Particle Pressure}}{\text{Magnetic Pressure}} = \frac{P}{B^2/8\pi} = \frac{nk_B T}{B^2/8\pi} \quad (5.27)$$

In our experiments we have  $n \sim 10^{17} / \text{cm}^3$ ,  $T \sim 7\text{eV}$  and  $B = 3 \text{ kG}$  at 2 mm from the target (section 4.2) and hence  $\beta$  comes out to be 3. The plasma pressure being higher than the magnetic pressure, the plasma "punches" its way across the magnetic field. As the plasma expands the  $\beta$  value rapidly decreases, approaching unity. Magnetic field simply diffuses into the plasma and the plasma becomes electrically polarized, the electric field  $\mathbf{E}$  is established which is perpendicular to both  $\mathbf{B}$  and the plasma velocity. The plasma moves across the  $\mathbf{B}$  field by  $\mathbf{E} \times \mathbf{B}$  drift. The plasma expansion ceases when the displaced magnetic energy approximately equals the kinetic energy of the plasma expansion.

Magnetic Reynolds number  $R_m$  determines the degree of magnetic field distortion of lines. For  $R_m > 1$ , the background field lines ahead of the flowing plasma will be distorted and compressed whereas for  $R_m < 1$ , the external field lines will be relatively unaffected and simply diffuse through the expanding plasma.

To get  $R_m$  we start with the equation for the evolution of the magnetic field

$$\frac{\partial \mathbf{B}}{\partial t} = \nabla \times (\mathbf{v} \times \mathbf{B}) + n_m \nabla^2 \mathbf{B} \quad (5.28)$$

where  $n_m$  is called the magnetic viscosity defined by

$$n_m = \frac{1}{(4\pi\sigma_0)} \quad (5.29)$$

where  $\sigma_0$  is the longitudinal conductivity i.e. conductivity parallel to the  $\mathbf{B}$  field [6]. The

first term on the right hand side of Eqn.(5.28) is called the flow term while the second term is called the diffusive term. The ratio of the flow term to the diffusive term gives the magnetic Reynolds number [6], viz.

$$R_m = \frac{vL}{\eta_m} \quad (5.30)$$

where  $v$  is the velocity of the fluid plasma,  $L$  the magnetic field gradient scale length and  $\eta_m$  the magnetic viscosity.

Using our experimental value we get  $R_m \sim 5$  i.e the flow term dominates over the diffusive term which inturn results in compression of magnetic field lines.

## 5.3 Experimental Techniques

The experimental set up used in the present study is described in Chapter 2. The field is maximum (3.5 kG) at the middle of the poles and decreases on either sides (along X axis) whereas along the Z direction it is minimum at the middle and maximum (5.1 kG) at the pole surface. The distance between the poles is 3.2 cm. The target is kept in between the pole pieces at one extreme end. The energy of the laser pulse used is 800 mJ/pulse having wavelength of 1.06  $\mu\text{m}$ .

## 5.4 Results and Discussions

### 5.4.1 ICCD Photography

The plasma expansion in vacuum ( $< 1$  mTorr), 100 mTorr air and non-uniform magnetic field in vacuum was recorded by ICCD camera at different delay times. Figure 5.1 shows ICCD images at different delay times. The exposure time for all these photographs is kept constant (20 ns) so that relative intensity can be compared. In order to view the real size of the images of varying intensity, each plume is normalized with respect to its maximum intensity.

The displacement of the luminous plasma front with respect to the target position



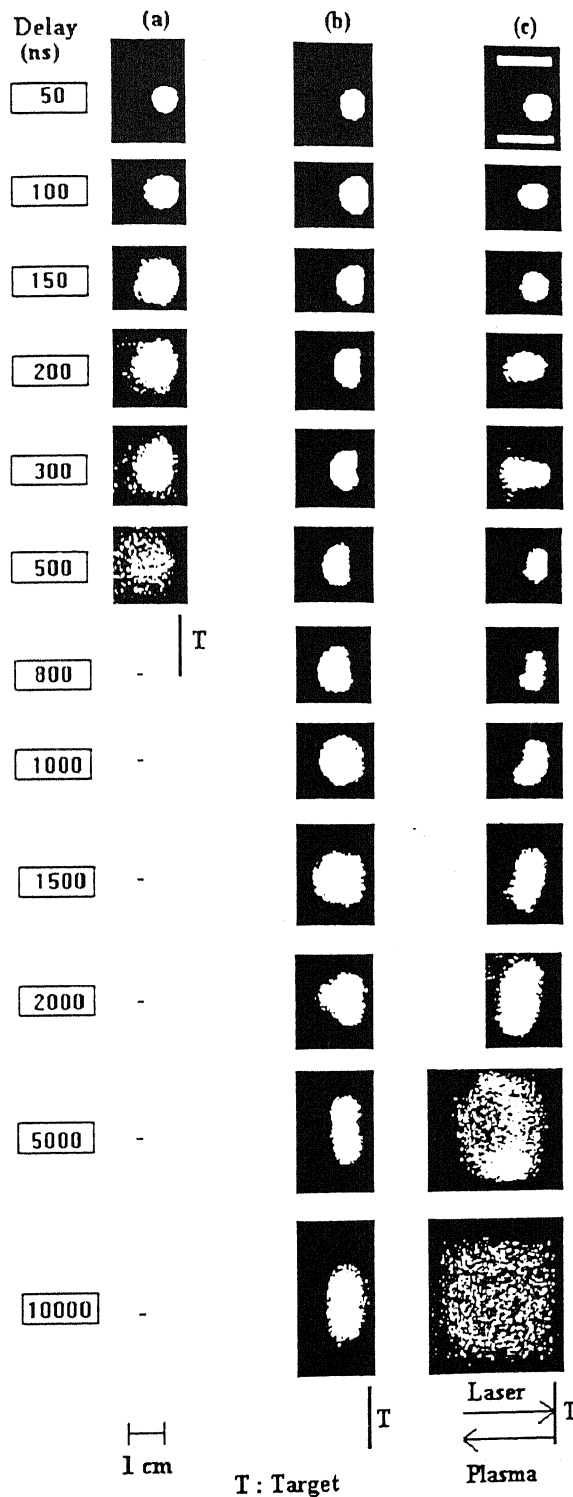


Figure 5.1: ICCD pictures of the plasma at different delay times with 20 nsec exposure. The images are normalized with respect to the maximum intensity of each image. (a) Vacuum, (b) 100 mTorr air and (c) Variable magnetic field in vacuum.

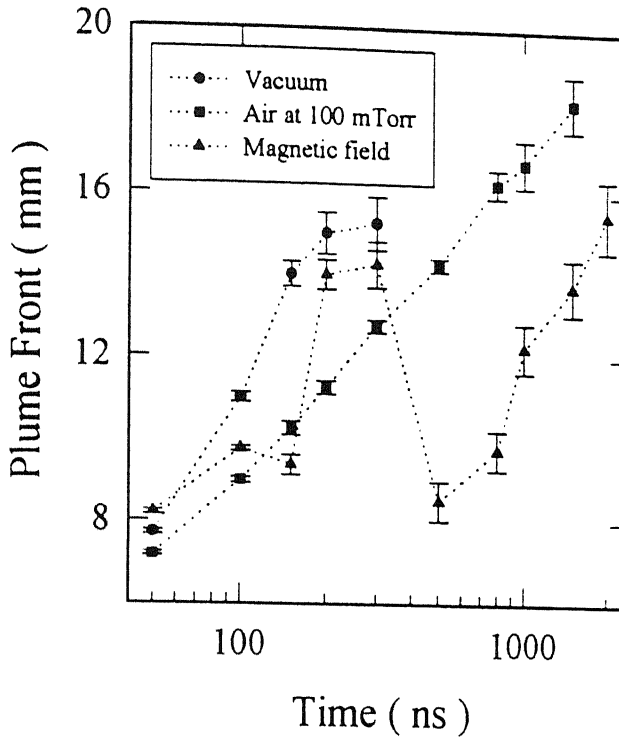


Figure 5.2: The variation of the plume front with time in vacuum, air at 100 mTorr and magnetic field. The dotted lines connecting the points are only an aid to the eye.

is plotted as a function of time in Fig.5.2. The volume of the expanding plasma plume for three different conditions is shown in Fig.5.3. The error in these quantities mainly originate from the error in determining the exact location of the plasma boundary.

The shape of the plume in vacuum is spherical throughout. The plume expansion is highly forward directed in this case. The plume appears very much diffused after 500 ns with 20 ns exposure time as shown in Fig.5.1(a). At 100 mTorr air, the shape of the plasma plume remains semispherical but the expansion of the plume gets highly reduced due to larger thrust from all sides as shown in Fig.5.1(b). The temporal behavior of plasma plume in the presence of nonuniform magnetic field in vacuum is shown in Fig.5.1(c). The size of the plasma as it propagates shows alternate contraction and expansion due to which the temporal behavior of the plasma front shows oscillations as shown in Fig.5.2. The first compression is seen at 150 nsec and the second at 500 nsec, Fig.5.1(c). To understand alternate contraction and expansion consider Eqn.(5.16). If we neglect resistive effects and assume that at early time  $\frac{\tilde{M}}{2} v_0^2 \ll \frac{3}{2} (N_e + N_i) k_B T_0$  and  $r_b \gg r_0$ , we get

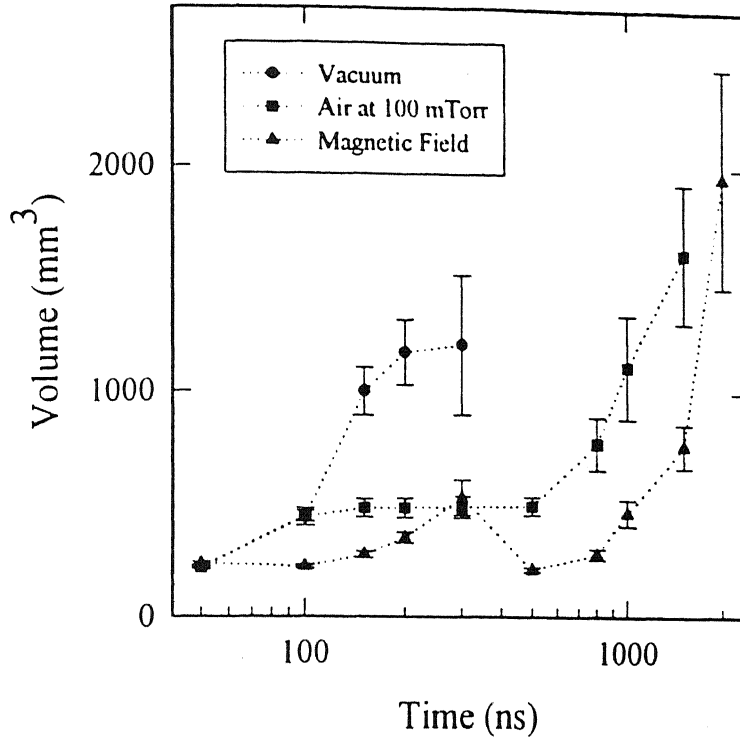


Figure 5.3: Temporal variation of the volume of the plasma plume in vacuum, air at 100 mTorr and magnetic field. The lines connecting the points are only an aid to the eye.

$$r_b \approx \left( \frac{9Nk_B T_0}{2B^2} \right)^{\frac{1}{3}} \quad (5.31)$$

The period of oscillation being given by

$$\tau \simeq \frac{r_b}{v}. \quad (5.32)$$

where  $v$  is the velocity of the plasma front. In order to calculate  $r_b$  and  $\tau$  [Eqn.(5.34) and Eqn.(5.35)], it is assumed that  $T_0$  during initial expansion is not influenced by the magnetic field [118, 203] and hence

$$T_0 \leq \frac{\bar{M}_i v^2}{5(z+1)} \quad (5.33)$$

where  $\bar{M}_i = 12 \times 1.67 \times 10^{-27}$  kg,  $v = 1.1 \times 10^5$  m/sec is asymptotic plasma expansion velocity measured from the ICCD photographs, taking  $z = 2$ ,  $T_0$  is estimated to be 101 eV from Eq(36). Taking  $N = 5.48 \times 10^{16}$  (calculated from the ICCD photographs) and  $B = 3$  kG we get  $r_b \approx 1.64$  cm and  $\tau = 0.04 \mu$  sec. From Fig.5.2 which shows the variation

of position of the plume front at various time, we find  $r_b$  to be 0.43 cm and  $\tau$  to be 150 ns, different from those calculated using Eqn.(5.31) and Eqn.(5.32). The radius of the second bounce is smaller [ Fig.5.1, Fig.5.2 ] and the time period larger. The decrease in bounce-radius with time in our case may be due to the energy loss from the plasmoid due to Bremsstrahlung radiation which is quite high in the early phase of expansion and it dominates over the resistive terms. This effect is not accounted for in Eqn.(5.16). Secondly, magnetohydrodynamic instabilities such as Rayleigh-Taylor instability which damps the plasma motion are also not considered in the equations of the plasma dynamics.

It is observed in Fig.5.1(d) that at delay times greater than 800 ns, the plasma moves towards one of the poles. The ICCD photographs of the plasma taken at a delay of 1000 ns when the target is in the middle and shifted towards the upper pole of the magnet is given in Fig.5.4. It is clear from the photographs that at a later time, the plume breaks into two lobes which move towards the poles. Figure 5.1(d) corresponds to the target position 3 mm nearer to the lower pole. When the target position is in between the poles, the lobes are symmetric, otherwise asymmetric. The above fact can be explained using magnetohydrodynamic model.

The generalised form of Ohm's law in a magnetoionic fluid is given by [6]

$$\mathbf{E} + \mathbf{v} \times \mathbf{B} = \mathbf{J}/\sigma_0 + (\mathbf{J} \times \mathbf{B})/n_e e \quad (5.34)$$

where  $\mathbf{E}$ ,  $\mathbf{B}$ ,  $\mathbf{J}$ ,  $\sigma_0$ ,  $n_e$ , and  $\mathbf{v}$  have usual meaning defined earlier. In an one dimensional flow, in the absence of conduction currents  $E_y = v_x B_z$ . As the plasma plume expands in transverse magnetic field, the ions and electrons get separated due to Lorentz force till the magnetic force acting on the charged particles equals the electric force. The plasma moves across crossed electric and magnetic field with a drift velocity given by

$$\mathbf{v} = \frac{\mathbf{E} \times \mathbf{B}}{B^2} \quad (5.35)$$

On account of three dimensional expansion of the plume, the induced electric field transverse to the flow will vary over the plume cross section because  $v_x$  decreases at larger angles. The field gradient in the plume boundary allows the closed current paths to form.

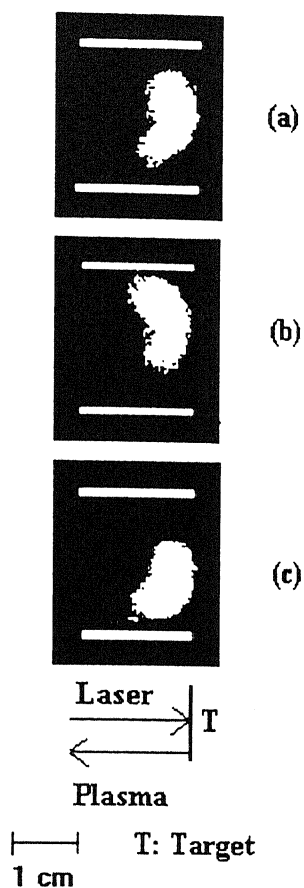


Figure 5.4: The expansion of the plasma in three different positions of the target at 1000 ns delay with respect to the ablating laser pulse. (a) Target is at the middle of the poles; (b) the target is few mms towards the upper pole of the magnet; (c) target is more towards the lower pole.

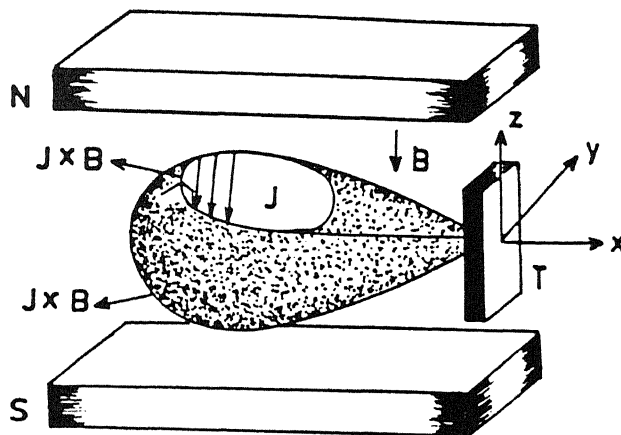


Figure 5.5: A cross sectional area of the plume showing the direction of current within and at the boundary. The  $\mathbf{J} \times \mathbf{B}$  force at the boundary accelerates the plume boundary giving rise to lobes which move towards the poles.

The current which flows inside the plume interacts with the magnetic field giving rise to  $\mathbf{J} \times \mathbf{B}$  term which decelerates the flow. Outer regions of the plume would likewise be expected to accelerate as return current flows in the opposite direction leading to  $-\mathbf{J} \times \mathbf{B}$  term. This  $\mathbf{J} \times \mathbf{B}$  term increases with increase in  $\mathbf{B}$  with larger  $Z$  (towards the poles in Fig.5.5) so the plume is observed to break into two lobes which move towards higher magnetic field side. The flow of induced current and formation of lobes is schematically shown in Fig.5.5.

The experiment is also done in magnetic field at 5 mTorr and 100 mTorr air pressure. In both the cases an increase in intensity is observed in addition to the features observed without the magnetic field.

The velocity profile of the plasma front in vacuum, 100 mTorr air and magnetic field is shown in Fig.5.6. The plume expansion is highly forward directed in case of vacuum with leading edge moving with velocity of  $1.1 \times 10^7$  cm/sec at 29 ns after the ablating laser pulse. The expansion velocity is highest in vacuum followed by air at 100 mTorr and magnetic field. Oscillations are observed in case of magnetic field due to alternate

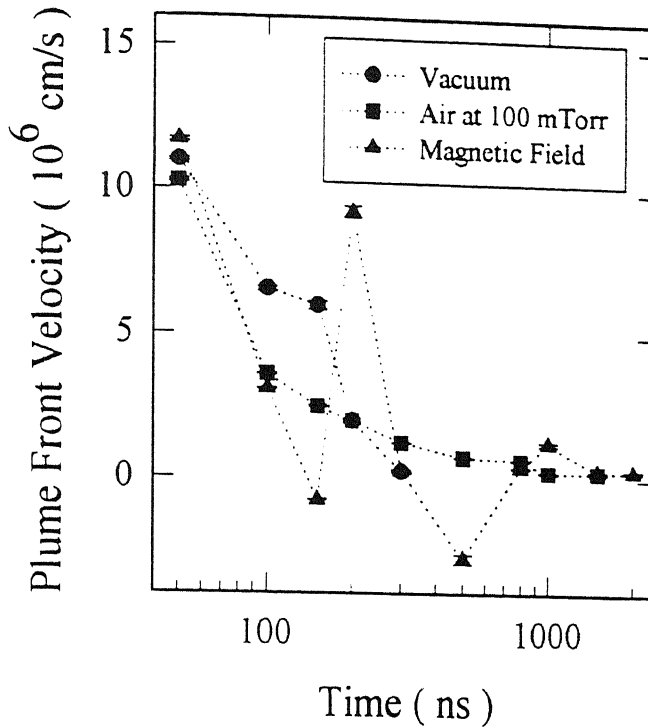


Figure 5.6: The velocity of the plume front with time.

contraction and expansion as discussed earlier. Velocity in magnetic field is minimum at 150 nsec and 500 nsec when the radius of the plasmoid is lowest.

Variation of mean and maximum intensity of the luminous plume is shown as a function of time in Fig.5.7 (a) and (b). The temporal behavior of  $I_{mean}$  and  $I_{max}$  are similar. The intensity in case of 100 mTorr air is highest followed by magnetic field and vacuum. In case of magnetic field a sudden rise in intensity is seen at the bounce points (150 ns, 500 ns) because of contraction of the plasmoid. At 900 nsec an increase in emission intensity is observed but no contraction is observed. The small fluctuations in intensity for the case of magnetic field in the interval 300-1200 nsec is shown in the inset of Fig.5.7 (b).

The ICCD images were used to estimate the electron density and temperature of the plasma. Referring to hydrodynamic Eqn.(1.11, 1.16) before and after the termination of the laser pulse, we find that after the termination of laser pulse, expansion in the direction of propagation that is in X direction, is well beyond the expansion in Y and Z direction. Since the laser pulse is Gaussian, the expansion in Y and Z direction can be taken as

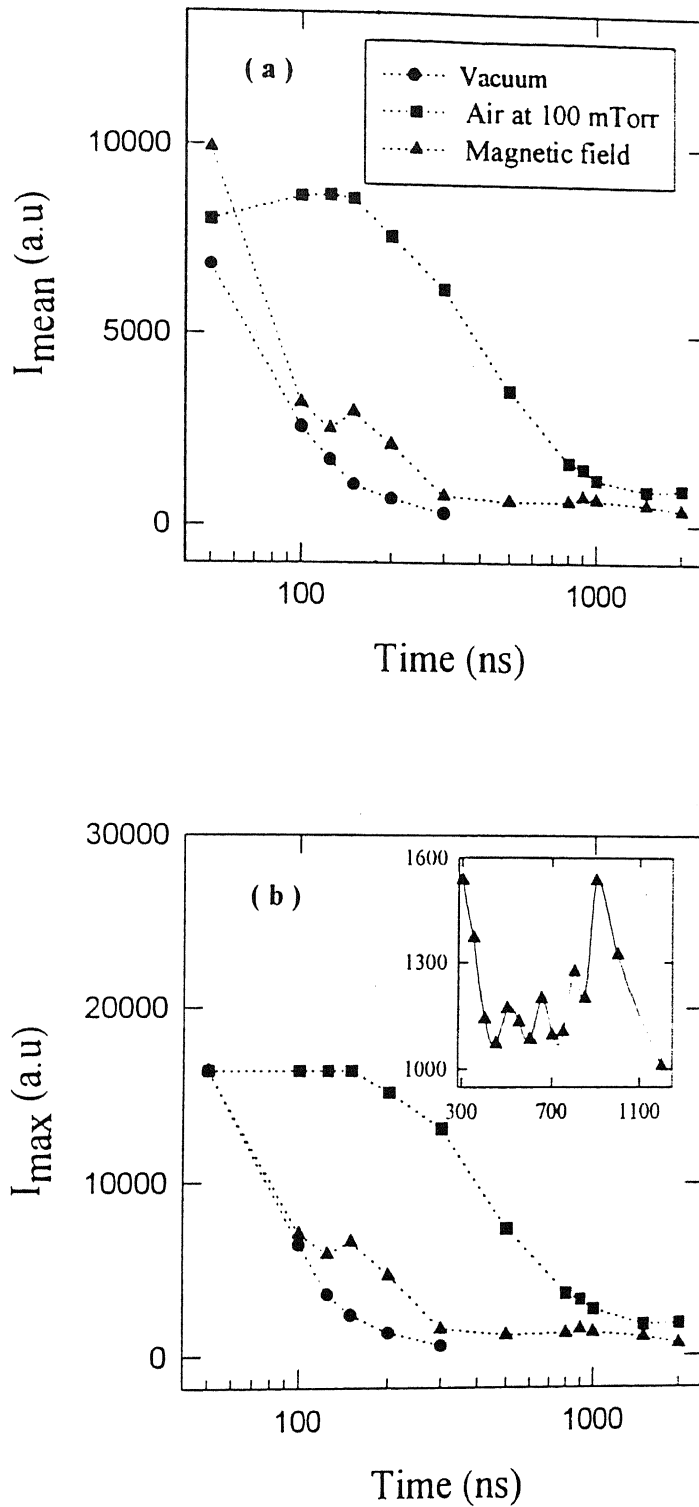


Figure 5.7: The temporal behavior of maximum and mean intensity of ICCD photographs. The inset in fig. (b) shows expanded version of the variation of intensity in case of magnetic field.



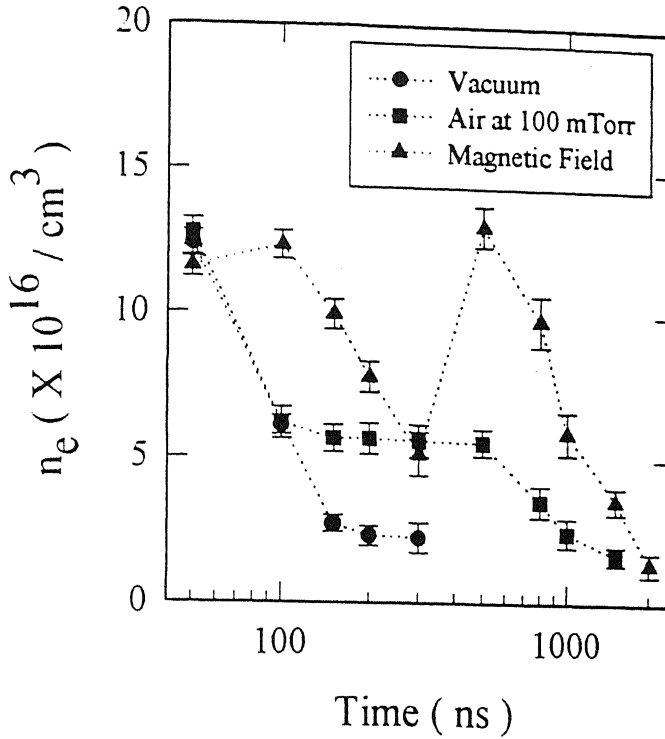


Figure 5.8: The temporal variation of electron density calculated from the ICCD photographs.

symmetric. From mass continuity equation it follows,

$$\rho(t_0)V(t_0) = \rho(t)V(t) \quad (5.36)$$

Here  $\rho$  is the ion density,  $V$ , the volume of the plasmoid,  $t_0$  ( $< t$ ) refers to time for the photograph taken at the earliest time and  $t$  is any later time. Electron density at an early time is calculated theoretically assuming adiabatic expansion [107] and volume at early time is calculated from the photographs. Thus knowing the volume of the plume at any time (from the photographs), electron density can be estimated. Figure 5.8. shows the temporal behavior of calculated electron density. The temporal behavior shows that electron density is highest in the presence of magnetic field followed by air and vacuum. Further, it shows oscillatory behavior in magnetic field due to contraction and expansion of the plasmoid.

The temperature of the plasma was also calculated from ICCD photographs. Since the temperature is high it is assumed that the plasma acts like an assembly of black body

radiators and the emission is mostly in the visible region (due to high temperature, Wien's displacement law). According to Stefans' law, the power radiated ( $P_r$ ) by a black body is

$$\sigma T^4 S = P_r \propto \text{total intensity observed in the photographs } (I_r)$$

Thus at  $t$  and  $t_0$  one can write

$$\sigma T^4(t) S(t) = K_1 I_T(t), \quad t > t_0. \quad (5.37)$$

$$\sigma T^4(t_0) S(t_0) = K_1 I_T(t_0), \quad t = t_0 \quad (5.38)$$

Here,  $S$  is the total surface area and  $K_1$ , the proportionality constant. The temperature at early time is calculated theoretically assuming adiabatic spherical expansion at early time [107] and area is calculated from the photographs. Comparing Eqn.(5.37) and Eqn.(5.38), it follows

$$\frac{T^4(t) S(t)}{I_T(t)} = \frac{T^4(t_0) S(t_0)}{I_T(t_0)} \quad (5.39)$$

Calculating the surface area at various times from the photographs, the temperature was calculated and is shown in Fig.5.9. It is found that the temperature in 100 mTorr air is highest followed by magnetic field and vacuum. A slight increase in temperature in magnetic field is observed at the second bounce point (500 ns). Increase in temperature in gas is caused due to enhanced interparticle collisions due to compression from the outside. In case of magnetic field, surface currents are set up due to finite resistivity at the plasma field boundary producing increased temperature on account of ohmic heating. The extra energy due to ohmic heating comes from the plume kinetic energy.

Assuming adiabatic expansion of the plasma plume after the termination of laser pulse, the theoretical calculations show that electron density and electron temperature in vacuum vary with time as  $n_e \propto t^{-3}$  and  $T_e \propto t^{-2}$  [107]. We have fitted the equation,  $y = b_0 t^p$  with the calculated values of electron density and electron temperature for the vacuum case as

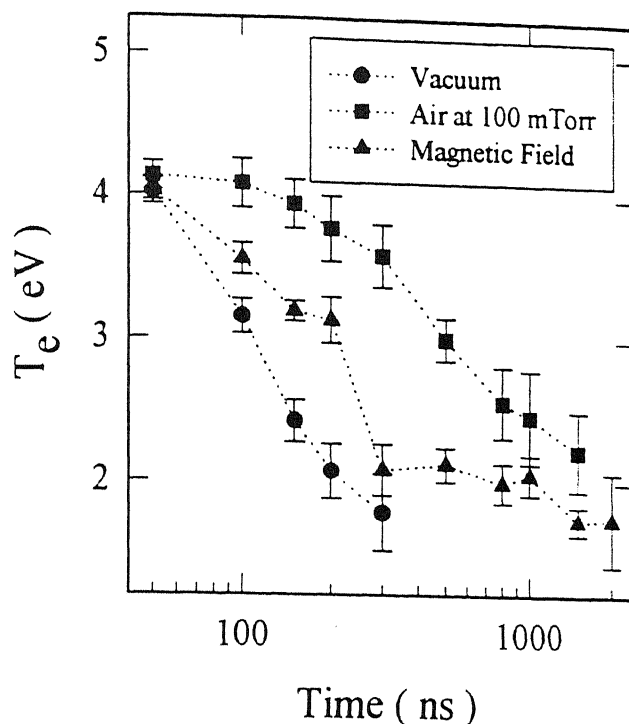


Figure 5.9: The temporal behavior of electron temperature calculated from the ICCD photographs.

shown in Fig.5.10. The value of  $p$  comes out to be -2.85 and -2.73 close to the theoretical value of -3 and -2 for the electron density and electron temperature respectively.

### 5.4.2 Time Resolved Emission Spectroscopy

The emission spectra of carbon plasma were recorded at different distances away and parallel to the target surface by moving the monochromator in a plane perpendicular to the target surface. The temporal profiles of CI transition  $2p^3\ ^3D^0 - 8f\ F(5/2)$  at 399.7 nm, CII transition  $3d\ ^2D - 4f\ ^2F^0$  at 426.7 nm, CIII transition  $3s\ ^3S - 3p\ ^3P^0$  at 465.0 nm and CIV transition  $3s\ ^2S - 3p\ ^2P^0$  at 580.1 nm were recorded at different distances away and parallel to the target surface in vacuum ( $P = 0.1\ \text{mTorr}$ ), with and without magnetic field. The emission lines were identified using the information available in the literature [186].

In the absence of magnetic field the temporal profile of all the species showed a single peak structure as shown in the inset of Fig.5.11 - 5.14. In the present case, the plasma moved in a non-uniform magnetic field as shown in the inset of Fig.2.1. (Chapter 2). Along

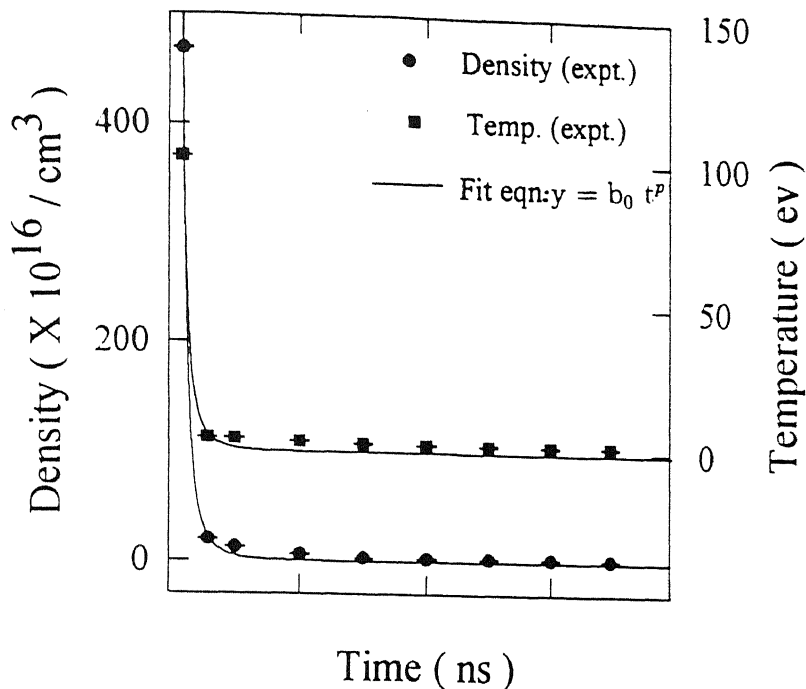


Figure 5.10: The  $n_e$  and  $T_e$  of the plasmoid expanding in vacuum, calculated from ICCD photographs has been fitted with equation of the form,  $y = b_0 t^p$ .

Z direction, the field was maximum at the poles and minimum in the middle. The single plume was observed to break into two symmetric lobes (say lobe 1 or L1 and lobe 2 or L2), one towards the north pole and other towards the south pole as shown in Fig.5.15(a). However, it was very difficult to analyze the different components (fast/slow), arising from each of these lobes spectroscopically because the two lobes (L1, L2) being symmetric, fall on the same line on the detector. To see the effect, the target was kept off centered such that the laser was focused nearer ( $\sim 3$  mm) to one of the poles than the other which gave rise to asymmetric lobes, L1 and L2, L1 being larger than L2. Figure 5.15 (a) and (b) (at the left) show the observed plume at 1000 ns with target kept at the centre and off centred with respect to the poles respectively. The Fig.5.15(c) and (d) give a pictorial representation.

The temporal profiles of CII and CIV ions which are at the front of the plasma plume show interesting features at a distance of 6 mm onwards from the target surface. Similar

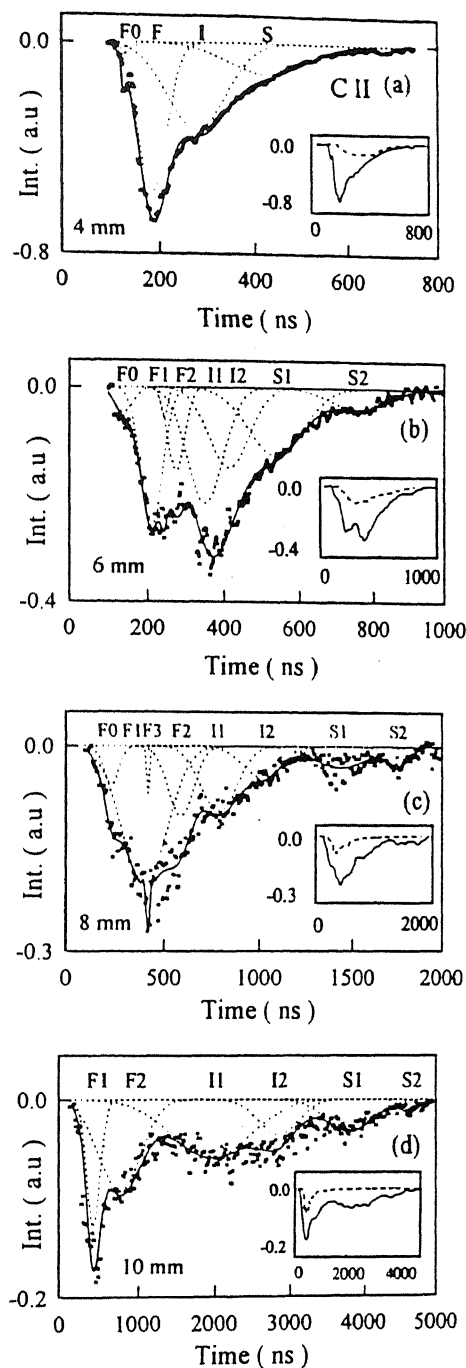


Figure 5.11: Time resolved emission spectra of CII species in vacuum with magnetic field at (a) 4 mm, (b) 6 mm, (c) 8 mm and (d) 10 mm respectively along with the best fitted curve (solid line) and the fitting Gaussian functions (dotted lines). In the inset the dotted line represents the emission spectra without magnetic field and solid line represents FFT smoothed spectra of the magnetic field case.

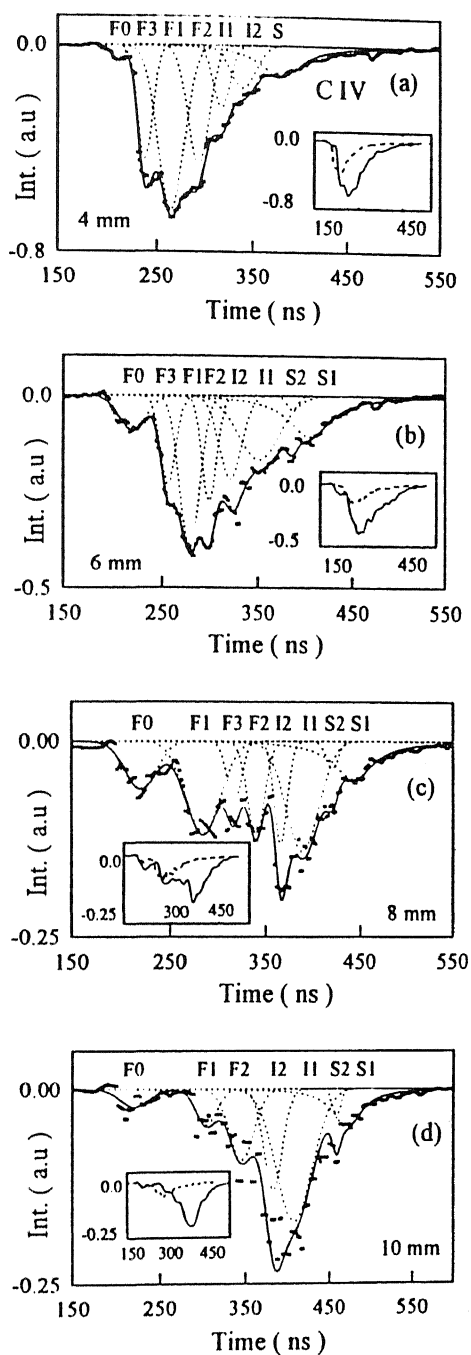


Figure 5.12: Time resolved emission spectra of CIV species in vacuum with magnetic field at (a) 4 mm, (b) 6 mm, (c) 8 mm and (d) 10 mm respectively along with the best fitted curve (solid line) and the fitting Gaussian functions (dotted lines). In the inset the dotted line represents the emission spectra without magnetic field and solid line represents FFT smoothed spectra of the magnetic field case.

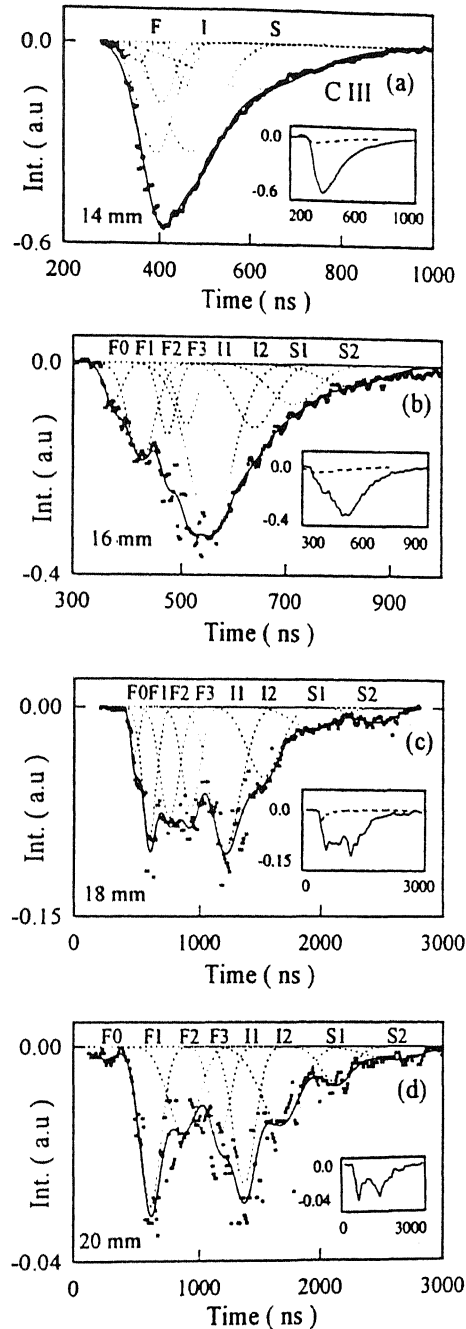


Figure 5.13: Time resolved emission spectra of CIII species in vacuum with magnetic field at (a) 14 mm, (b) 16 mm, (c) 18 mm and (d) 20 mm respectively along with the best fitted curve (solid line) and the fitting Gaussian functions (dotted lines). In the inset the dotted line represents the emission spectra without magnetic field and solid line represents FFT smoothed spectra of the magnetic field case.

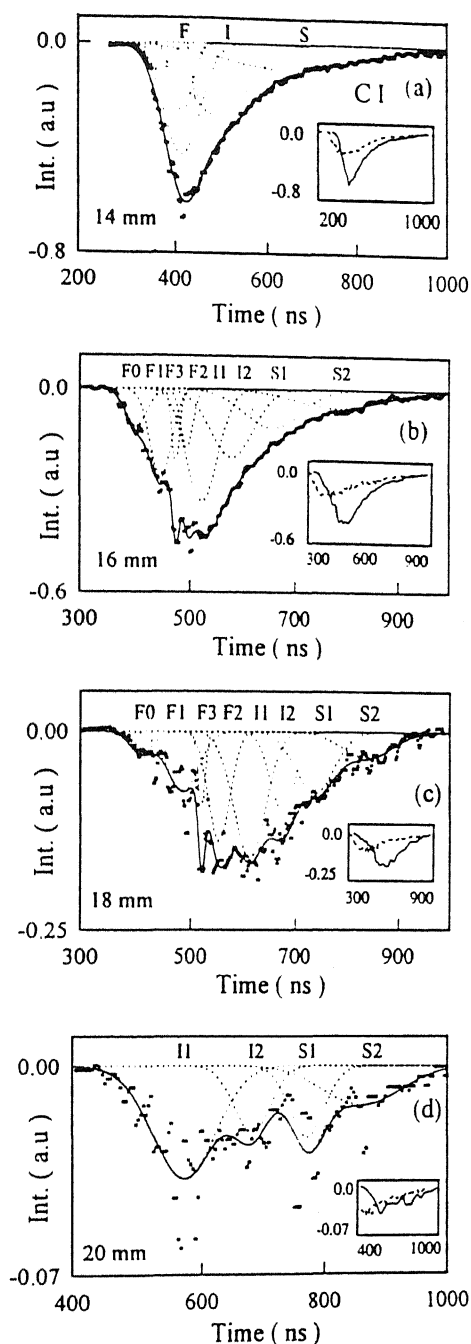


Figure 5.14: Time resolved emission spectra of CI species in vacuum with magnetic field at (a) 14 mm, (b) 16 mm, (c) 18 mm and (d) 20 mm respectively along with the best fitted curve (solid line) and the fitting Gaussian functions (dotted lines). In the inset the dotted line represents the emission spectra without magnetic field and solid line represents FFT smoothed spectra of the magnetic field case.



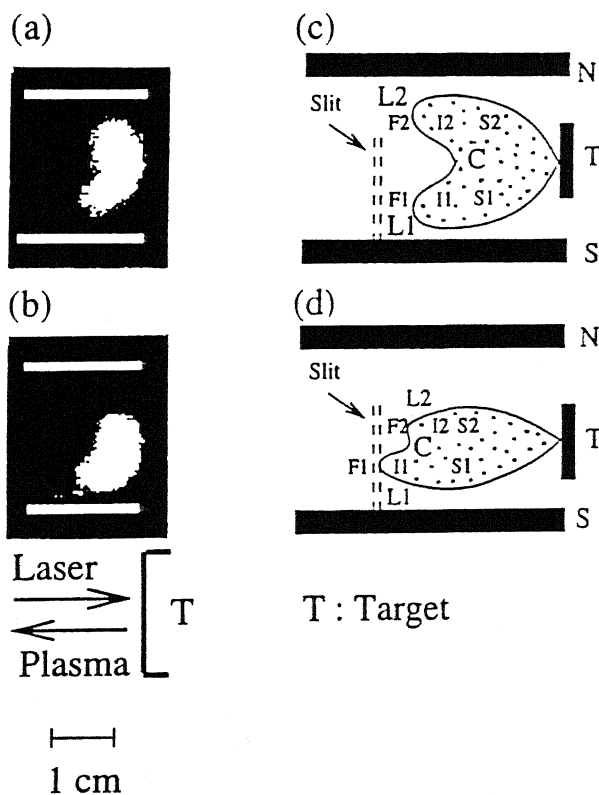


Figure 5.15: (a) ICCD images of the plume breaking into two symmetric lobes (at 1000 ns) when focal spot is exactly between the two poles. (b) Plume breaking into two asymmetric lobes (at 1000 ns) when focal spot is nearer to one of the poles. (c) Pictorial representation of (a). (d) Pictorial representation of (b). L1, L2, C refers to lobe 1, lobe 2 and central lobe. F1/(F2), I1/(I2), S1/(S2), refers to fast, intermediate and slow components of lobe 1 and lobe 2 respectively.

features are also observed in CIII and CI at 16 mm and onwards. The time resolved spectra of CII, CIV, CIII and CI ions along with the best fitted curve at different distances in the direction of propagation of the plasma plume are shown in Fig.5.11 - 5.14. respectively. It has been found that Gaussian function fits best with the different peaks observed in the spectra. The best fitted curve (solid line) (minimum standard fit error of around 0.01) is the resultant of individual Gaussian curves (dotted line) shown in the figure. The significance of fitting the main spectra with these individual curves lies in the fact that the peak position of these individual curves help locate the less prominent peaks in the original spectra in addition to the prominent ones. It also helps understand their evolution with time and distance. Figure 5.11 shows time resolved spectra of CII at 4 mm and onwards up to 10 mm along with the best fitted curve. In the inset the solid line shows the smoothed curve by fast fourier transform (FFT) filtering, and dotted line shows the temporal profile in vacuum without magnetic field plotted on the same scale as that of magnetic field for comparison. It shows that intensity of the spectra increases in presence of magnetic field. After 10 mm, the intensity of all the peaks decreases till 14 mm beyond which signal is too weak to be recorded. The spectrum of CIV from 4 mm onwards is shown in Fig.5.12. The spectrum of CIV like that of CII could be recorded till 14 mm. The spectrum of CIII at different distances is shown in Fig.5.13. Till 14 mm, only one single peak is observed which can be fitted by 3 Gaussian functions like that of CII at 4 mm. At 16 mm that is just after the disappearance of CII and CIV, CIII shows small peaks in addition to the main peak. The case is very much similar to that of CII and CIV. The spectrum of CI shown in Fig.5.14 resembles CIII very closely.

The velocity of the carbon species is calculated from the delay of the peak of the emission spectra at different distances with respect to the trigger pulse. The velocity of the carbon species with and without magnetic field at a distance of 4 mm from the target is shown in table 5.1. In magnetic field, velocity of CII species is highest followed by CIV, CIII and CI species.

In addition to the multiple peak structure, another interesting feature observed is the

Table 5.1: Velocity of carbon species with and without magnetic field in vacuum.

Species	Velocity ( $10^6$ cm/sec)	
	B absent	B present
CI	1.58	1.54
CII	1.24	2.50
CIII	1.76	1.68
CIV	1.90	1.69

oscillations in the temporal profile of CII and CIV at distance of 6 mm to 14 mm away from the target and at 16 mm to 20 mm for CIII and CI respectively. Since these oscillations are observed for the species at the outermost boundary they can be attributed due to edge oscillations in magnetic field.

The formation of multiple peaks can be explained using magnetohydrodynamics model as discussed earlier in section 5.41 [Eqn. (5.34)] On account of three dimensional expansion of the plume the induced electric field transverse to the flow will vary over the plume cross section because  $v_x$  decreases at larger angles. Field gradient will exist in the plume boundary permitting closed current paths to form. The current which flows inside the plume interacts with the magnetic field giving rise to  $\mathbf{J} \times \mathbf{B}$  term which decelerates the flow. This gives rise to slow component (S) in the plasma plume. In the outermost boundary, the electrons flow in the opposite direction giving rise to  $-\mathbf{J} \times \mathbf{B}$  term which accelerates the outermost boundary [30] giving rise to fast component (F) in plasma plume. The region lying in between fast and slow component forms the intermediate component (I). It is schematically shown in Fig.5.16.

Multiple peak formation in the emission spectra is due to two lobes, L1 and L2, which move towards the poles and the central lobe. Each lobe has three components viz. the fast, the intermediate and the slow one. In Fig.5.11 at 4 mm from the target, other than the first small peak F0, there is only one distinct peak which can be best fitted (least standard fit error of around 0.01) by three Gaussian peaks shown as F (fast), I (intermediate) and S (slow). The small peak F0 is the one also observed without the magnetic field. On going

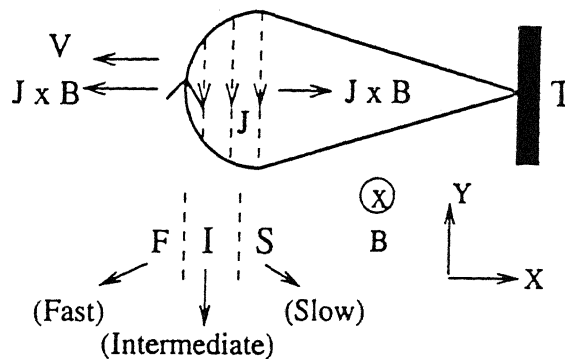


Figure 5.16: Schematic diagram of the direction of current density  $J$  giving rise to fast, intermediate and slow component.

from 4 mm to 10 mm, it is observed that the fast peak (F) breaks into three distinct peaks (F1, F2, F3), the intermediate (I) and slow peak (S) break into two distinct peaks (I1, I2) and (S1, S2) respectively. F1, I1, S1 are the fast, intermediate and slow components coming from L1 whereas F2, I2, S2 are due to L2. F3 is the fast peak due to central lobe. The intermediate and slow peaks of central lobe are not resolved. The situation is schematically depicted in Fig.5.16. In general we observe

- (1) Peaks due to L1 are of higher intensity than the corresponding peaks from L2 i.e. intensity of  $F1 > F2$ ,  $I1 > I2$  and  $S1 > S2$ . This is because intensity of L1 is higher than that of L2. (Fig.5.15(b)).
- (2) The intensity of the fast peak F3 due to central lobe is of lower intensity than  $F1/(F2)$  and the intensity decreases faster compared to  $F1/(F2)$ . This is because central lobe disintegrates into L1 and L2 with increasing distance.

Intensity and velocity are calculated for all the peaks of each of these species and their nature is studied. The velocity of the fast peaks for CII (Fig.5.11), CIII (Fig.5.13) and CI (Fig.5.14) increases with distance whereas for other peaks, it decreases with distance. For CIV species velocity increases for all the components but it is highest for the fast

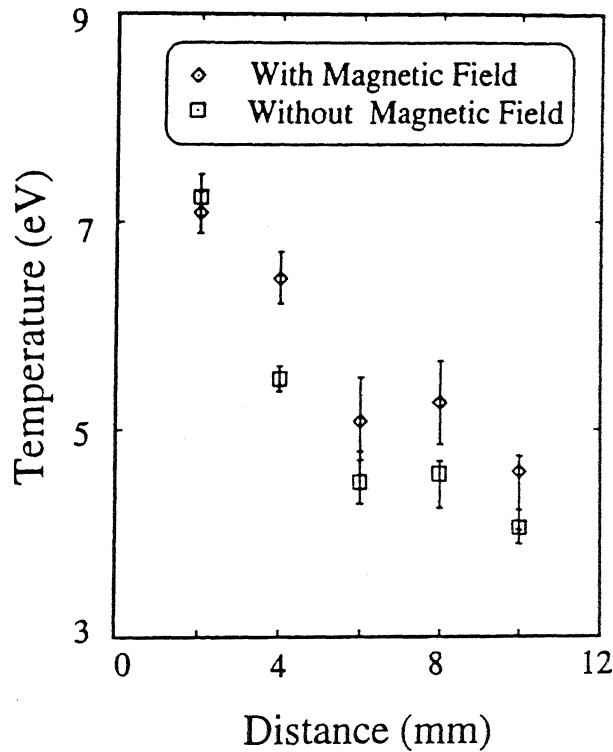


Figure 5.17: Variation of electron temperature with distance with and without magnetic field.

components followed by intermediate and slow components.

The effect of magnetic field on CIII and CI species is conspicuous only after the disappearance of CII and CIV species after 14 mm when CIII and CI species are at the outermost boundary. In both CIII ( Fig.5.13) and CI (Fig.5.14) till 14 mm, only one peak is observed in the signal which can be best fitted by three Gaussian peaks. However, 16 mm onwards, multiple peaks are observed in CIII and CI, similar to that of CII at earlier distances. Beyond 20 mm, the spectrum of CIII and CI could not be recorded.

The increase in intensity of the temporal profile of all these species ( CI, CII, CIII and CIV) in magnetic field is due to higher temperature and density of the plasma in magnetic field. The temperature profile of plasma with and without magnetic field is shown in Fig.5.17. The temperature of the plasma was experimentally determined at various distances using relative line intensities of the species having same ionization state assuming the plasma to be in local thermodynamic equilibrium. The temperature of the plasma is found to be higher in magnetic field case. The increase in electron temperature

may be due to joule heating and electromagnetic compression of the plasma. The density can be estimated from model of mass ablation rates [133], that is  $dm/dt \propto I_L^{0.6}$ . Since the velocity of the bulk of the plasma decreases in magnetic field, the density increases in magnetic field compared to no magnetic field case. The electron density at 4 mm from the target is estimated to be  $1.18 \times 10^{17} / \text{cm}^3$  without magnetic field compared to  $1.24 \times 10^{17} / \text{cm}^3$  in magnetic field. Increase in density in magnetic field has been reported earlier [177]

The temporal variation of density and temperature as shown in Fig.(5.8, 5.9) shows rise in both density and temperature in magnetic field.

Oscillations are observed in the temporal profile of CII and CIV from 6 mm and onwards (Fig.5.11 - 5.12); in CIII and CI from 16 mm and onwards (Fig.5.13 - 5.14). These oscillations are not observed without magnetic field. Since the oscillations are observed for species when they are at the outermost front, they are attributed due to edge instability in magnetic field. These edge oscillations are similar to that observed by Kent *et al* [136] in a transverse magnetic field of 4.4 kG using langmuir probe.

### 5.4.3 Time Integrated Emission

Time integrated spectra of carbon plasma is recorded at various distances from the target surface kept at positions marked as P, Q, R respectively between the poles, as shown in Fig.5.18. The position of these points and the respective magnetic fields at these points is also shown in the figure. Figure 5.19 shows the time integrated spectra of carbon plasma recorded at 6 mm (P'/ Q'/ R') from the target position (P/ Q/ R) respectively in the spectral range 350 nm to 600 nm, thus the spectra recorded at position P' correspond to target position at P (Fig.5.18) and similarly for other cases. The spectra without magnetic field are also shown in Fig.5.19(d) for comparison. The wavelength and the corresponding excited ionic states observed are shown in the figure. The emission lines are identified using the information available in the literature [184]. The characteristics of emission spectra vary considerably for the three positions in the magnetic field and that of without magnetic field. The striking differences observed in the four cases are enumerated below.

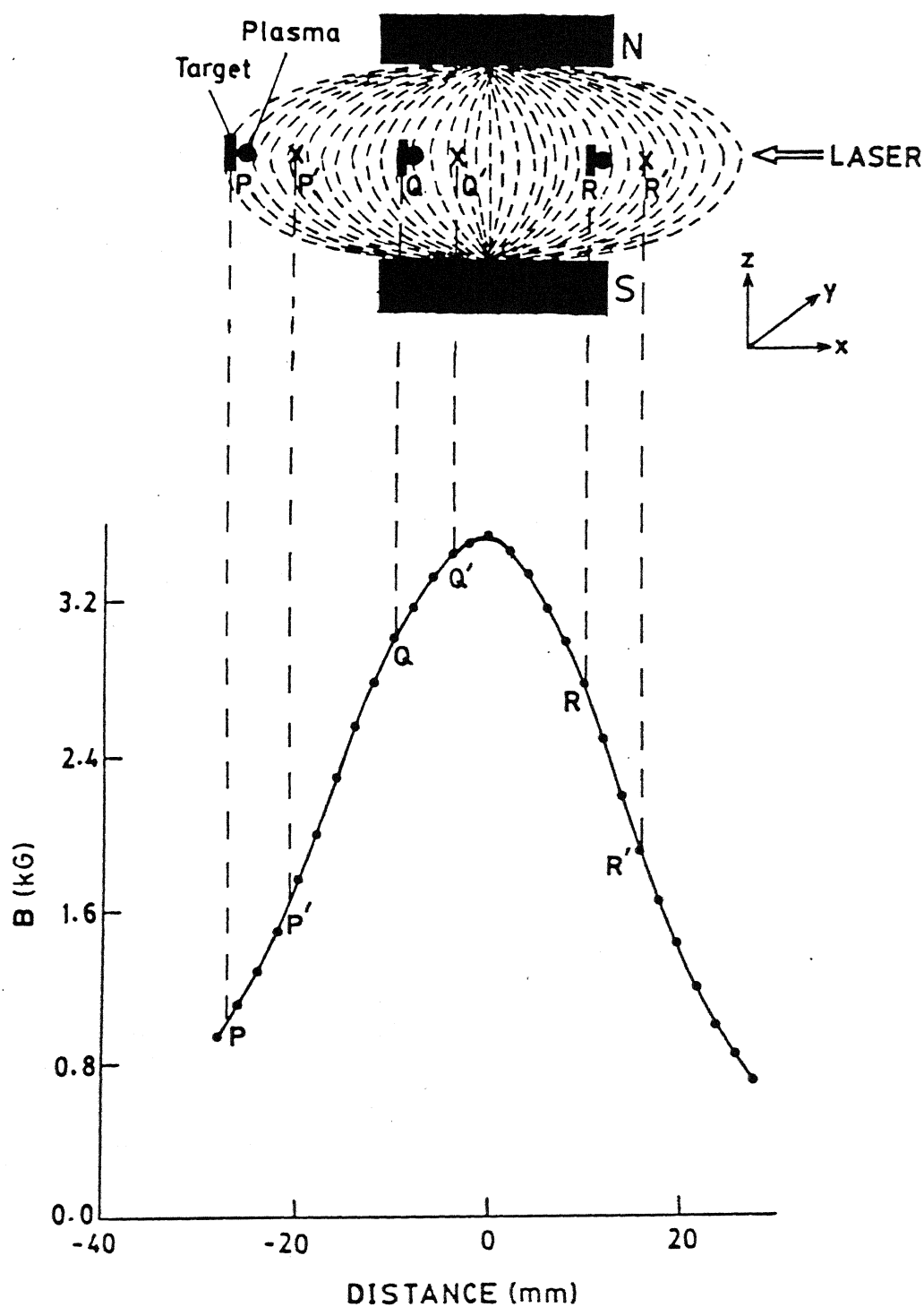


Figure 5.18: Schematic diagram of three positions of the target at P, Q and R in magnetic field. The graph below shows the magnetic field strength at those points.

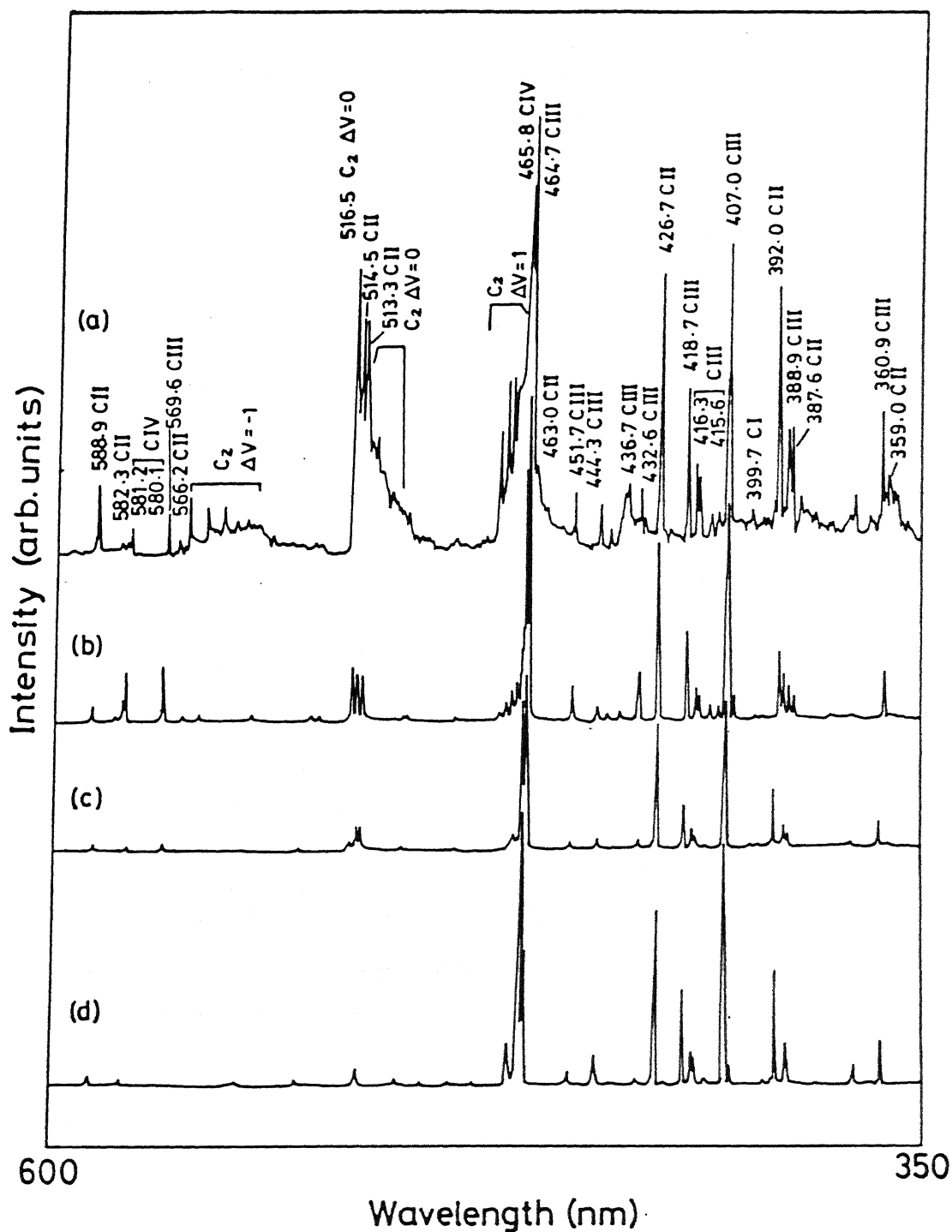


Figure 5.19: Time integrated emission spectra at three different positions in magnetic field (a) target kept at P and spectrum taken at P'; (b) target kept at Q and spectrum taken at Q'; (c) target kept at R and spectrum taken at R' and (d) B = 0 case.



The intensity of the emission lines increases in magnetic field for the position P and Q of the target compared to that of no magnetic field case. It is highest in case of position P followed by position Q of the target in magnetic field. However, the intensity of the lines in position R of the target is less than that of no magnetic field case.

The excited lines are both from neutrals and ionic species but the concentration of ionic species is more than that of the neutrals. The intensity variation of a strong line of CII (426.7 nm,  $3d^2D - 4f^2F^0$ ) and CIII (407.0 nm,  $4f^3F^0 - 5g^3G$ ) is plotted as a function of distance for all the three position of magnetic field in Fig.5.20. It follows from the figure that the intensity of the lines increases initially, attains a maximum value and then starts decreasing. The fall in intensity with distance for the spectra recorded at position P is slower than that for position R. The emission was observed as far as 30 mm from the target for position P compared to 10 mm for position R.

It is interesting to note that the intensity of  $C_2$  Swan band emission,  $d^3\pi_g - a^3\pi_u$ , with  $\Delta v = -1, 0, 1$  is much larger at the position P of the target compared to other positions as shown in Fig.5.19 and Fig.5.21. Figure 5.21 shows the band emission along with the transitions on an enlarged scale for  $\Delta v = -1, 0, 1$ . Variation of  $C_2$  band intensity (516.5 nm,  $d^3\pi_g - a^3\pi_u$ ) with distance for various positions and that without magnetic field is shown in Fig.5.22. The  $C_2$  band intensity is highest in position P followed by position Q. The vibrational temperature of  $C_2$  molecule was calculated from intensity ratio of two transitions [205] and was found to be 1.96 eV at a distance of 6 mm from position P.

The temperature of the plasma is calculated from the ratio of relative intensity of the lines of the ionic species assuming plasma to be in local thermodynamic equilibrium (LTE). For LTE to hold, the electron density must satisfy [45]

$$n_e \geq 10^{12} T_e^{1/2} (E_k - E_i)^3 \text{ cm}^{-3} \quad (5.40)$$

where  $T_e$  is in k and  $(E_k - E_i)$  in eV.

Using  $\Delta E = 2.84$  eV, corresponding to the largest energy gap of transitions used for temperature measurement and highest  $T_e$  (11.4 eV) the lower limit for  $n_e$  from above

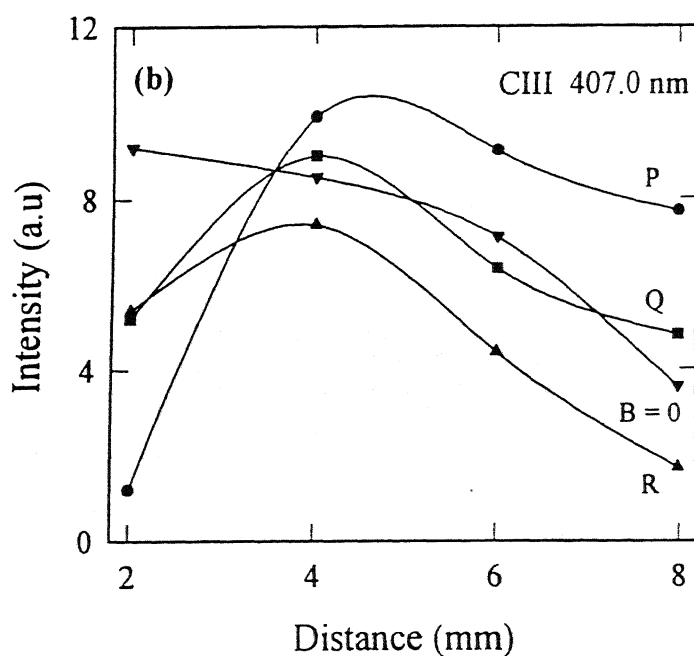
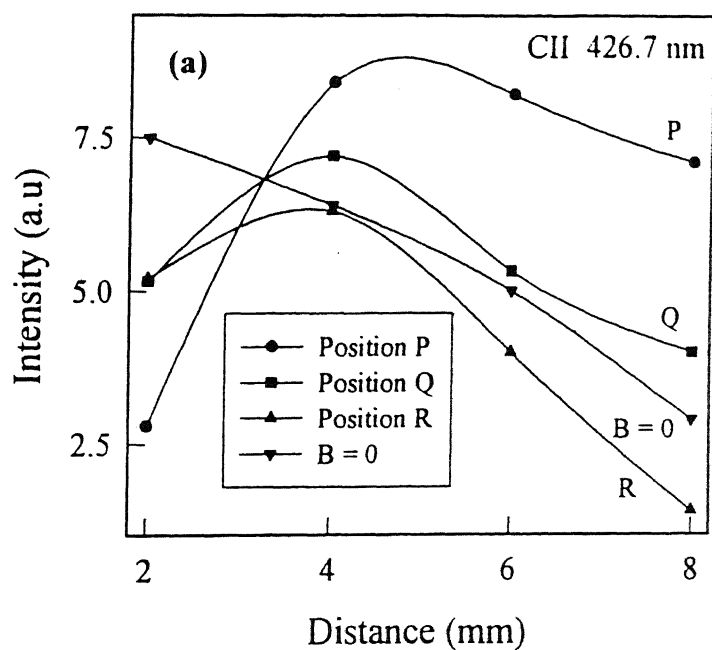


Figure 5.20: Variation of relative intensity of the lines of (a) CII (426.7 nm) and (b) CIII (407.0 nm) transition with distance when target is kept at different positions in magnetic field and without magnetic field.

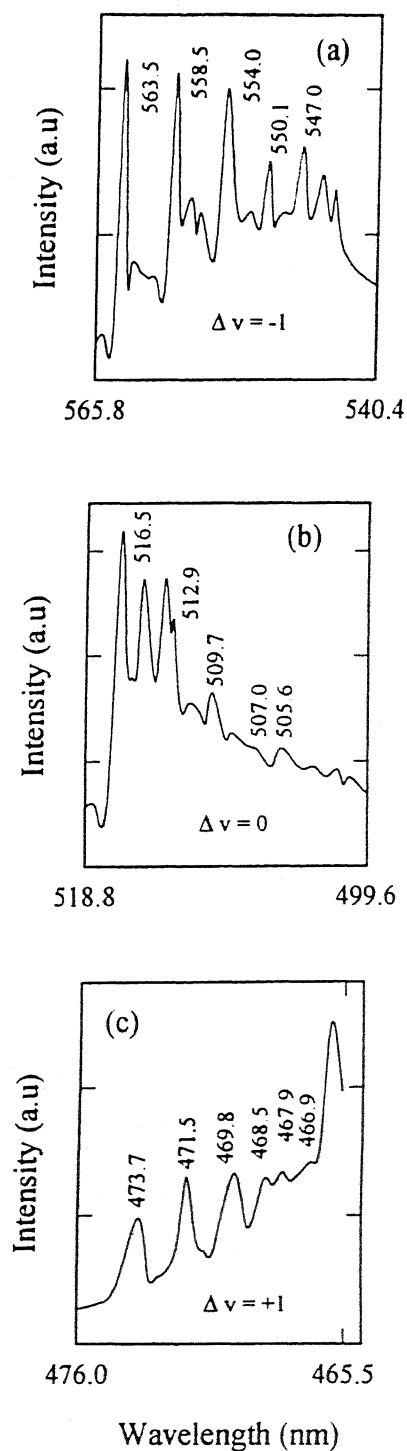


Figure 5.21: C<sub>2</sub> Swan band emission at 6 mm from the target when it is kept at position P of magnetic field. Transitions corresponding to (a)  $\Delta v = -1$ ; (b)  $\Delta v = 0$  and (c)  $\Delta v = 1$  are shown in an enlarged scale.

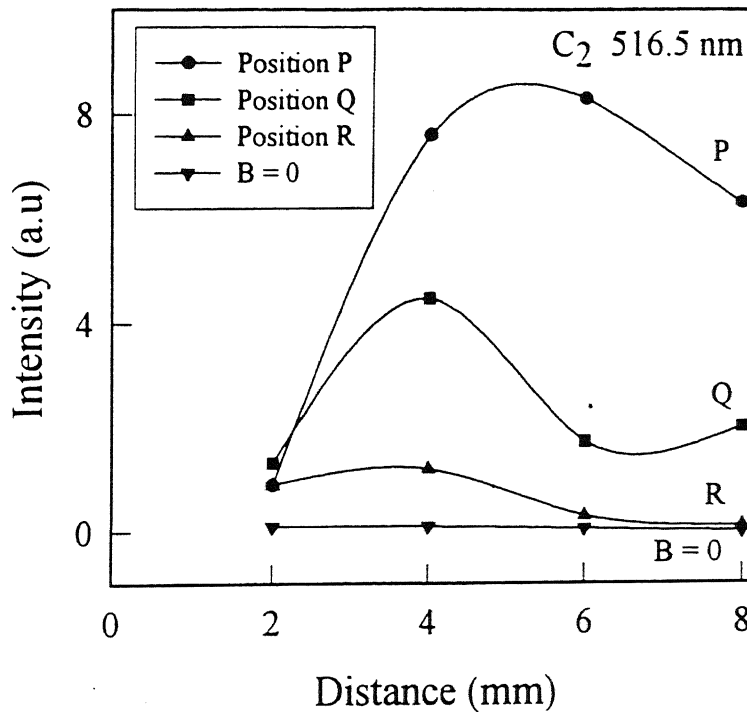


Figure 5.22: Variation of relative intensity of  $C_2$  band (516.5 nm) with distance when target is kept at different positions in magnetic field and without magnetic field.

equation comes out to be  $8.33 \times 10^{15} / \text{cm}^3$ . Our observed values of  $n_e$  calculated from the Stark broadened profile of CII transition is always greater than this limit which justifies the use of LTE approximation for our analysis. Figure 5.23 shows the spatial variation of temperature in presence and absence of magnetic field. The temperature in case of position P is found to be highest followed by position Q and R. It is estimated to be 11.4 eV, 5.10 eV and 4.34 eV at a distance of 6 mm from the target (P', Q', R') when the target position is P, Q and R of magnetic field respectively. The temperature in the absence of magnetic field at 6 mm is estimated to be 4.5 eV. Temperature is also calculated at different laser fluence in magnetic field (in position Q) and without magnetic field at a fixed distance from the target (4 mm) as shown in the Fig.5.24. It is found that temperature is higher in magnetic field and increases with increase in fluence. The estimated density using Stark broadened profile without magnetic field at 4 mm from the target is  $1.18 \times 10^{17} / \text{cm}^3$  compared to  $1.24 \times 10^{17} / \text{cm}^3$  at the same distance in the position Q of the magnetic field in agreement

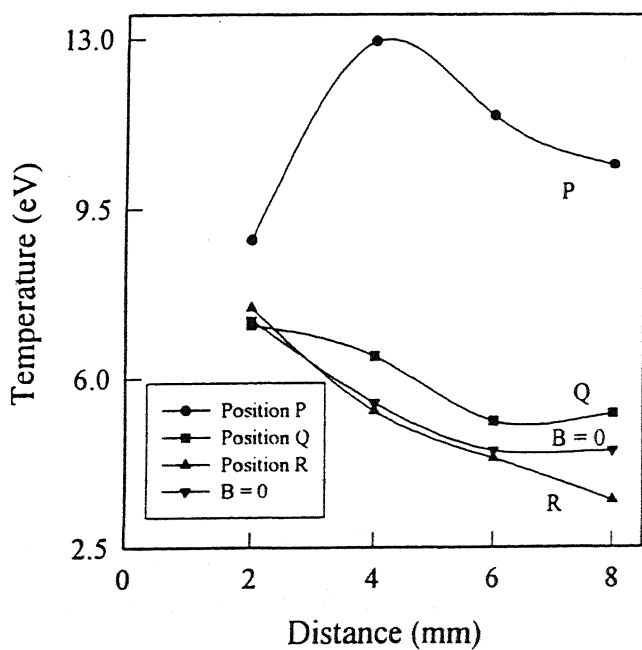


Figure 5.23: Variation of electron temperature with distance, with and without magnetic field for different positions in magnetic field calculated from relative line intensity of the same ionic species.

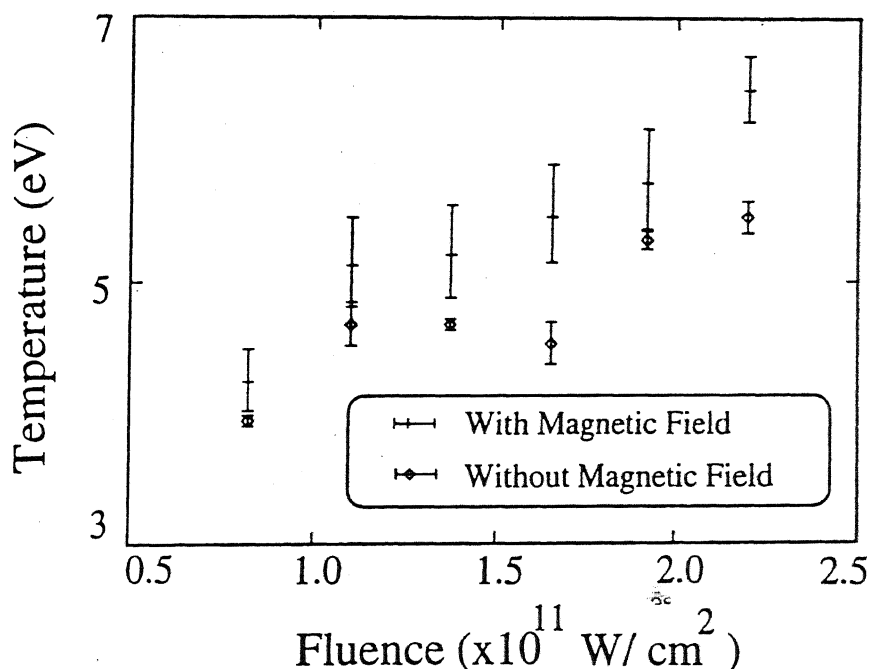


Figure 5.24: Variation of electron temperature with laser fluence with and without magnetic field at a fixed distance (4 mm) from the target surface.

with earlier report [177]. It is due to the compression of the plasma by  $\mathbf{J} \times \mathbf{B}$  force and enhanced ionization due to rise in temperature in magnetic field.

The visible observation of the colour of the luminous plume revealed that it changes from blue to green in the presence of magnetic field. The  $\text{C}_2$  emission at 516.5 nm may be responsible for this green colour in magnetic field. As is obvious from Fig.5.19 that in the absence of magnetic field, most of the strong emission lines fall in the wavelength range 360 nm to 465 nm which is violet and blue region in the electromagnetic spectrum.

It is worthwhile to mention that in case of position Q of the target, the plasma traverses a path of highest magnetic field (QQ') followed by position R and P (Fig.5.18) whereas intensity is highest in position P followed by position Q and R. This observation signifies that curvature and gradient of magnetic field is responsible for the above observations. Field lines are convex to the moving plasma with positive field gradient in position P compared to position R where field lines are concave to the moving plasma with negative

field gradient. The earlier experiment in magnetic field [144] corresponds to position Q of target in our experiment.

In order to explain the characteristic emission in magnetic field we believe the following three processes may be responsible viz,

- (1) The compression of magnetic field due to flowing plasma which is different for three positions P, Q and R.
- (2) Flow of current due to electro-magnetic interaction.
- (3) Drift of charged species due to curvature and gradient of magnetic field.

The expanding plasma has finite conductivity that can support currents, the plasma hydrodynamic motion leads to compression and distortion of the ambient magnetic field. For the plasma having high  $\beta$ , that is when the particle pressure is higher than magnetic pressure compression of field lines is more. A better way of quantifying this fact is by magnetic Reynolds number,  $R_m$  which is the ratio of magnetic field convection to magnetic field diffusion given in Eqn.(5.30).

$$R_m = \frac{vL}{n_m}$$

where  $v$  is the fluid velocity and  $L$ , the magnetic field gradient scale length and  $n_m$ , the magnetic viscosity. In our case at early time  $v \sim 10^5$  m/sec,  $L \sim 0.6$  cm and  $n_m = 1.35 \times 10^2$  m<sup>2</sup>/sec, we get  $R_m \sim 5$  which is  $>1$ , that is the flow term dominates over the diffusion term which results in compression of the magnetic field lines. Figure 5.25. schematically shows the distortion of magnetic field lines for three positions. The field lines are highly compressed at position P where radius of curvature is opposite to the moving plasma whereas they are rarefied or less compressed at position R where the field lines are along the moving plasma. Thus due to distortion of field lines the effective magnetic field becomes highest at P followed by position Q and R.

The flow of current due to electromagnetic interaction is governed by generalised form of Ohm's law in a magnetoionic fluid given by Eqn.(5.16) As the plume expands three dimensionally, electric field induced transverse to the flow vary over the plume cross

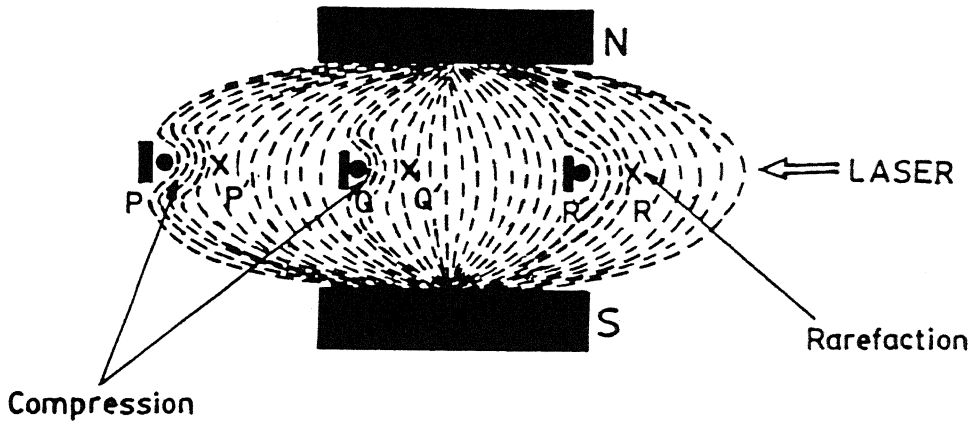


Figure 5.25: Schematic diagram of the distortion and compression of magnetic field lines when target is kept at different positions in magnetic field.

section, field gradients exist in the plume boundary and current starts to flow.

In a curved vacuum field, the drift experienced by the charged species due to curvature and gradient of magnetic field is given by [202].

$$v_d = v_c + v_g = \frac{m}{q} \frac{\mathbf{R}_{cr} \times \mathbf{B}}{R_{cr}^2 B^2} \left( v_{\parallel}^2 + \frac{1}{2} v_{\perp}^2 \right) \quad (5.41)$$

where  $v_c$  and  $v_g$  are the drift due to curvature and gradient of the magnetic field.  $v_{\parallel}$  and  $v_{\perp}$  denotes velocity parallel and perpendicular to magnetic lines of force,  $R_{cr}$  the radius of curvature and  $\mathbf{B}$  is the magnetic field.

As discussed above the behavior of the charged species in magnetic field is mainly governed by two factors viz. electromagnetic interaction [Eqn.(5.16)] and curvature gradient drift [Eqn.(5.41)] along with magnetic field distortion [Eqn.(5.28)]. Since mass of the electron is much less than that of ions, movement of ions due to electromagnetic force ( $\text{acc} = qvB/m$ ) can be neglected compared to that of electrons. Similarly, drift for the electrons can be neglected compared to that of ions due to curvature of magnetic field ( $v_d \propto m$ ). In position P, the electrons and ions move in the same direction compared to position R where they move in opposite direction because of the reversal in the direction of radius of curvature. The situation is schematically shown in Fig.5.26. The movement of electrons



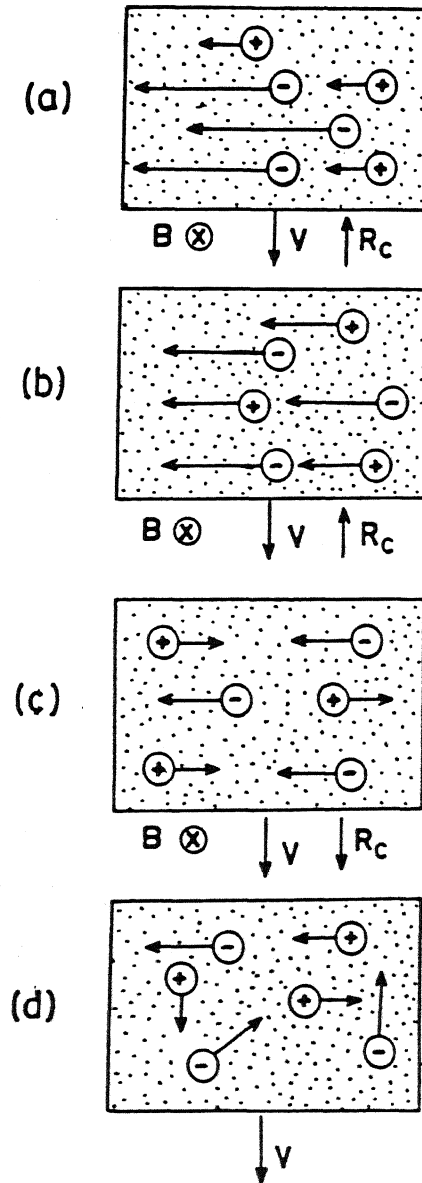


Figure 5.26: Motion of electrons and ions due to electromagnetic interaction and curvature gradient drift (a) positive field gradient with radius of curvature opposite to the direction of propagating plasma; (b) with the gradient less than case (a); (c) negative field gradient with the radius of curvature in the same direction of propagating plasma and (d) no magnetic field.

and ions in the same direction may favor recombination of electrons with ions to form  $C_2$  molecule in position P compared to position R. This may be the reason for not getting  $C_2$  emission at position R. Regarding the motion of electrons and ions, position Q is similar to position P but the velocity of the electrons is less in position Q compared to position P because of lower effective magnetic field in position Q. This results in generation of less  $C_2$  in position Q compared to position P. The velocity of the electrons is highest in position P followed by position Q and R because of difference in effective magnetic field which causes ohmic heating highest in position P resulting in highest intensity of spectral lines followed by position Q and R. The reason for lower intensity in position R compared to that of no magnetic field case is not very clear. It may be possible that the motion of plasma in a concave magnetic field (position R) causes Rayleigh-Taylor instability [206] to occur resulting in sharp fall in emission intensity.

#### 5.4.4 Langmuir probe spectra

Langmuir probe was kept at a distance of 4 mm and at an angle of  $45^\circ$  from the target surface where laser beam hit the surface. The output signal was recorded by varying the probe voltage from -160 V to +160 V in presence and absence of magnetic field. A triple peak structure is observed for the positive probe voltage as shown in Fig.5.27. It was suggested [157] that peak 1 is due to photoelectric emission current from the probe caused by the UV light emitted by the dense plasma, peak 2 is due to the fast component of the plasma and peak 3 is due to the main component of the plasma produced by laser-target interaction. It is found that increasing the voltage from 10 Volt onwards intensity of peak 1 and 2 remains almost constant whereas intensity of peak 3 increases. The I-V characteristics for the case of plasma motion in presence and absence of magnetic field has been calculated from the Langmuir probe signal using the third peak as shown in Fig.5.28. It is observed that in case of magnetic field the ionic part ( the negative voltage side) does not saturate unlike the case of no magnetic field where it saturates. The flow of ions are mainly governed by curvature of the magnetic field which may be responsible

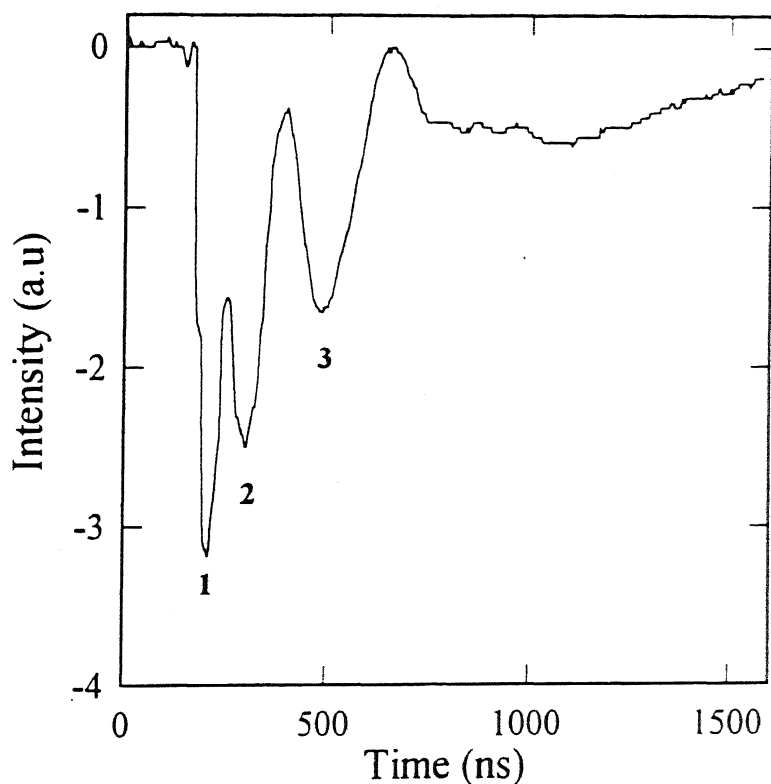


Figure 5.27: A typical Langmuir probe signal at a distance of 4 mm from the target and at a probe potential of + 10 Volt

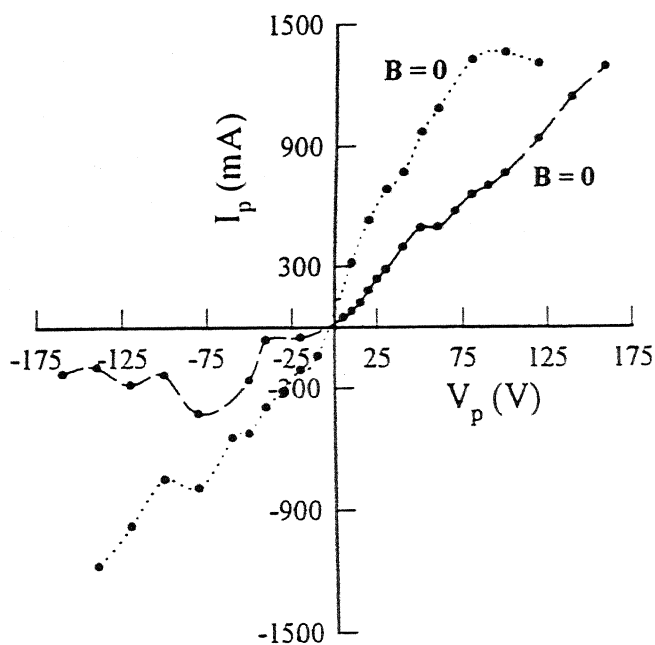


Figure 5.28: I-V characteristics of Langmuir probe signal for the case of plasma in presence and absence of magnetic field.

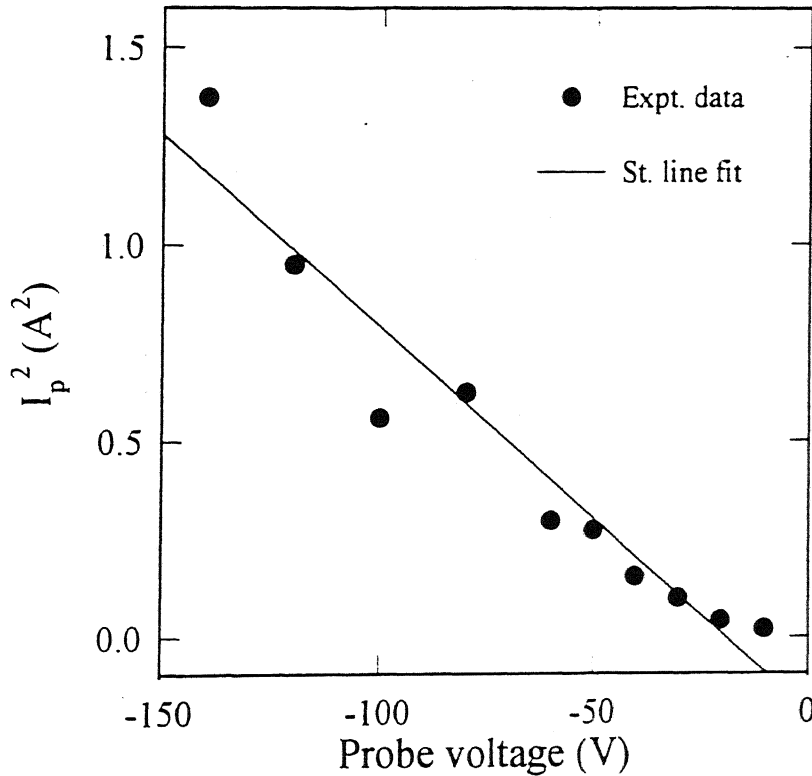


Figure 5.29: Square of the probe current is plotted against probe voltage and along with a straight line fit.

for the unusual behavior of ion current not saturating in magnetic field. The square of the probe current is plotted with negative probe potential as shown in Fig.5.29. for the case of magnetic field. The slope of the curve gives the ion density according to the Eqn. (2.10). The ion density in case of magnetic field is found to be higher than that of no magnetic field case. The estimated density at an angle of  $45^\circ$  to the target normal is in agreement with earlier work [100]. The increase in ion density in magnetic field has been observed earlier by us using ICCD photography and emission spectroscopy and is due to compression of plasma due to magnetic field as discussed before. Eqn. (2.9) is used to calculate electron temperature where  $\ln(I_p - I_{L0})$  is plotted against probe voltage for both magnetic field and without magnetic field. The electron temperature in case of magnetic field at a distance of 4 mm and at an angle of  $45^\circ$  is estimated to be 4.57 eV compared to 4.21 eV without magnetic field. Increase in temperature in the presence of magnetic field has been observed earlier using emission spectroscopy which is due to ohmic heating

caused due to surface current in magnetic field.

# Chapter 6

## Instabilities in a Laser Ablated Plasma Expanding in a Magnetic Field

---

### 6.1 Introduction

The generation of a dense high-temperature plasma using lasers is of prime importance in the field of plasma physics due to its technological applications and rich physics underlying the phenomena. A hot plasma which expands across a magnetic field offers the possibilities of investigation of instabilities. The physics of plasma flow across magnetic field lines regarding its collimation and stability properties are of particular relevance to the solar wind evolution [207], astrophysical jets [208], bipolar flows associated with young stellar objects [209], beam plasma heating [10] and cross field injection fueling of tokamak plasmas [210].

Plasma propagation across magnetic field falls between two extreme limits. In case

---

<sup>0</sup>The work presented in this Chapter is based on :

1. "Instabilities in laser produced carbon plasma expanding in a nonuniform magnetic field at low pressure ambient atmosphere" A. Neogi and R. K. Thareja, communicated to *Phys. Plasmas*.

of low  $\beta$  (particle pressure / magnetic pressure) plasma i.e. in the nondiamagnetic limit, magnetic field simply diffuses into whole of the plasma and the plasma moves across B field by  $E \times B$  drift [211] whereas in case of high  $\beta$  plasma i.e. in the diamagnetic limit, the plasma pressure being higher than magnetic pressure, the plasma "punches" its way across the magnetic field giving rise to Rayleigh Taylor (RT) instability as heavy fluid (plasma) is decelerated by light fluid (magnetic field) [134, 212]. The Kelvin-Helmholz (KH) instability is another kind of magnetohydrodynamic instability which arises in a stratified fluid if the different layers are in relative motion. Angelo [213] has examined the conditions of this instability in a fully ionized plasma immersed in a magnetic field and observed KH instability along the magnetic field. Peyser et. al. [131] designed an experiment where plasma is produced by interior illumination of a hollow glass cylinder which provides some degree of collimation to the emerging plasma which travels across magnetic field giving rise to plasma jet (above 3 kG). Surfaces of these jets undergo edge instability, time period of which matches with a modified form of KH instability [139-141].

There are three standard methods normally used to determine the stability or the properties of the instabilities associated with a given plasma equilibrium as discussed in detail in Chapter 1. They are *intuitive approach* in which the equilibrium is subjected to a perturbation that alters the forces acting on the plasma. The second method is based on *energy considerations* where equilibrium state of a plasma will be stable if potential energy is a minimum and may be unstable otherwise. A third way to determine the stability of a plasma equilibrium is *normal mode analysis*. This method assumes that if the equilibrium under investigation is perturbed, the linearized plasma equations for the time development of the perturbation can be solved, subject to the appropriate boundary conditions, assuming a time dependence of the perturbation of the form  $\exp(-i \omega_1 t)$ .

In this Chapter, we report on propagation of laser produced carbon plasma in an ambient atmosphere in a curved magnetic field (maximum of 3.5 kG). A characteristic delayed peak is observed in the temporal profile of CII transition at 426.7 nm and CIII transition at 465.0 nm. This delayed peak is not observed in case of only magnetic field or only

ambient atmosphere but is observed when both magnetic field and ambient atmosphere are present. Moreover, it is observed only in that region of the magnetic field where field lines are concave to the moving plasma which is one of the condition for RT instability to occur in magnetic field [202].

## 6.2 Rayleigh Taylor Instability

Rayleigh Taylor instability occurs at the interface of the two fluids of different densities when accelerated in a direction perpendicular to their interface; this interface is unstable or stable according to whether the acceleration is directed from heavier to the lighter medium or vice-versa [202, 206]. In other words Rayleigh Taylor instability occurs when the density grows in the direction against the accelerating force. A heavy fluid supported against gravity by a light fluid is a common example of Rayleigh Taylor instability. Studies of the behavior of small perturbations can be described by [25]

$$f' = f_0 \exp[i(k_1 r - \omega_1 t)] \quad (6.1)$$

For the motion of plasma (density =  $\rho_1$ ) in ambient gas (density =  $\rho_0$ ), we get

$$\omega_1^2 = -ka \frac{(\rho_1 - \rho_0)}{(\rho_1 + \rho_0)} = -ka_c \alpha \quad (6.2)$$

$$\alpha_1 = \frac{\rho_1 - \rho_0}{\rho_1 + \rho_0}$$

where  $a_c$  is the acceleration of the contact boundary. The plasma boundary is stable if  $\omega_1^2 > 0$  whereas if  $\omega_1^2 < 0$  the perturbation grows exponentially. The growth time of perturbation is given by

$$\tau_p = (ka\alpha_1)^{-\frac{1}{2}} \quad (6.3)$$

In plasma, a Rayleigh Taylor instability can occur when a dense plasma (heavy fluid) is supported against gravity (light fluid) by the pressure of a magnetic field. Now if the plasma is disturbed slightly its motion can deform the magnetic field lines in such a way as to produce magnetic forces that tend to amplify the original disturbance. The plasma



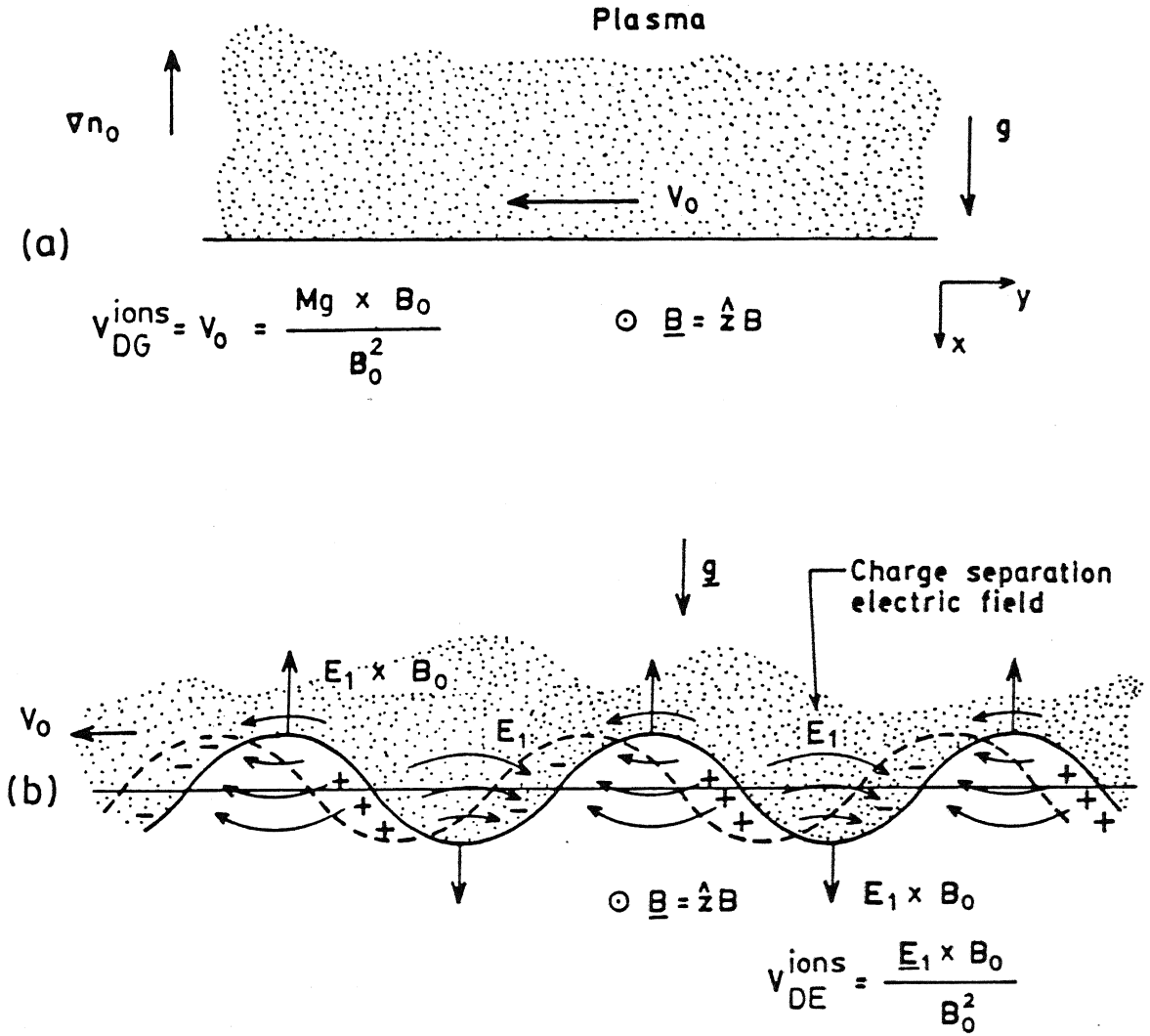


Figure 6.1: (a) Plasma (heavy fluid) supported by magnetic fluid (light fluid) against gravity; (b) Ripples at the surface got enlarged due to  $\mathbf{E} \times \mathbf{B}$  drift giving rise to Rayleigh Taylor instability.

moving in a curved magnetic field experiences a centrifugal force due to particle motion along the curved lines of force which act as an equivalent of "gravitational force" in a conventional system discussed above.

Consider a plasma boundary lying in a Y-Z plane as shown in Fig.6.1(a). Let there is a density gradient  $\Delta n_0$  in the -X direction and a gravitational field  $g$  in the X direction. It is assumed that  $\beta$  is low such that  $B_0$  is uniform throughout. The plasma is supported due to magnetic pressure. The ions and electrons initially drift parallel to the Y axis as a result of the gravitational force and the magnetic field which is commonly called "gravitational

drift" in plasma physics.

$$v_{DG} = \frac{M\bar{g} \times \bar{B}_0}{eB_0^2} \quad (6.4)$$

Since the drift velocity is inversely proportional to the charge to mass ratio, the ions and electrons drift in opposite directions and the ions have a velocity that is  $\frac{m_i}{m_e}$  greater than electrons.

If a ripple develops at the interface as a result of random thermal fluctuations, the drift  $v_0$  will cause the ripple to grow as shown in Fig.6.1(b). The drift of ions causes a change to build up on the sides of the ripple and an electric field develops which changes sign on going from crest to trough in the perturbation. This electric field interacts with magnetic field giving rise to well known  $\bar{E} \times \bar{B}$  drift,

$$v_{DE} = \frac{\mathbf{E}_1 \times \mathbf{B}_0}{B_0^2} \quad (6.5)$$

This  $\mathbf{E}_1 \times \mathbf{B}_0$  drift is upward where the surface has moved upward and downward the ripple grows as a result of these properly phased  $\mathbf{E}_1 \times \mathbf{B}_0$  drifts. The growth rate of the instability is calculated using the usual linearized wave analysis.

The condition for instability to occur is

$$-g \frac{n'_0}{n_0} > \frac{1}{4} k^2 v_0^2 \quad (6.6)$$

where  $n'_0 = \frac{\partial n_0}{\partial x}$  is the density gradient and  $k$  the wave vector. The growth rate is given by

$$\gamma_g = \left[ -g \frac{n'_0}{n_0} \right]^{\frac{1}{2}} \quad (6.7)$$

$$\gamma_g = \left[ \frac{g}{s} \right]^{\frac{1}{2}} \quad (6.8)$$

where  $s$  is the density gradient scale length given by  $\frac{n_0}{n'_0}$ . From the condition of instability, Eqn.(6.6) the instability occurs when  $g$  and  $\frac{n'_0}{n_0}$  have opposite sign. This is similar to the statement that light fluid is supporting the heavy fluid. In practical situation the plasma is hardly affected by gravity. The effect of magnetic field curvature is similar to  $g$  where plasma particles flowing along the curved magnetic lines experiences a centrifugal force. Thus, if the lines of force are concave to the moving plasma, the centrifugal force and

the density gradient are in opposite direction fulfilling the condition of Rayleigh Taylor instability. However, if the lines of force are convex to the moving plasma, the plasma tend to be stabilized.

### 6.3 Results and Discussion

The plasma expanding in vacuum, low pressure ambient atmosphere, variable magnetic field in vacuum and in presence of air is studied by time resolved emission spectroscopy. The time resolved emission spectra of carbon plasma were recorded at different distances away and parallel to the target surface by moving the monochromator in a plane perpendicular to the target surface. The temporal profiles of CI transition  $2p^3\ ^3D^0 - 8f\ F(5/2)$  at 399.7 nm, CII transition  $3d\ ^2D - 4f\ ^2F^0$  at 426.7 nm, CIII transition  $3s\ ^3S - 3p\ ^3P^0$  at 465.0 nm and CIV transition at  $3s\ ^2S - 3p\ ^2P^0$  at 580.1 nm were recorded at different distances from the target surface at various pressures of air. Each of these transitions is one of the strongest transitions in their respective ionic states. The emission lines are identified using the information available in the literature [184].

In case of vacuum a single peak structure is observed for all the species CI, CII, CIII and CIV whereas double peak structure is observed for the case of plasma expanding in low pressure ambient atmosphere (5 mTorr, 100 mTorr air) in CI, CII and CIII transitions and has been discussed in detail in Chapter 4. This double peak structure is attributed to stratification of the plasma into slow and fast components. In case of variable magnetic field in vacuum, the temporal profile of the species show multiple peaks and oscillations are observed mainly due to edge effects. It is observed through ICCD photography that the plume splits into two lobes which move towards the two poles of the magnet. Each lobe contains a fast, intermediate and slow component which gives rise to multiple peak in the spectra. A detailed study of the plasma expansion in variable magnetic field in vacuum is described in Chapter 5 [129, 178].

When air is introduced at low pressure in magnetic field, the multiple peaks and oscillations observed in the temporal profile disappear. The nature of the temporal profile

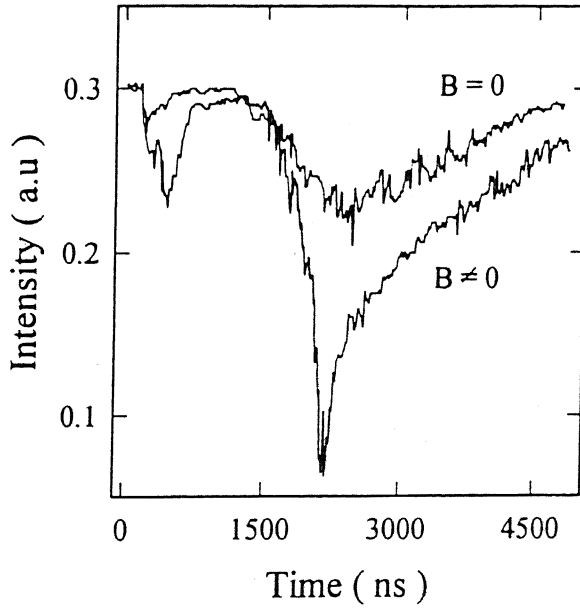


Figure 6.2: The temporal profile of CII transition at 5 mTorr air pressure with and without magnetic field.

is dominated by the gas rather than that by the magnetic field, i.e. the temporal profile in 5 mTorr/100 mTorr air in magnetic field resembles closely the case of 5 mTorr/100 mTorr air without magnetic field. The difference caused due to the presence of magnetic field is the increase in intensity of the temporal profile, dominance of the intensity of the first peak over the second peak for a larger distance and the increase in onset distance of double peak compared to no magnetic field case (*i. e.* only gas). Figure 6.2 shows the temporal profile of CII at 20 mm at 5 mTorr air pressure with and without magnetic field. The delayed second peak is of higher intensity in magnetic field at this distance and onwards. This is because of ohmic heating at the front edge of the plume which is caused due to surface current which arises when plasma moves in a magnetic field.

An interesting feature is observed when plasma expands in 100 m Torr air in magnetic field. The second peak gets suddenly delayed after a certain critical distance in case of CIII and CII but not for CI. In order to investigate the above process the experiment was done keeping the target in six different positions in magnetic field at T1, T2, T3, T4, T5 and T6 as shown in Fig.6.3. It is observed that the temporal profile of CIII transitions show a sudden increase in delay of the second peak after a certain critical distance as shown in

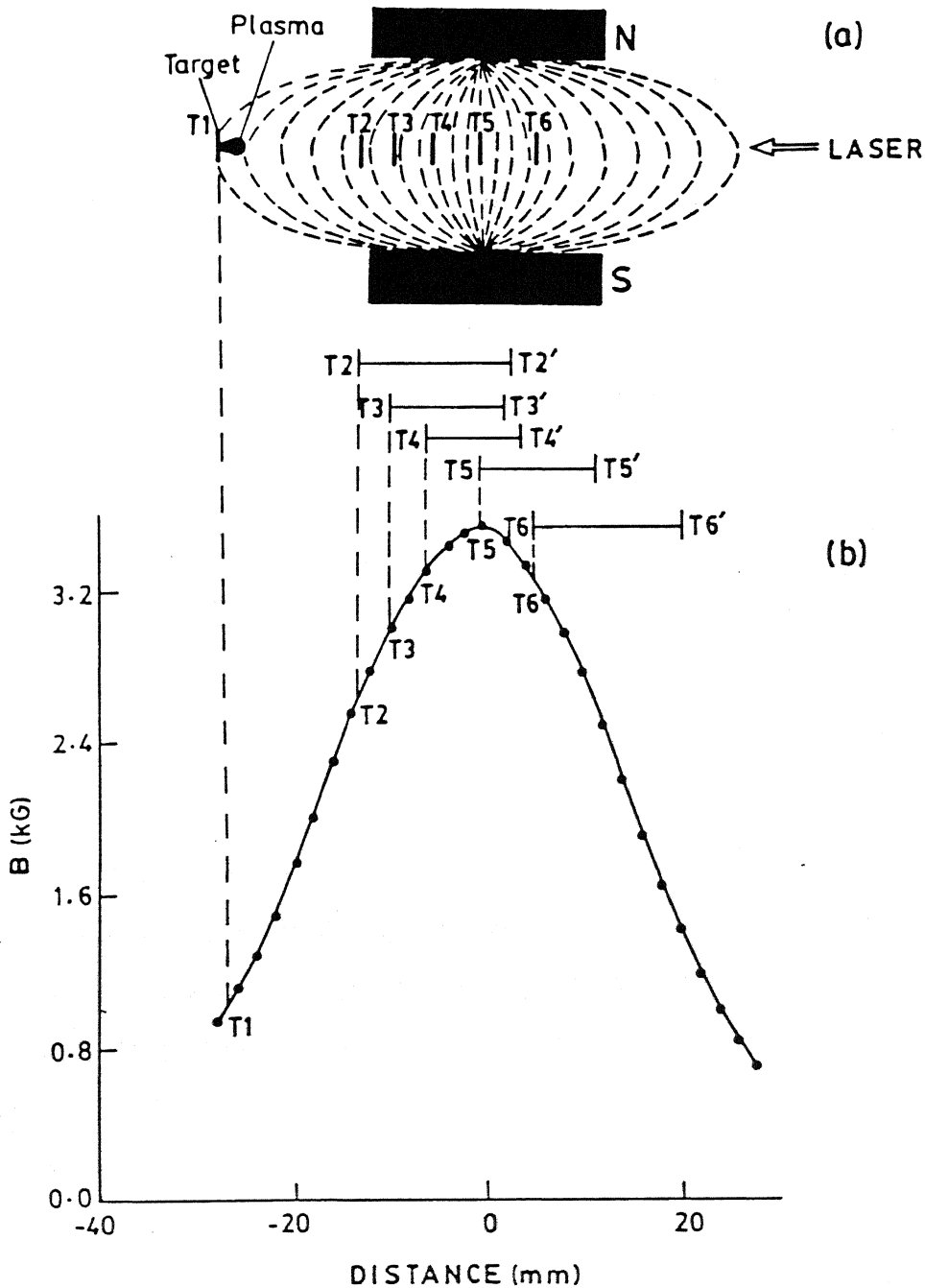


Figure 6.3: (a) Six different target positions in nonuniform magnetic field; (b) The variation of magnetic field strength along the direction of propagation of plasma.

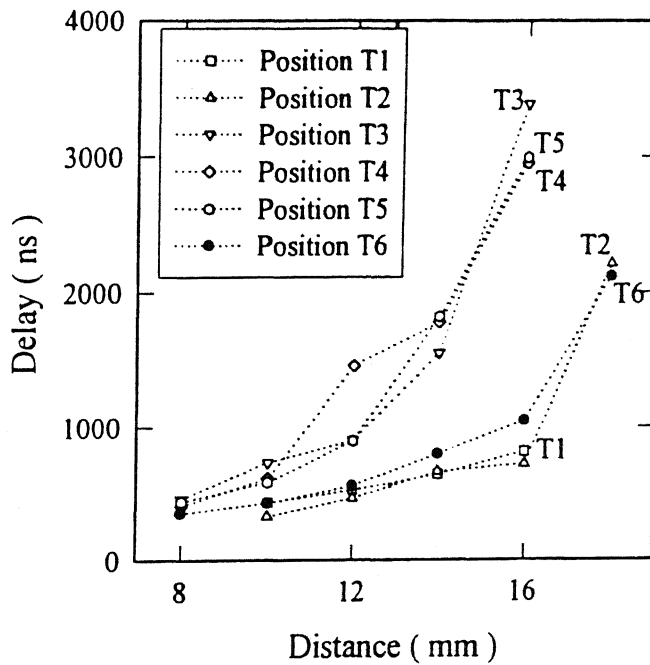


Figure 6.4: Variation of delay of the second peak as a function of distance from the target position T1, T2, T3, T4, T5 and T6 respectively.

Fig.6.4 for all positions of target except at T1. Position T2 shows increase in delay after 16 mm, position T3 after 12 mm, position T4 after 10 mm, position T5 after 12 mm and position T6 after 16 mm respectively. It is important to note that this delayed second peak occurs only at the latter half of the magnet and not in the first half of the magnet. Figure 6.3 shows the position of the target and the corresponding point of increased delay, e.g. for position T2 it occurs at T2' and similarly for others. Figure 6.5 shows that as the target is moved towards increasing side of magnetic field from T2 to T4 where the plasma first expands in the convex part of magnetic field and then concave region, the onset distance for the delayed second peak decreases. For the position T5 and T6, the plasma expands completely in the region where magnetic field lines are concave. As target is moved from position T5 to T6 the onset distance for the delayed second peak increases. Another interesting feature observed is the appearance of a third peak as one goes from position T2 to other positions inside the magnet in the direction of increasing magnetic field. This occurs just before the occurrence of the delayed second peak. Figure 6.6 shows a distinct third peak (P3 in the figure) at 12 mm (dashed line) which disappears at 14 mm

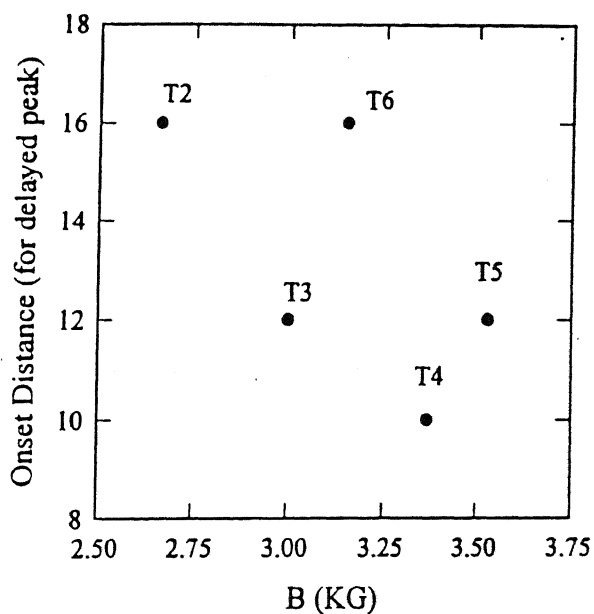


Figure 6.5: The onset distance for the occurrence of delayed second peak for different position of the target.

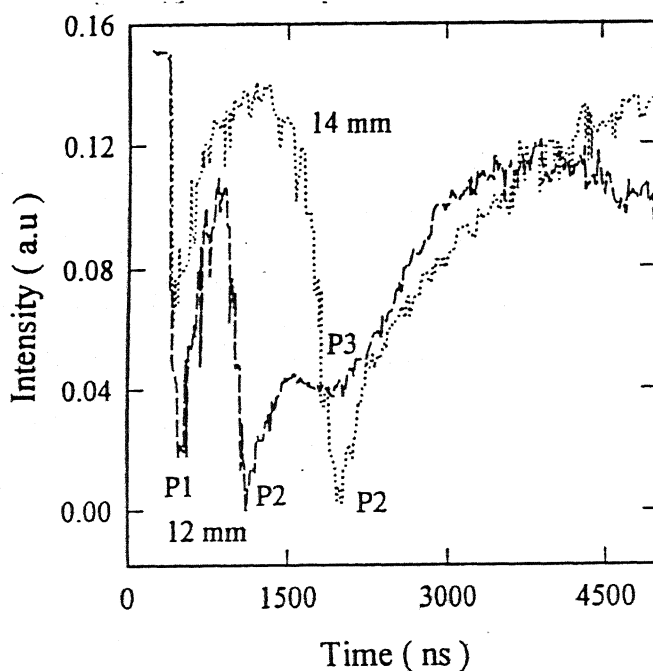


Figure 6.6: The dark line represents the temporal profile of CIII transition at 12 mm and the dotted line is at 14 mm. P1, P2 and P3 are the first, second and third peak respectively. The third peak does not appear at 14 mm.

(dotted line) giving rise to a delayed second peak when the target is at position T5; the peak eventually disappears as in position T6 where magnetic field is much less than that at T5.

Now we consider various processes responsible for the formation of delayed second peak and third peak. They may be due to recombination - three body recombination and radiative recombination, charge exchange or magnetohydrodynamic instability. If recombination is the cause, the delayed second peak should occur more prominently for CI and CII transition and not for CIII transition. However, it is observed for CIII and not for CI, the recombination cannot be responsible for the formation of delayed second peak. In charge exchange process an energetic ion or neutral captures either an ion or an electron and gets transferred to an energetic neutral. Since the delayed second peak is not observed for the neutrals, the probability of charge exchange process is rather low. Let us see the possibility of magnetohydrodynamic instabilities for the cause of delayed second peak. The growth rate calculations of Rayleigh-Taylor (RT) instability in magnetic field show that instability can occur when  $-g \left( \frac{\partial n_0}{\partial x} \right) / n_0 > 0$  [202] i.e. when  $g$  and density gradient scale length of the plasma are in a direction opposite to each other. Since  $g$  can be used to model the effects of magnetic field curvature, so Rayleigh-Taylor instability can occur only when magnetic field lines are concave to the moving plasma. This is exactly the situation in our case. The delayed second and third peak occur only at the latter half of the magnet where magnetic field lines are concave to the moving plasma. When the target is kept to the extreme left (position A) such that plasma mostly travel through the first half of the magnet where magnetic field lines are convex to the moving plasma, the delayed second peak is not observed. The delayed second peak for CIII ions is formed due to two consecutive processes. As RT instability grows, cracks or fissures like structure develops at the surface which helps air to diffuse into the plasma giving rise to delayed peak as shown schematically in Fig.6.7. Since charged particles play the major role at the surface no delayed second peak is observed in neutrals (CI).

An attempt has been made to calculate the growth time of RT instability from the



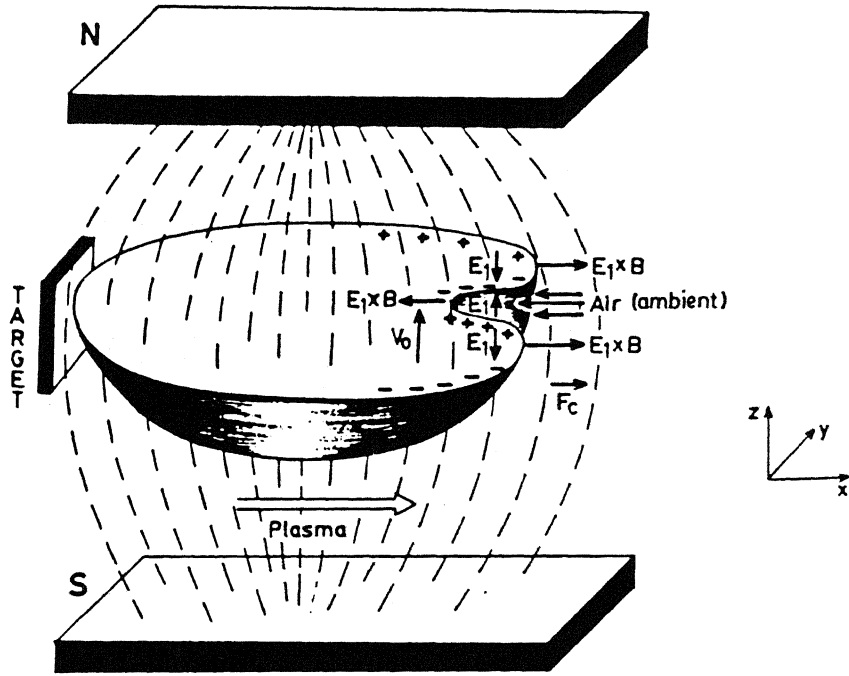


Figure 6.7: A schematic diagram showing the expansion of plasma in magnetic in presence of air. The Rayleigh-Taylor instability gives rise to cracks or fissures which allows air to diffuse into the plasma giving rise to delayed second peak.

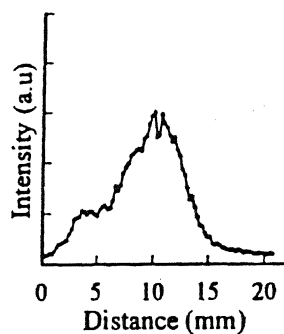
intensity plots of ICCD photographs of the plume. The maximum growth rate of instability is given by [25].

$$\gamma_g = \left( \frac{g_{eff}}{s} \right)^{\frac{1}{2}}$$

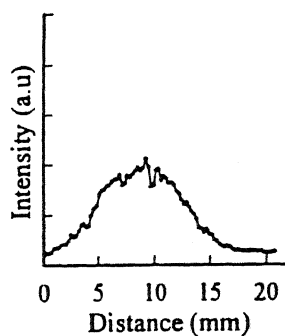
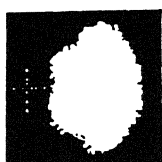
Where  $g_{eff}$  is the effective deceleration due to magnetic field and  $s$  is the density gradient scale length. Figure 6.8 gives ICCD images and the intensity plots at 1000, 1500 and 2000 ns. It is a plot of total emission intensity of all the ions and neutrals. It is difficult to resolve the peaks. The growth time of the instability which is the inverse of growth rate given by Eqn.(6.8) can be estimated from the values of  $g_{eff}$  and  $s$ . The density gradient scale length at 1000 ns is estimated to be 5 mm from Fig.6.8 (the length from the plasma boundary where density gradient remains constant). Figure 6.9 gives the plot of velocity of the plasma front with time calculated from ICCD photographs.  $g_{eff}$  is estimated to be  $0.554 \text{ cm}/\mu \text{ sec}^2$ . The growth time of the RT instability which is inverse of growth rate comes out to be  $0.95 \mu \text{ sec}$ .

To conclude, a sudden increase in the delay of the second peak in CIII transition is

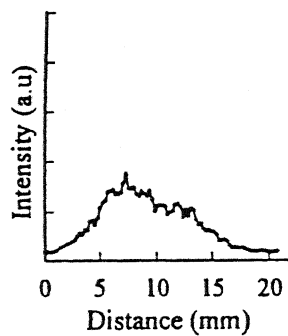
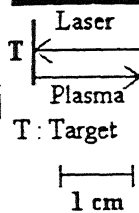
(a) 1000 ns



(b) 1500 ns



(c) 2000 ns



T |

Figure 6.8: The ICCD images and intensity profile of the plume from ICCD photographs at 1000 and 1500 ns and 2000 ns.

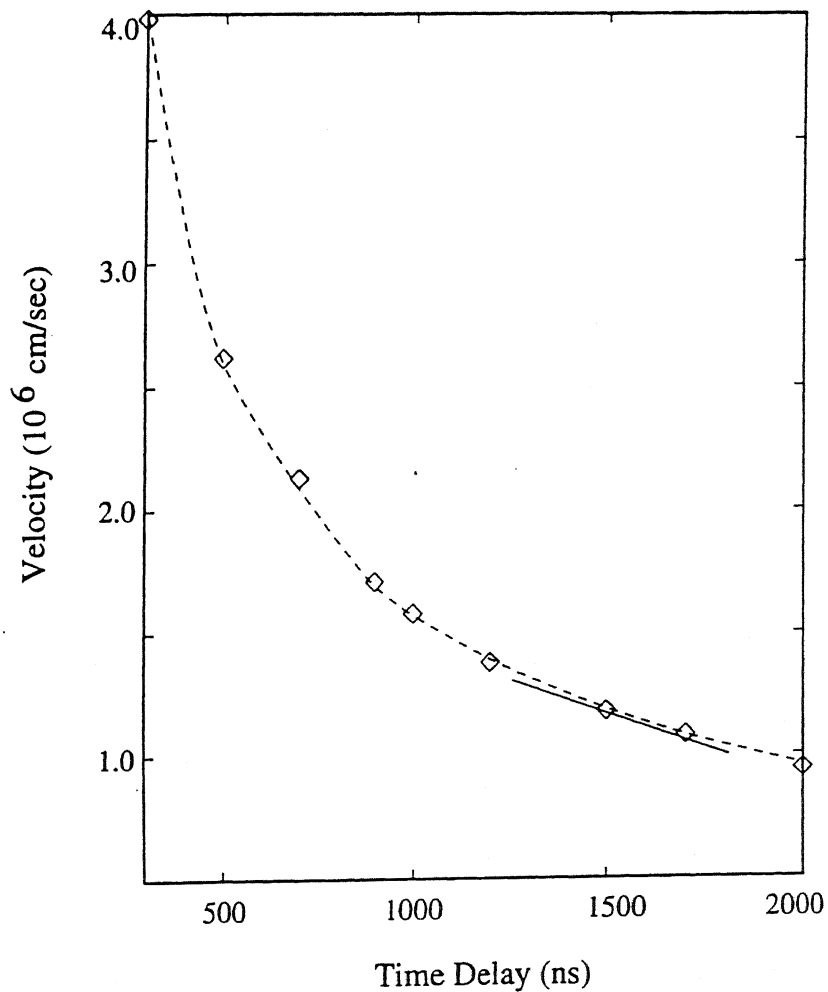


Figure 6.9: The temporal variation of the velocity of the plume front calculated from ICCD photographs. The slope of the curve gives the deceleration in magnetic field.

observed in case of carbon plasma expanding in nonuniform magnetic field in 100 mTorr air by changing the position of the target in magnetic field. It is observed that the enhanced delay occurs in that part of magnetic field where magnetic field lines are concave to the moving plasma. Since Rayleigh Taylor instability occurs when plasma expands in concave magnetic field, so Rayleigh Taylor instability along with diffusion of air is attributed as the cause for the formation of delayed second peak. The growth rate of Rayleigh Taylor instability is estimated from the intensity and velocity profile of ICCD photographs.

# Chapter 7

## Conclusion

---

To conclude, the laser ablated carbon plasma expanding in an ambient gas and nonuniform magnetic field has been investigated using emission spectroscopy, fast photography and Langmuir probe. Modifications are done in one dimensional Lagrangian code MEDUSA to simulate the behavior of the plasma front expanding in ambient atmosphere of He, Ne, Ar and Xe. The simulated result match well with the experimental observations. The two dimensional images of the plasma plume expanding in low pressure ambient atmosphere exhibit stratification of the plume into slow and fast components. The plasma plume expanding in magnetic field shows oscillatory behavior of the plume front in agreement with theoretical predictions. Using the time integrated spectra of the plasma plume expanding in nonuniform magnetic field it is shown how the gradient and curvature of the magnetic field controls the plasma behavior. Multiple peak structure in the temporal profiles of various species of the plume is observed in case of plasma expanding in nonuniform magnetic field. The observed delayed behavior of the temporal profile in nonuniform magnetic field in presence of ambient gas is attributed to the onset of Rayleigh-Taylor instability in plasma.

An one dimensional Lagrangian Code MEDUSA which simulates the temporal and spatial evolution of laser ablated plasma in vacuum is modified for the plasma expansion

in high pressure ambient atmosphere (of He, Ar, Ne and Xe). Rankine-Hugoniot relations for the shock wave are used to calculate the boundary conditions of the plasma front. Prandtl's mixing length theory is used to calculate the total shear stress or the viscous drag experienced by the plasma boundary. The external gas diffuses into the plasma plume when the pressure outside the plasma front is almost equal to the pressure inside the plume which gives rise to a diffusive force opposing the motion of the plasma. Finally, the Navier-Stokes equation is modified by incorporating the viscous drag term and diffusive force term. The simulated results using modified MEDUSA code (with the changed boundary conditions and modified Navier-Stokes equation) matches well with the experimental observations. The plasma parameters like velocity, temperature, pressure and electron density of the plasma front can be simulated for any gas at any higher pressure with the help of the modified code.

The temporal profiles of CI transition  $2p^3\ ^3D^0 - 8f\ F(5/2)$  at 399.7 nm, CII transition  $3d\ ^2D - 4f\ ^2F^0$  at 426.7 nm, CIII transition  $3s\ ^3S - 3p\ ^3P^0$  at 465.0 nm and CIV transition at  $3s\ ^2S - 3p\ ^2P^0$  at 580.1 nm were recorded at different distances from the target surface at various pressures of air (0.1 mTorr, 5 mTorr and 100 mTorr). The intensity of the species is observed to increase in presence of ambient gas. The ICCD photographs at 5 mTorr at various delay times show stratification of plasma plume into two components, fast and slow at 600 ns. The velocity of the two components is estimated to be  $1.0 \times 10^6$  cm/sec and  $7.5 \times 10^5$  cm/sec and hence termed as fast and slow components respectively. The ICCD images show that the fast component is bulky at earlier time whereas slow component becomes bulky at later time. In vacuum the temporal profiles show a single peak structure for all the species. In 5 mTorr and 100 mTorr, double peak structure is observed for CI, CII and CIII transitions whereas no double peak is observed for CIV transition. The stratification of the plasma plume is attributed to the diffusion of ionized air particles into the plasma plume and collisions with the different charged species of the plasma plume. The collided species give rise to slow component whereas uncollided species give rise to fast component resulting in stratification.

The ICCD photographs of the plasma expanding in a nonuniform magnetic field show oscillatory behavior of the plasma front at various delay times (150 and 500 ns) in accordance with the theoretical predictions. At later time ( $\sim 1000$  ns) the plume is observed to break into two lobes which move toward the poles of the magnet. The ICCD images were used to estimate the plasma parameters. The electron density in presence of magnetic field is found to be higher than that of vacuum case and shows oscillations because of alternate contraction and expansion of the plasmoid at 150 and 500 ns. The temperature of the plasma plume is estimated assuming the plasma plume to behave as an ensemble of black body radiators. The temperature in case of magnetic field increases due to Ohmic heating caused by the surface current. In presence of ambient gas the temperature rises due to enhanced interparticle collisions with the gas particles. The calculated density and temperature of the plasma plume match well with the theoretical value.

The time integrated spectra of the plasma plume propagating in magnetic field were recorded at a distance of 6 mm from the target surface keeping the target at three different positions in nonuniform magnetic field. It is found that the curvature and the gradient of the magnetic field controls greatly the plasma behavior. The plasma expanding in convex magnetic field with positive field gradient shows a maximum rise in emission line intensity whereas in concave magnetic field with negative field gradient the line intensity decreases compared to that of no magnetic field case. Furthermore,  $C_2$  molecular Swan band emission,  $d^3\pi_g - a^3\pi_u$ , with  $\Delta v = -1, 0, 1$  is observed to dominate at the former position whereas at the latter position it is not observed. The temperature calculated from the ratio of line intensity of two lines of same ionization state at a distance of 6 mm from the target is higher in former position where the field gradient is positive (11.4 eV) compared to the latter where field gradient is negative (4.34 eV). The increase in line intensity is attributed to compression of magnetic field lines.  $C_2$  emission in the former position of the target is attributed to the movement of electrons due to electromagnetic interaction and that of the ions due to curvature gradient drift.

The time resolved spectra of carbon plasma were recorded for all the species CI, CII,

CIII and CIV in nonuniform magnetic field. It is found that the species at the outermost boundary, CII and CIV, show a single peak structure at 4 mm from the target surface whereas with increasing distance ( $\sim 10$  mm) multiple peaks (six peaks) are observed. They are because of two fast, two intermediate and two slow components arising from two asymmetric lobes. Multiple peaks and oscillations are observed in the temporal profile of CIII and CI when they are at the outermost boundary (14 mm from the target) where CII and CIV disappear. The oscillations are attributed to edge oscillations in magnetic field.

The temporal profiles of the species show interesting features when the plasma expands in combined environment of ambient gas and magnetic field. A sudden delay in second peak for CIII and CII species and a triple peak structure is observed but not for CI. This delay is not observed when the plasma expands in either only gas or only magnetic field. In order to investigate the delay the target was kept at six different positions in magnetic field and it was observed that the delay only occurs when the plasma expands in concave magnetic field. This behavior is attributed to the formation of fissures or cracks on account of Rayleigh-Taylor instability which occurs when a plasma expands in concave magnetic field lines which favors diffusion of air resulting in formation of delayed peak. The growth time of the instability is estimated to be 1000 ns from the ICCD photographs.

### **Future scope of the work**

It will be an interesting study to simulate the experimental observations of plasma behavior in magnetic field using Medusa code. Since  $\mathbf{J} \times \mathbf{B}$  and  $\mathbf{J}^2\eta$  term dominate the behavior of plasma motion in magnetic field, so alteration are needed in the energy equation of Medusa code. Since the MEDUSA code is one dimensional, two dimensional effects can be studied using two dimensional codes like CASTOR.

The effect of magnetic field curvature on plasma behavior can be studied by varying the curvature of magnetic field by changing the distance between the two poles of magnet. However, the time resolved spectroscopy of different species at different positions of magnetic field can be carried out. It will augment our knowledge of plasma behavior in curved magnetic field.

In the present experimental set up the behavior of plasma along the magnetic field lines could not be observed because the body of the poles obstruct the line of sight. If the plasma motion along the field can be viewed then magnetohydrodynamic instabilities can be observed using fast photography. Using those images one can more accurately calculate the density gradient scale length to estimate the growth rate of the instability.

The fast ablated plasma flow into a stationary ambient medium in presence of static magnetic field as discussed earlier can be used to study many magnetospheric and astrophysical processes. At low background gas pressure ( $P < 1 \text{ Torr}$ ) collisionless phenomena such as those occurring when solar wind impinges on magnetospheric and ionospheric plasmas and with obstacles such as comet, moons, and planets dominate. At high pressure ( $> 1 \text{ Torr}$ ) collisional interstreaming plasma effects such as blast wave formation are generated which behave like supernova shocks. Plasma expanding in magnetic field undergo RT instability. An analogous instability was observed in the tail of magnetosphere. The plasma behavior in curved magnetic field can be used to study the motion of the plasma in curved magnetic field of the earth like generation of ring current in the equatorial plane. Because of cosmic abundance of carbon in the interstellar space, spectroscopic study of carbon species is of great significance. The knowledge of plasma behavior in different ambient conditions elucidates our understanding regarding thin film deposition, surgery and many technological applications.



# Bibliography

- [1] J. C. Brandt, *Introduction to solar wind* (Freeman, San Francisco, 1970).
- [2] B. H. Ripin *et. al.* *Interaction and Related Plasma Phenomena* Vol. 7, eds. H. Horr, G. Miley (Plenum, New York, 1986) pp. 857-877.
- [3] P. Bernhardt, *et. al.* *Geophys. Res.* **92**, 5777 (1987).
- [4] A. N. Mostovych, B. H. Ripin and J. A. Stamper, *Rev. Sci. Instr.* **60**, 807 (1989).
- [5] C. K. Manka, *et. al.* *Laser Interaction with Matter* eds. G. Velarde, E. Minguez and J. Iado (World Scientific, Singapore, 1989) pp. 401-404.
- [6] J. A. Bittencourt, *Fundamentals of Plasma Physics* (Pergamon Press, Oxford, 1986).
- [7] C. L. S. Lewis and J. Meglinchay, *Opt. Commun.* **53**, 179 (1985).
- [8] B. H. Ripin, C. K. Manka, T. A. Peyser, E. A. Mclean, J. A. Stamper, A. N. Mostovych, J. Grun, K. Keavney, J. Y. Crawford and J. D. Huba, *Laser and Part. beam* **8**, 183 (1990).
- [9] J. P. Hare and H. W. Kroto, *Acc. Chem. Res.* **25**, 106 (1992).
- [10] *Pulsed laser deposition of thin films*, edited by D. B. Chrisey and G. K. Hubler (Wiley, New York, 1994).
- [11] R. K. Dwivedi and R. K. Thareja, *Phys. Rev. B.* **51**, 7160 (1995).
- [12] R. Bellantone and Y. Hahn, *J. Appl. Phys.* **76**, 1447 (1994).

- [13] W. NAM, H. Nishiyama and S. Kamiyama, JSME International J. series B **39**, 134 (1996).
- [14] Laser Induced Plasmas and Applications, edited by L. J. Radziemoki and D. A. Cremers (Dekker, New York, 1989).
- [15] S. Kraulhamer, R. S. L. Das, R. H. Frisbee, Proceedings of the 30 th Intersociety Energy conversion Engineering Conference (IEEE cat. No. 95 CH35829), 30 July - 4 Aug. 1995 ( New York, NY, USA : ASME 1995), p-255 - 60 vol.1.
- [16] James E. A. John, Gas Dynamics, Second edition, (Allwyn & Bacon, INC , Boston, 1984).
- [17] H. Nishiyama, Turbomachinery **22**, 614 (1993).
- [18] D. C. Winburn, *What Every Engineer should know about Laser* (Marcel Dekker Inc, New York, 1987).
- [19] Jams J. Duderstadt and Gregry A. Moss, *Inertial Confinment Fusion* (John Wiley and Sons, New York, 1982).
- [20] J. F. Ready, *Effects of High Power Laser Radiation* (Academic, New York, 1971).
- [21] I. N. Mihailescu, N. Chitica, L. C. Nistor, M. Popescu, V. S. Teodorescu, I. Ursu, A. Andrei, A. Barborica, A. Luches, M. Luisa De Giorgi, B. Dubreuil and J. Hermann, J. Appl. Phys. **74**, 5781 (1993).
- [22] C. Champeaux, P. Marchet, J. Aubreton, J.-P. Mercurio and A. Catherinot, Appl. Surf. Sci. **69**, 335 (1993).
- [23] O. Auciello, Materials and Manufacturing Process **64**, 33 (1991).
- [24] V. Berardi et. al. J. Appl. Phys. **76**, 8077 (1994).
- [25] Anan'in, ByKovski, Yu. V. Eremin, A. A. Zhuravlev, O. S. Lyubchenko, I. K. Navikov and S. P. Frolov, Sov. J. Quantum Electronics **21**, 787 (1991).

- [26] H. Nishiyama, T. Sato and S. Kamiyama, Proc. 10<sup>th</sup> Int. Conf. Gas Discharges Their Appl. Swansea 2, 778 (1992).
- [27] T. Pisarczyk, A. Farynski, H. Fiedorowicz, P. Gogolewski, M. Kusnicrz, J. Makowski, R. Mikilaszewski, M. Mroczkowski, P. Parys and M. Szczurek, Laser and Particle Beams 10, 767 (1992).
- [28] E. Ott and W. M. Mannheimer, Nucl. Fusion 17, 1057 (1977).
- [29] A. N. Mostovych, B. H. Ripin and J. A. Stamper, Phy. Rev. Lett. 62, 2837 (1989).
- [30] L. Dirnberger, P. E. Dyer, S. R. Farrar and P. H. Key, Appl. Phys. A 59, 311 (1994).
- [31] J. S. Lash, R. M. Gilgenbach and C. H. Ching, Appl. Phys. Lett. 65, 531 (1994).
- [32] M. Aden, E. Beyer, G. Herziger and H. Kunze, J. Phys D, Appl. Phys. 57 (1991).
- [33] C. J. Knight, AIAA Journal 17, 519 (1979).
- [34] J. J. Macfarlane, G. A. Moses and R. R. Peterson, Phys. fluids B1 7, 635 (1989).
- [35] John. L. Giuliani, Jr. and Margaret Mulbrandon, Phys. fluids B1 7, 1463 (1989).
- [36] R. Tambay, R. Singh and R. K. Thareja, J. Appl. Phys. 72, 1197 (1992).
- [37] D. B. Geohegan and D. N. Mashburn, Appl. Phys. Lett. 55, 2345 (1989).
- [38] Y. Nakata, H. Kaibara, T. Okada and M. Maeda, J. Appl. Phys. 80, 2458 (1996).
- [39] Abhilasha, P. S. R. Prasad and Raj K. Thareja, Phys. Rev. E. 48, 2929 (1993).
- [40] R. K. Dwivedi, Ph.D thesis, IIT Kanpur (1997).
- [41] R. Timm, P. R. Willmott and J. R. Huber, J. Appl. Phys. 80, 1794 (1996).
- [42] T. P. Hughes, *Plasmas and Laser Light* (Wiley, New York, 1975).
- [43] V. Kumar and R. K. Thareja, J. Appl. Phys. 64, 5269 (1988).

- [44] R. K. Singh and J. Narayan, Phys. Rev. B. **41**, 8843 (1990).
- [45] P. K. Carroll and E. T. Kennedy, Contemp. Phys. **22**, 61 (1981).
- [46] C. Fauquignon and F. Floux, Phys. fluids **13**, 386 (1970).
- [47] S. Suckewer *et. al.*, Phys. Rev. Lett. **55**, 1753 (1985).
- [48] C. Steden and H. J. Kunze, Phys. Lett. A **151**, 534 (1990).
- [49] J. Dawson, P. Kaw and B. Green, Phys. fluids **12**, 875 (1969).
- [50] Ya. B. Zel'dovich and Yu. P. Raizer, *Physics of Shock Waves and High Temperature Hydrodynamics Phenomenon* Vol.I (Academic, New York, 1966).
- [51] J. P. Christiansen, DETF Ashby and K. V. Roberts, Comp. Phys. Comm. **7**, 271 (1974).
- [52] J. P. Christiansen *et. al.* Comp. Phys. Comm. **17**, 397 (1979).
- [53] G. B. Zimmerman and W. L. Kruer, Comments Plasma Phys. Controlled Fusion, **11**, 51 (1975).
- [54] R. F. Schmalz, J. Meyer-ter-vehn and R. Ramis, Phys. Rev. A **34**, 2177 (1986).
- [55] H. Nishimura *et. al.* Phys. Rev. A **43**, 307 (1991).
- [56] S. Kiyokawa, T. Yabe and T. Mochizuki, Jap. J. Appl. Phys. **22**, 1772 (1983).
- [57] R. Ramis, R. F. Schmalz and J. Meyer-ter-vehn, Comp. Phys. Comm. **49**, 475 (1988).
- [58] A. Neogi and R. K. Thareja, Pramana **50**, 63 (1998).
- [59] R. Bellantone and Y. Hahn, J. Appl. Phys. **76**, 1436 (1994).
- [60] O. B. Anan'in, Yu. A. By Kovskii, Yu. V. Eremin, A. A. Zhuravlev, O. S. Lyubchenko, I. K. Novikov and S. P. Frolov, Laser Phys. **2**, 711 (1992).

- [61] L. I. Sedov, *Similarity & Dimensional Methods in Mechanics* (Academic, New York, 1959); G. I. Taylor, *Proc. R. Soc. London. Ser A* **201**, 175 (1950).
- [62] J. C. S. Kools, *J. Appl. Phys.* **74**, 6401 (1993).
- [63] S. S. Harilal, Riju C. Issac, C. V. Bindhu, V. P. N. Nampoori and C. P. G. Vallabhan, *J. Appl. Phys.* **81**, 3637 (1997).
- [64] T. Kerdja, S. Abdelli, D. Ghobrini and S. Malek, *J. Appl. Phys.* **80**, 5365 (1996).
- [65] Abhilasha and R. K. Thareja, *Appl. Phys. Lett.* **61**, 63 (1995).
- [66] R. K. Thareja, R. K. Dwivedi and Abhilasha, *Phys. Rev. B* **55**, 2600 (1997).
- [67] D. B. Geohegan, A. A. Puretzky, R. L. Hettich, X. Y. Zheng, R. E. Haufler and R. N. Compton, *Appl. Advanced Material '93, IV / Laser and Ion Beam Modification of Materials* eds. I. Yamada *et. al.* *Trans. Mat. Res. Soc. Jpn.* Vol. 17 2345 (1989).
- [68] T. Venkatesan *et. al.* *Appl. Phys. Lett.* **53**, 1431 (1988).
- [69] J. P. Zheng, Q. Y. Ying, S. Wiranachchi, Z. Q. Huang, D. T. Shaw, and H. S. Kwok, *Appl. Phys. Lett.* **54**, 954 (1989).
- [70] C. Girault, D. Damiani, J. Aubreton, and A. Catherinot, *Appl. Phys. Lett.* **55**, 182 (1989).
- [71] P. E. Dyer, A. Issa, and P. H. Key, *Appl. Surf. Sc.* **46**, 89 (1990); P. E. Dyer, A. Issa, and P. H. Key, *Appl. Phys. Lett.* **57**, 186 (1990).
- [72] A. Gupta, B. W. Hussey, A. Kussmaul, and A. Segmuller, *Appl. Phys. Lett.* **57**, 2365 (1990).
- [73] K. Scott, J. M. Huntley, W. A. Phillips, J. Clarke, and J. E. Field, *Appl. Phys. Lett.* **57**, 922 (1990).

- [74] D. B. Geohegan, in *Surface Chemistry and Beam-Solid interactions*, Material Research Society, Pittsburgh, PA 1990, p557.
- [75] D. B. Geohegan, in *Laser Ablation-Mechanism and Applications*, (Springer, Berlin, 1991), p28.
- [76] Yoshiki Nakata, Wanniarachchi, K. A. Kumuduni, T. Okada, and M. Maeda, *Appl. Phys. Lett.* **64**, 2599 (1994).
- [77] Francesco Fuso, Leonid Vyacheslavov, Guglielmo. Masciarelli, and Ennio Arimondo, *J. Appl. Phys.* **76**, 8088 (1994).
- [78] D. B. Geohegan, *Appl. Phys. Lett.* **60**, 2732 (1992).
- [79] E. Dyer, and R. J. Farlay, *J. Appl. Phys.* **74**, 1442 (1993).
- [80] E. B. D. Bourdon, W. W. Duley, A. P. Jones, and R. H. Prince, in *Diamond and Diamond like Films and Coatings*, edited by R. E. Clausing *et. al.* (Plenum, New York 1991).
- [81] D. L. Pappas, K. L. Saenger, J. Bruley, W. Krakow, and J. J. Cuomo, *J. Appl. Phys.* **71**, 5675 (1992).
- [82] T. Sato, S. Furuno, S. Iguchi, and M. Hanabusa, *Jpn. J. Appl. Phys.* **26**, L 1487 (1987).
- [83] J. C. S. Kools, C. J. C. M. Nillesen, S. H. Brongersma, E. Vande Riet, and J. Dieleman, *J. Vac. Sci. Technol. A* **10**, 1409 (1992).
- [84] Peter K. Schenck, John W. Hastle, Albert J. Paul and David W. Bonnell, *Opt. Eng.* **35**, 3199 (1996).
- [85] H. W. Kroto, R. J. Heath, S. C. O'Brein, R. F. Curl and R. E. Smalley, *Nature*, **318**, 165 (1985).

- [86] T. Guo, C. Jin, and R. E. Smalley, *J. Phys. Chem.* **95**, 4948 (1991).
- [87] F. Vega, C. N. Afonso and J. Solis, *J. Appl. Phys.* **73**, 2472 (1993).
- [88] H. S. Kim and H. S. Kwok, *A. Phys. Lett.* **61**, 2234 (1992).
- [89] Seung Min Park, Heebyung Vhae, Sangwook Wee and Inhyung Lee, *J. Chem. Phys.* **109**, 928 (1998).
- [90] O. B. Ananin, Yu. A. Bykovskii, E. L. Stupitskii and A. M. Khudaverdyan, *Sov. J. Quantum Electron* **17**, 1474 (1987).
- [91] A. Misra and R. K. Thareja, *Appl. Surf. Sci.* **xx**, xxx (1999).
- [92] A. Misra, A. Mitra and R. K. Thareja, *Appl. Phys. Lett.* **xx**, xxx (1999).
- [93] A. A. Puretzky, D. B. Geogan *et al.*, AIP. Conference Proceedings, Laser Ablation: Mechanism and Application-II Second International Conference, April (1993) 288.
- [94] C. Girault, D. Damiani, J. Aubreton, and A. Catherinot, *Appl. Phys. Lett.* **54**, 2035 (1989).
- [95] D. B. Geohegan, and A. A. Puretzky, *Appl. Surf. Sc.* **96-98**, 131 (1996).
- [96] S. S. Harilal, C. V. Bindhu, V. P. N. Nampoori, and C. P. G. Vallabhan, *Appl. Phys. Lett.* **72**, 167 (1998).
- [97] P. E. Dyer, and J. Sidhu, *J. Appl. Phys.* **64**, 4657 (1988).
- [98] Wanniarachchi. K. A. Kumuduni, Yasushi Nakayama, Yoshiki Nakata, Tatsuo Okada, and Mitsuo Maeda, *Jpn. J. Appl. Phys.* **32**, L271-L273 (1993).
- [99] D. B. Geohegan, A. A. Puretzky, *Appl. Phys. Lett.* **67**, 197 (1995).
- [100] R. K. Dwivedi, S. P. Singh and R. K. Thareja, *Int. J. Mod. Phys. B* **xx**, xxx (1999).
- [101] G. Ding, J. E. Scharer and K. -L. Kelly, *J. Appl. Phys.* **84**, 1236 (1998).

- [102] R. B. Tukot et. al. J. Appl. Phys. **73**, 2173 (1993).
- [103] V. Yu. Baranov, O. N. Derkach, V. G. Grishina, M. F. Kanevskii and A. Yu. Sebrant, Phys. Rev. E. **48**, 1324 (1993).
- [104] R. K. Thareja, A. Misra and S. R. Franklin, Spectrochim. Acta B **xx**, xxx (1998).
- [105] A. Neogi, A. Misra and R. K. Thareja, J. Appl. Phys. **83**, 2831 (1998).
- [106] D. B. Geohegan, *Diagnostics and characteristics of PLD Laser plasmas* (Martin Marietta Energy Systems, Inc, 1993).
- [107] P. T. Rumsby and J. W. M. Paul, Plasma Phys. **16**, 247 (1974).
- [108] M. Mattioli, Plasma Phys. **13**, 19 (1971).
- [109] J. B. Hasted, *Physics of Atomic Collisions*, (Butterworths, Washington, 1964).
- [110] J. F. Seely and W. B. McKnight, J. Appl. Phys. **48**, 3691 (1977).
- [111] J. Grun, J. Stamper, C. Manka, J. Resnick, R. Burris, J. Crawford and B. H. Ripin, Phys. Rev. Lett. **21**, 2738 (1991).
- [112] S. H. Jeong, R. Greif and R. E. Russo, Appl. Surf. Sci. **127-129**, 177 (1998).
- [113] Nicholas A. Krall and Alvin W. Trivelpiece, *Principles of Plasma Physics* (McGraw-Hill, New York, 1973).
- [114] H. Motz, *The Physics of Laser Fusion* (Academic Press, 1979)
- [115] R. W. P. McWhirter (1965). Spectral intensities. In *Plasma Diagnostic Techniques* Ed. R. H. Huadelstone and S. L. Leonard, (Academic, New York, 1965) pp. 201-64.
- [116] G. Schmidh, Phys. fluids **3**, 965 (1960).
- [117] W. H. Bostick in Proceedings of the Symposium on Electromagnetics and Fluid Dynamics of Gaseous Plasma, I. Fox, ed. (polytechnic Press, Brooklyn, New York, 1962) pp-211.



- [118] J. M. Dawson, *Phys. fluids* **7**, 981 (1964).
- [119] P. I. Shkuropat and G. A. Shneerson, *Sov. Phys. Tech.* **12**, 249 (1969).
- [120] D. K. Bhadra, *Phys. Fluids* **11**, 234 (1968).
- [121] I. B. Bernstein and J. W. Fader, *Phys. Fluids* **11**, 2209 (1968).
- [122] A. F. Haught and D. H. Polk, *Phys. Fluids* **13**, 2825 (1970).
- [123] T. P. Write, *Phys. Fluids* **14**, 1905 (1971).
- [124] M. G. Haines, *Phys. Lett.* **6**, 313 (1963).
- [125] A. Cavaliere, *Phys. Lett.* **25 A**, 636 (1967).
- [126] J. Martineau and G. Tonon, *Phys. Lett.* **28 A**, 710 (1969).
- [127] F. Schwirzke and R. G. Tuckfield, *Phys. Rev. Lett.* **22**, 1284 (1969).
- [128] H. S. Dunn and M. J. Lubin, *J. Plasma Phys.* **4**, 573 (1970).
- [129] A. Neogi and R. K. Thareja, *J. Appl. Phys.* **85**, xxx (1999).
- [130] A. N. Mostovych, B. H. Ripin and J. A. Stamper, *Phys. Rev. Lett.* **62**, 2837 (1989).
- [131] T. A. Peyser, C. K. Manka, B. H. Ripin and G. Ganguli, *Phys. Fluids B* **4**, 2448 (1992).
- [132] Guy Dimonte and L. G. Wiley, *Phys. Rev. Lett.* **67**, 1755 (1991).
- [133] H. Nishiyama, T. Sato, A. Veefkind, S. Kamiyama, *Heat and mass transfer* **30**, 291 (1995).
- [134] B. H. Ripin, E. A. Mclean, C. K. Manka, C. Pawley, J. A. Stamper, T. A. Peyser, A. N. Mostovych, J. Grun, A. B. Hassam and J. Huba, *Phys. Rev. Lett.* **59**, 2299 (1987).

- [135] Shigefumi OKADA, Koshnosuke SATO and Tadashi SEKIGUCHI, *Jap. J. Appl. Phys.* **20**, 157 (1981).
- [136] Gerald I. Kent, Norman C. Jen and Francis F. Chen, *Phys. Fluids* **12**, 2140 (1969).
- [137] G. Ganguli, Y. C. Lee, P. J. Palmadesso and J. D. Huba, *International Conference on Plasma Physics* (1989), eds. A. Sen and P. K. Kaw, New Delhi, India.
- [138] G. Ganguli, Y. C. Lee and P. J. Palmadesso, *Phys. Fluids* **31**, 2753 (1988).
- [139] H. Romero, G. Ganguli and Y. C. Lee, *Phys. Rev. Lett.* **69**, 3503 (1992).
- [140] H. Romero and G. Ganguli, *Phys. Fluids* **5**, 3163 (1993).
- [141] H. Romero, G. Ganguli, Y. C. Lee and P. J. Palmadesso, *Phys. Fluids* **4**, 1708 (1992).
- [142] B. Lehnert, *Comments Plasma Phys. Controlled Fusion* **18**, 129 (1997).
- [143] A. Neogi and R. K. Thareja, *Communicated to Phys. Plasmas* (1998).
- [144] Fumino Kokai, *Jpn. J. Appl. Phys.* **36**, 3504 (1997).
- [145] A. Neogi and R. K. Thareja, *Communicated to J. Appl. Phys.* (1998).
- [146] H. F. Sakeek, T. Morrow, W. G. Graham and D. G. Walmsley, *J. Appl. Phys.* **75**, 1138 (1994).
- [147] C. Cali, F. La Rosa, G. Targia and D. Robba, *J. Appl. Phys.* **78**, 6265 (1995).
- [148] Z. Andreic, V. Henc-Bartolic and H. -J. Kunze, *Physica Scripta* **47**, 405 (1993).
- [149] A. H. El-Astal, S. Ikram, T. Morrow, W. G. Graham and D. G. Walmsley, *J. Appl. Phys.* **77**, 6572 (1995).
- [150] J. Gonzalo, F. Vega and C. N. Afonso, *J. Appl. Phys.* **77**, 6588 (1995).
- [151] P. Lecoeur, A. Gupta, P. R. Duncombe, G. Q. Gong and G. Xia, *J. Appl. Phys.* **80**, 513 (1996).

- [152] I. Apostol and R. Stopian, *Opt. Eng.* **35**, 1334 (1996).
- [153] T. F. Tseng, M. H. Yeh, K. S. Liu and I. N. Lin, *J. Appl. Phys.* **80**, 4984 (1996).
- [154] D. Luben, S. A. Barnett, K. Suzuki, S. Gorbatskin and J. E. Greene, *J. Vac. Sci. Technol. B* **3**, 968 (1985).
- [155] D. Miu, C. Grigoriu, D. Dragulescu and I. Chis, *Opt. Eng.* **35**, 1325 (1996).
- [156] J. Brcka, E. W. Kreutz and A. Voss, *Elektrotechn. Cas.* **43**, 118 (1992).
- [157] C. T. Chang, M. Hashmi and H. C. Pant, *Plasma Phys.* **19**, 1129 (1977).
- [158] R. J. von Gutfeld and R. W. Dreyfus, *Appl. Phys. Lett.* **54**, 1212 (1989).
- [159] J. M. Hendron, R. A. Al-Wazzan, C. Mohanty, T. Morrow and W. G. Graham, *Appl. Surf. Sci.* **96**, 112 (1996).
- [160] R. P. van Ingen, *J. Appl. Phys.* **76**, 8055 (1994).
- [161] K. Tanaka, T. Miyajima, N. Shirai, Q. Zhuang and R. Nakata, *J. Appl. Phys.* **77**, 6581 (1995).
- [162] M. A. Capano, *J. Appl. Phys.* **78**, 4790 (1995).
- [163] H. Koinuma, M. -S. Kim and M. Y. Yoshimoto, *Jpn. J. Appl. Phys.* **34**, 3720 (1995).
- [164] N. H. Cheung, Q. Y. Ying, J. P. Zheng and H. S. Kwok, *J. Appl. Phys.* **69**, 6349 (1991).
- [165] R. A. Al-Wazzam, C. L. S. Lewis and T. morrow *Rev. Sci. Instrum.* **67**, 85 (1996).
- [166] L. Ganapathi, S. Giles and Rama Rao, *Appl. Phys. Lett.* **63**, 993 (1993).
- [167] M. Harnafi and B. Dubreuil, *J. Appl. Phys.* **69**, 7565 (1991).
- [168] R. M. Gilenbach and P. L. G. Ventzek, *Appl. Phys. Lett.* **58**, 1597 (1991).

- [185] A. H. El-Astal and T. morrow, J. Appl. Phys. **80**, 1156 (1996).
- [186] R. Tambay, Ph.D thesis, IIT Kanpur (1991).
- [187] P. J. Wolf, J. Appl. Phys. **76**, 1480 (1994).
- [188] L. L. Danylewych and R. W. Nicholls, Proc. R. Soc. Lond. A **339**, 197 (1974).
- [189] R. J. Spindler, J. Quant. Spectrosc. Radiant. Transfer. **5**, 165 (1965).
- [190] F. F. Chen, in *Plasma Diagnostic Techniques* ed. R. H. Huddleston and S. L. Leonard (Academic, New York, 1971).
- [191] E Hontzopoulos, D. Charalambidis, C. Fortakis, Gy Farkas, Gy Horvath and Cs Toth, Opt. Commun. **67**, 124 (1988).
- [192] Daniel Fried and Gene P. Reck, J. Phys. D, Appl Phy **24**, 1065 (1991).
- [193] L. Spitzer, *Physics of Fully Ionised Gases* Second Ed. (Interscience Publishers, 1965).
- [194] D. J. Rose and M. Clarke, *Plasmas and Controlled Fusion* (John Wiley and Sons. New York, 1961).
- [195] H. Slitching, *Boundary layer Theory* (Pergamon Press, London, 1955).
- [196] Landau and Lifshitz, *Fluid Mechanics* (Pergamon Press, New York, 1984).
- [197] S. A. Kaplan, *Interstellar Gas Dynamics* (Pergamon Press, London 1966) pp 86.
- [198] W. T. Silfvast, S. H. Szeto, and O. R. Wood II, Opt. Lett. **4**, 271 (1979).
- [199] R. H. Dixon, J. F. Seeley, and R. C. Elton, Phys. Rev. Lett. **40**, 122 (1978).
- [200] J. M. Bridge, C. L. Cromer, and T. J. McIlrath, Appl. Opt. **25**, 2208 (1986).
- [201] V. I. Bayanov, V. A. Serebryakov, I. Yu. Skobelev, N. A. Soloer, A. Ya. Faenov, and S. Ya. Khakhalii, Sov. J. Quant. Elect. **18**, 1150 (1988).

- [202] Francis F. Chen, *Introduction to Plasma Physics and Controlled Fusion* Second edition, vol. 1 (Plenum Press, New York, 1984).
- [203] R. G. Tuckfield and F. Schwirzke, *Plasma Physics* 11, 11 (1969).
- [204] Abhilasha, Ph.D thesis, IIT Kanpur (1994).
- [205] X. Chen, J. Majumdar and A. Purohit, *Appl. Phys. A* 52, 328 (1991).
- [206] R. J. Goldston and P. H. Rutherford, *Introduction to Plasma Physics*" (Institute of Physics Publishing, Bnston and Philadelphia, 1995).
- [207] D. J. Southwood, *Planet Space Science* 16, 587 (1968).
- [208] J. O. Burns, M. L. Norman and D. A. Clarke, *Science* 253, 522 (1991).
- [209] R. Pudritz and M. Fich, *Galactic and Extragalactic Star Formation* NATO ASI Series C (Reidel, Dortrecht, 1988).
- [210] F. L. Waelbroeck and L. Chen, *Phys. Fluids B* 3, 601 (1991); A. Bhattacharjee, R. Iacono, J. L. Milovich and C. Paramicas, *Phys. Fluids B* 1, 2207 (1989).
- [211] Jams W. Poukey, *Phys. Fluids* 10, 2253 (1967).
- [212] J. Grun, M. E. Emery, C. K. Manka, T. N. Lee, E. A. Mclean, A. N. Mostovych, J. A. Stamper, S. Bodner, S. P. Obenschain and B. H. Ripin, *Phys. Rev. Lett.* 58, 2672 (1987).
- [213] N. D. Angelo and S. Von Goeler, *Phys. Fluids* 9, 309 (1966).

\_\_\_\_\_

[illegible]

[illegible]

```

write (60,*) d,vel
write (65,*)d,vel11
close (unit=50)
close (unit=55)
close (unit=60)
close (unit=65)
200 open (unit=70, access='append', file='all.out')
format (8X,F4.1,3X,F7.5,3X,F7.5,3X,F10.1,4X,F9.1,3X,F8.3,3X,F8.3)
write (70,200) d,z,z11,vel,vel11,wml,wml1
close (unit=70)
return
end

c-----
c-----calculates the initial point-----
c
subroutine initial(x,y,u,v)
dimension x(512),y(512)
i=0
75 i=i+1
   if (i.EQ.250) goto 80
   if ( y(i+1).EQ.y(i))goto 75
   i=i+1
   v=y(i)
   u=x(i)
   goto 80
80 continue
   v=v
   u=u
   return
end

c-----
c-----calculates the peak (1/2)-----
c
subroutine peak(x,y,u,v,w,z,kp)
dimension x(512),y(512),s(511)
real u1
if (kp.NE.0) goto 90
do 85 i=1,512
y(i)=y(i)-v
u1=u
85 continue
90 i=0
95 i=i+1
s(i)=abs(y(i))
goto 110
105 continue
i=i+1
110 if ( kp .NE. 2) goto 115
if ( x(i) .LT. u1) goto 95
if ( x(i) .GT. u) goto 140
goto 120
115 if (x(i) .LT. u) go to 95
120 if (y(i) .EQ. y(1)) goto 95
if (i .GT. 505) go to 125
if ( abs(s(i)) .GT. abs(y(i+1))) then

```



[illegible]

```

    s(i+1)= s(i)
    else
    s(i+1)= y(i+1)
    endif
    go to 105
125  continue
    z=s(i)
    i=0
130  i=i+1
    if ( x(i).LT.u) goto 130
    if (y(i).NE.z) go to 130
135  w=x(i)
    goto 150
140  continue
    z=s(i)
    i=0
145  i=i+1
    if (y(i).NE.z) go to 145
    w=x(i)
150  continue
    return
    end
c-----
c-----calculates the mean of the peak-----
c
    subroutine mean(x,y,u,v,z,e,wm,zm,kp)
    dimension  x(512),y(512)
    if ( kp .NE. 0) goto 155
    u1=u
155  continue
    i=0
    ze=abs(z)-e
    j1=0
    sw=0
    sz=0
160  continue
    i=i+1
    if (i.EQ.500) goto 175
    if (kp .NE. 2) goto 165
    if ( x(i) .LT. u1) goto 160
    if ( x(i) .GT. u) goto 175
    goto 170
165  if ( x(i) .LT. u) goto 160
170  if ( y(i) .EQ. y(1) ) goto 160
    if ( abs(y(i)).LT. ze) goto 160
    q=x(i)
    sw=sw+q
    r=y(i)
    sz=sz+r
    j1=j1+1
    goto 160
175  continue
    wm= (sw)/(j1)
    zm= (sz)/(j1)
    return
    end

```

c. p2.for - used in Chapter 5

c-----  
 c The following program is used in Chapter 5 which  
 c prepares data file for temperature calculation  
 c using relative intensity of lines of the same  
 c ionization state.  
 c-----

c TWO input fille

c\*\*\*\*\*  
 c dimension a(20),b(20)  
 c dimension x(20), y(20)  
 c open (unit=30,file='o319')  
 c\*\*\*\*\*DATA\*\*\*\*\*  
 c n=5  
 c n=n-1

c-----a(i) are the intensity of different lines---

a(1)=109  
 a(2)=28.5  
 a(3)=3  
 a(4)=2  
 a(5)=12.50

c-----b(i) are the corresponding energy value of  
 c of the upper level in eV. -----

b(1)=32.20  
 b(2)=34.28  
 b(3)=50.97  
 b(4)=40.57  
 b(5)=43.25

c-----  
 c read (30,\*) (x(i),y1(i),i=1,n)  
 c-----

do 5 i=1,n  
 y(i)= ALOG(a(1)/a(i+1))  
 x(i)= b(i+1)-b(1)  
 5 continue  
 n=n-1  
 do 6 i=1,n  
 y(4+i)= ALOG(a(2)/a(i+2))  
 x(4+i)= b(i+2)-b(2)  
 6 continue  
 n=n-1  
 do 7 i=1,n  
 y(7+i)= ALOG(a(3)/a(i+3))  
 x(7+i)= b(i+3)-b(3)  
 7 continue  
 n=n-1  
 do 8 i=1,n  
 y(9+i)= ALOG(a(4)/a(i+4))  
 x(9+i)= b(i+4)-b(4)  
 8 continue  
 open (unit=50,file='m40.dat')  
 n=10  
 do 20 i=1,n  
 write (50,\*)x(i),y(i)  
 20 continue  
 close(unit=30)  
 close(unit=50)  
 stop



This book is to be returned on the date last stamped.

[illegible]

A131098